Dynamics in Orientationally Disordered Solids

Julio César Martínez García

Universitat Politècnica de Catalunya

Dynamics in Orientationally Disordered Solids

by

Julio César Martínez García

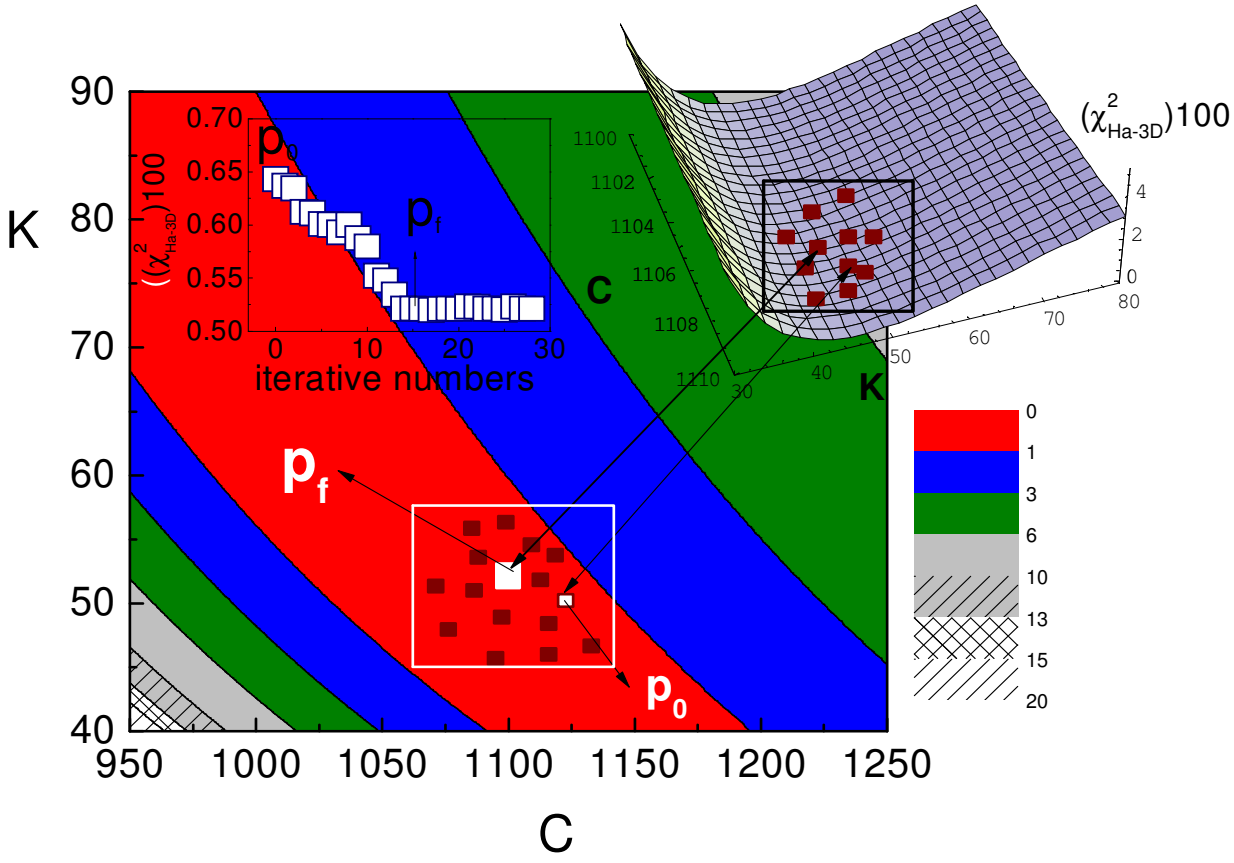

Universitat Politècnica de Catalunya
Dept. de Física i Enginyeria Nuclear
Barcelona, Mayo 2011

Dissertation of the Doctoral Thesis supervised by Dr. Josep Lluis Tamarit Mur and Dr. Luis Carlos Pardo Soto

Abstract

The key features of dynamics of ultraslowing glass forming systems are their universality in diversity. Its origin is recognized as one of the greatest challenges of condensed matter physics and materials engineering in the XXI century. Similar phenomena are observed on approaching the glass transition in low molecular weight supercooled liquids, polymers, colloidal fluids as well as in solids, for instance in orientationally disordered crystals, spin glass-like magnetic, vortex glasses. The upsurge of the primary relaxation time or related dynamical properties is the basic physical phenomena of the still mysterious previtreous behavior. This means a much more pronounced slowing down than the Arrhenius pattern observed far above the glass transition temperature. Portraying this behavior constitutes one of key checkpoints for theoretical models developed to unwind the glass transition puzzle. However, none of the aforementioned features can answer the understanding that governs the increase of relaxation time in liquids upon cooling.

In this thesis we focus on the above questions studying the dynamics of some materials for which their molecules can retain a translational order being orientationally disordered between them upon cooling, which are referred to plastic phases or orientationally disordered (OD) crystalline phases. The work presented in this thesis potentially extends the knowledge of dynamics of OD phases and orientationally glasses (OG), a research topic which has gained interest during the last decades. Through this study, especial attention has been devoted to the phenomenological equations accounting to the temperature dependence of the mean relaxation time describing the orientational dynamics. The study was carried out by the use of BDS as well as two complementary experimental techniques. We show distortion-sensitive and derivative-based empirical analysis of the validity of leading equations for portraying the previtreous evolution of primary relaxation time. A new method for studying the dynamics of glass forming systems is introduced and the minimization procedure is validated and discussed.

We present the results divided in two topics, the dynamics of the pure compounds and mixed crystals and the derivative analysis through different existing models. In the first topic we focus on the dynamics of the pure compounds and mixed crystals formed between cycloheptanol and cyclooctanol as well as the α-relaxation dynamics of 1-cyano-adamantane and its mixtures with 1-chloro-adamantane. The second topic is divided in two groups of models, linearized and non-linearized models. In the linearized models we show the application of the derivative based, distortion-sensitive analysis to liquid crystals (LC) and OD phases. We also discuss the results concerning to the cases of the olygomeric liquid epoxy resin (EPON828), neopentylalcohol and neopentylglycol mixture, isooctylcyanobiphenyl and propylene carbonate. The possible empirical correlations between one of the linearized models with the universal pattern for the high frequency wing of the loss curve for primary relaxation time for LCs and OD phases is also shown. In the final part we show that the form of the equation recently introduced by Mauro et al. does not allow a similar straightforward linearization procedure. Unlike the previous models, the involved parameters are not correlated with the slope and the intercept of a linear function. In order to solve this problem, we have introduced the concept of the *enthalpy space*. The evidences of the existence of crossovers as well as quantitative descriptions are discussed. We show also a new procedure for detecting the crossover in a very easy way. A new kind of crossovers which seems to be impossible to be detected by the classical Stickel transformation is presented.

Acknowledgments

The work presented in this thesis has been carried out at the Group of Characterization material (GCM) at the Universitat Politècnica de Catalunya (UPC). The work in this thesis would not have been realised without the financial support of the UPC fellowship.

The entire research work would not have finished without the support and the help of many people. To all of them, thank you very much.

My first and sincere thanks go to my research supervisor, Prof. Josep Lluis Tamarit Mur. I offer him my deepest gratitude for allowing me work in this exciting and fruitful research topic, for believing always in me, for giving me this wonderful opportunity to continue growing in my scientific career. I would like to sincerely thank him for reviewing this thesis, in this regard, I appreciate him his critical reading and useful remarks. His criticism provides invaluable guidance and support to the development of this thesis. I would like to thank to Dr. Luis Carlos Pardo for his reading and useful remarks to the final version of the thesis.

Thank you very much to Dr Maria del Barrio for helping me in all experimental sample preparations. Her help has provided big contributions in my experimental skills and big contributions in this thesis.

I am grateful to Dr. Sylwester Rzoska. I would like to thank sincerely him for his big contribution in this thesis and to my scientific career. Thank you very much for showing me the derivative analysis and for our many useful comments and intriguing questions. Thank you very much for opening me the door of your lab.

Special acknowledgments to Dr. Simone Cappacioli for his criticism and for all his help, for being always able for discussing in our informal seminars.
Thank you very much to Dr. Sergio Diez for helping in the dielectric measurements in my first year of my thesis. He showed me how to use the dielectric setup and how to perform measurements. Production

Thank you very much to the Katowice University in Poland. Thank you very much to Sebastian Pawlus, for his help with the data treatment and for many inspiring discussions. Thank you very much to the Centre for Electronic Correlations and Magnetism of University of Augsburg, especially to Dr. Peter Lunkenheimer and Prof. Dr. A. Loidl for providing me the possibility to perform the high frequency measurements of one of the pure compound studied in this thesis.

A la facultad de Física de la Universidad de la Habana donde me he formado. A todos los profesores que han tenido que ver con mi formación en especial al Dr. Ernesto Estevez Rams, con quien compartí mis primeros años de investigación del cual aprendí mucho y me guío en mi primera etapa como investigador. A Dr Angelina del Cueto por darme fuerzas para seguir adelante, a Dr. Jose Luis Sanchez Llamazares por creer en mí en un momento delicado de mi vida.

Muchas gracias a todos los miembros de la sección por recibirme con simpatía. En especial a dos personas. A Margarita Lorente, por ayudarme y animarme con su sincera amistad. Gracias por todos los detalles conmigo y con mi hijo. Muchas gracias a Antonio Muñoz, por su ayuda en todo lo informático y por su amistad.

A Rafa y Sonia por ser esas personas que aparecen en el camino de la vida no por unos años sino para toda la vida. Estoy eternamente agradecido por su sincera amistad por tomarme y aceptarme como soy, por darme fuerzas, por estar siempre presentes. Gracias a ustedes pude sentirme en familia. Gracias por ser mis mejores amigos

Esta tesis va dedicada a mi abuelo a mis padres a mi hermano y a mi hijo. A mis padres gracias por soportar la distancia de estos largos cuatro años, gracias por darme vida gracias por educarme, por inculcarme valores, por hacerme ver que en la vida las cosas se consiguen con fe esperanza e ilusión. A mi hermano las palabras se quedan muy pequeñas es esa persona que ha estado a mi lado a lo largo de toda mi vida, tenemos la suerte de compartir la misma profesión y la misma familia. Sin el no hubiese llegado aquí, es un ejemplo para mi. Gracias por todo lo que has hecho, me siento orgulloso de ti. Por ultimo dedicarle mi esfuerzo a mi hijo Alejandro y a mi esposa Iris por su ayuda y comprension, gracias Alejandro por venir al mundo y por hacerme feliz.

Contents

Chapter 1

Introduction

The key features of dynamics of ultraslowing glass forming systems are their universality in diversity. Its origin is recognized as one of the greatest challenges of condensed matter physics and material engineering in the XXI century [1-8]. Similar phenomena are observed on approaching the glass transition in low molecular weight supercooled liquids, polymers, colloidal fluids as well as in solids, for instance in orientationally disordered crystals, spin glass-like magnetic, vortex glasses [1,3,4,7-16]. Pre-vitreous dynamics is also proposed as a general reference for the category of complex liquids/soft matter systems [7].

The upsurge of the primary relaxation time or related dynamical properties is the basic physical phenomena of the still mysterious previtreous behavior. This means a much more pronounced slowing down than the Arrhenius pattern observed far above the glass transition temperature(T_g) [3,4,8,17-21]. Portraying this behavior constitutes one of key checkpoints for theoretical models developed to unwind the glass transition puzzle. It is noteworthy to recall that still a set of competing theoretical models exists and none of them is able to cover the majority of basic "universal" experimental features observed in so different systems as low molecular weight liquid, oligomers and polymers, spin glasses, liquid crystals, plastic crystals, colloids [8,17]. There seems to be a common agreement that this universality may be related to multibody heterogeneities, possible to be observed via the 4-point correlation function related techniques, such as the nonlinear dielectric spectroscopy (NDS) [20-22], the successor of the broadband dielectric spectroscopy (BDS) [3]. However understanding the nature of heterogeneities as well as the status of NDS method is still at the very beginning [3-5,8,9,17-19]. Undoubtedly, BDS remains the basic reference method for testing the previtreous dynamics, due to the possibility of covering more than 12 decades in frequency/time in a single experiment [8]. One of basic outputs of BDS is the dielectric permittivity loss curve $\varepsilon^{''}(f)$ which peak coordinates are directly related to the primary relaxations, namely $\tau = {}^{2\pi}/_{f_{peak}}$[8].

However, none of the aforementioned features can answer the understanding what governs the increase of relaxation time in liquids upon cooling. The increase of relaxation time and viscosity when the temperature is lowered and the formation of a non-equilibrium solid state are universal

in the sense that it regards all types of materials ranging from metals to polymers. However, the relaxation time has qualitatively different temperature dependencies in different systems. The central common questions in the field are:

- What causes the non-Arrhenius temperature dependence of the average α-relaxation time?
- Does the relaxation time diverge at finite temperatures or only as $T \rightarrow 0$?
- Does the relaxation time diverge at some finite temperature below the glass transition temperature T_g?
- Is the relaxation time of all liquids described by the same underlying model?
- Is the existence of a thermodynamic singularity the cause of the dramatic viscous slowdown?

The vast majority of the studies have been carried out on canonical glass formers which mixed orientational and translational degrees of freedom of the liquid state are freezing at the glass transition. In this work we focus on the above questions studying the dynamic of some materials for which their molecules can retain a translational order being orientationally disordered between them upon cooling, which are referred to plastic phases or orientationally disordered crystalline phases (ODIC).
The central issue of this thesis is the study of the dynamic of the orientational disordered crystals ODIC. The study was carried out by the use of BDS as well as two complementary experimental techniques. We show distortion-sensitive and derivative-based empirical analysis of the validity of leading equations for portraying the previtreous evolution of primary relaxation time. A new method for studying the dynamic of glass forming systems is introduced and the minimization procedure is validated and discussed.

Thesis' Outline

The thesis is structured as follows: Chapter 2 gives an introduction to the theoretical concepts of dielectric relaxation. The Kirkwood correlation factor for molecular systems is discussed in the first part. In the second part we focus on the dielectric properties under a periodic electric field. The theoretical and phenomenological aspects of the primary and secondary relaxation processes are reviewed and discussed. In the last part of the chapter, the coupling-model equation is discussed and corrective functions are proposed.
Chapter 3 presents the materials and experimental techniques that have been used in this work. The first section of the chapter is devoted to the studied materials. We describe the polymorphic behavior of the studied materials which display orientationally disordered phases. The experimental techniques are detailed in the second part of this chapter. The basic concept of the dielectric spectroscopy technique as well as a brief description of the experimental setup used in this work

is shortly introduced. Two additional experimental techniques, X-ray diffraction and calorimetric, which have been used for complementing the study, are presented as well.
In Chapter 4 we focus on the data analysis procedure used in this work. Three subjects were covered. The brief first section is devoted to the basic procedure of dielectric data analysis. We show the basic procedure for processing dielectric experimental data, in particular for obtaining the relaxation time, as well as the procedure to analyze the temperature dependence of the derived relaxation time. A new method for studying the dynamic of glass forming systems is introduced and the minimization procedure is discussed.
The results and discussion are presented in Chapter 5. They are presented in two groups (linearized and non- linearized models equation). The first section of the chapter focus on the linearized model equation, where the application of the derivative based, distortion-sensitive analysis to ODIC materials are presented. In the last part we showed the application of the minimization procedure to 30 glass forming liquids system. The evidences of the existence of crossovers in the Mauro equation as well as a quantitative description are discussed.
The last part of the thesis corresponds to Chapter 6 (General Conclusions); therein, the main results and conclusions reported in this work are reviewed and presented together in order to provide a general view of them.

1.1 The glass transition

The transition from supercooled liquid to structural glass is observed in a wide variety of materials with varying compositions and structures. The glass transition is defined experimentally by the presence of two nearly universal features: a rapid increase in the relaxation time with decreasing temperature and a not exponential relaxation. This scenario, occurring at the glass transition temperature T_g, usually identified by the viscosity attaining 10^{12} Poise, or by the step of ΔH in differential scanning calorimetric (DSC) measurements or when the α-relaxation time τ takes values around $100s$. The criterion of $\tau_\alpha = 100s$ is often used as a definition of the glass transition temperature. The temperature evolution of dynamic properties including the dielectric relaxation time above glass transition shows a divergence in the apparent activation energy, refusing the Arrhenius law over a substantial range of temperatures, making this question as a still unsolved problem of condensed matter physics. Phenomenological studies dominate these experiments, as due to both structural complexity of the amorphous matter and the diverging time scales of its dynamics, a commonly accepted theory has not yet been found [3,4,8]. In the next sections we focus on the principal conceptual aspect used for describing the glass transition phenomenon. The thermodynamic, entropy and dynamic point of view are presented.

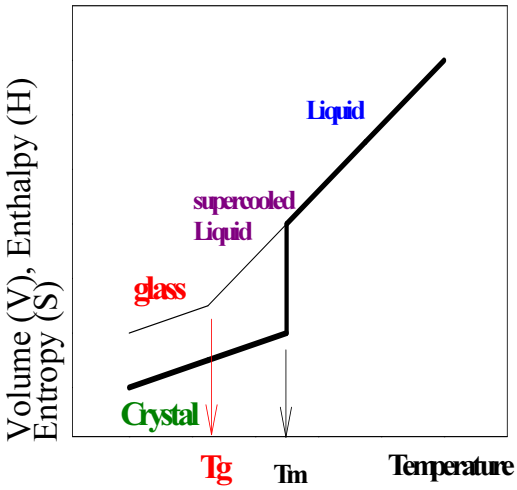

Figure 1.1: *Schematic diagram showing the glass transition phenomenom. Cooling a liquid rapidly below the melting temperature T_m, may results in the formation of a supercooled metastable state. The transition from metaestable liquid to glassy state is reached by passing the glass transition temperature T_g.*

1.1.1 Thermodynamic point of view

A glass is formed by cooling a liquid fast enough to avoid crystallization. At continued supercooling the liquid viscosity increases dramatically, and at some point the liquid freezes continuously into a no crystalline "solid". This is defined as the glass transition, although it is not a phase transition with a well-defined transition temperature [23-25].
If a liquid is cooled slowly (following an equilibrium state) when it reaches its melting temperature T_m it starts to crystallize and shows discontinuities in first (enthalpy, volume, entropy) and second order (heat capacity, thermal expansion coefficient) thermodynamics properties (Figure 1.1). If cooled rapidly the liquid may avoid crystallization, even well below the melting temperature T_m. The change in the temperature dependence of the volume gives rise to a discontinuity in the thermal expansion coefficient when passing T_g. This kind of discontinuity leads a thermodynamic definition of the glass transition phenomenon. This transition is similar to a second-order phase transition in the Ehrenfest sense with continuity of volume and entropy, but discontinuous changes of their derivatives [26]. The transition is continuous and cooling-rate dependent, so it cannot be a genuine phase transition.

1.1.2 Correlations between dynamic and thermodynamic properties

1.1.2.1 Free volume model

Free-volume model have been developed on the assumption that molecular transport in viscous fluids occurs only when hole having a volume large enough to accommodate a molecule form by redistribution of some free volume. The basic idea of the model is that molecules need "free"

volume in order to be able to rearrange [27,28]. As the liquid contracts upon cooling, less free volume becomes available. Cohen and Turnbull [27] also consider that the local free volumes are statistically uncorrelated following a Boltzman distribution. If the free volume per molecule is denoted by $v_f(T)$ the probability of the molecular distribution $P(v_f)$ will be defined as an exponential law. Taking in to account that the diffusion constant D is given by the probability of finding a free volume, the relaxation time and the viscosity can also be defined also by an exponential law, giving the following model prediction .

$$\tau(s) = \tau_0 \exp\left[\frac{C}{v_f(T)}\right] \tag{1.1}$$

where the constant C is related to the barrier height of the energy due to the rearrangement of atom units and the prefactor τ_0 is associated only with the high temperature dynamical domain
Cohen and collaborators defined the free volume as that part of the volume "which can be redistributed without energy cost" and argued that this quantity goes to zero at a finite temperature. This leads to VFT equation if $v_f(T)$ is expanded to first order. Doolittle [29] defined the free volume by subtracting the molecular volume defined by extrapolating the liquid volume to zero temperature, implying that $v_f \to 0$ only when $T \to 0$.
The main problem of the free volume models is that it is not possible to define free volume rigorously. In this simple model no characteristic length scale is involved. On the other hand, all transport properties should have the same temperature dependence and a decoupling of rotational and traslational diffusion can not be explained within this model. Furthermore, the pressure dependence of the viscocity and the α-relaxation time is not adequately reproduced. Free-volume models are not generally popular because the relaxation time is not just a function of density ρ [8].

1.1.2.2 Adam-Gibbs theory (AG)

Assuming that molecular reorientations take place cooperatively, Adam and Gibbs (AG) argued that the minimum size of a cooperatively rearranging region is determined by the requirement that it should contain at least two different configurational states [30]. They invoked the concept of a cooperatively rearranging region (CRR) being defined as the smallest volume which can change its configuration indepent from neighboring regions. As the temperature is lowered the cooperatively rearranging regions grow. Assuming that the activation energy is proportional to the region volume, Adam and Gibbs relate the relaxation time to the numbers of particles $\left(N(T) \sim S_{conf}(T)\right)$ per CRR leading the following equation :

$$\tau(s) = \tau_0 \exp\left[\frac{C}{TS_{conf}(T)}\right] \tag{1.2}$$

In this equation, the constant C is related to the barrier height of the energy due to the rearrangement of atom units and the prefactor τ_0 is associated only with the high temperature dynamical domain.

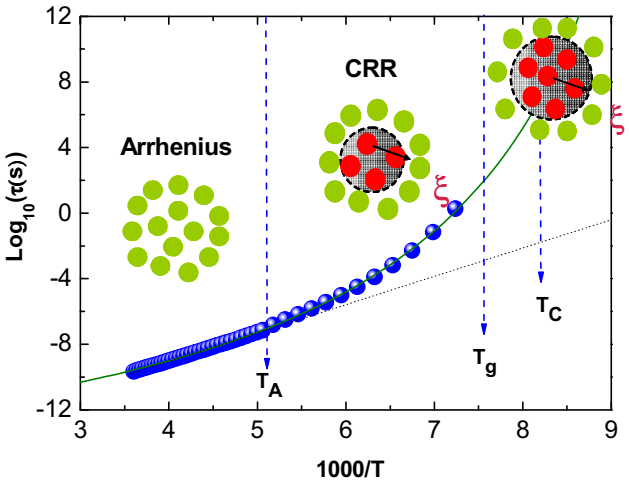

Figure 1.2: *Arrhenius plot of the relaxation time data obtained for a case example. The temperature T_A denotes the caging temperature which stands for the temperature above which all entities are moving without cooperative motions. As the temperature is lowered the cooperatively rearranging regions grow. The dramatic increase of the relaxation time upon cooling is explained by a divergence of the size of cooperatively rearranging regions at T_C,($T_C < T_g$).*

The namely configurational entropy S_{conf} is the configurational part of the excess entropy which assuming a two-state model, it can be estimated as a fraction of the total numbers of particles N as $S_{conf}(T) = N(T)NK_B \ln 2$ allowing a microscopic description of the CRR .
Using thermodynamic considerations, the configurationl entropy can be related of the heat capacity change ΔC_p at the glass transition. Considering that $\Delta C_p \approx {}^{C}/_{T}$ the AG model leads the mostly use temperature relaxation time dependence (VFT) which predicts a temperature T_0 with infinity relaxation time. It also gives an equation for calculating the size of a CRR as $N(T) \sim \frac{1}{C(T-T_0)}$ which will diverge at T_0
Although the Adam-Gibbs model does not provide information about the absolute size of a CRR at T_g, it has enjoyed appreciable success in accord with experimental values in many fields, it is a beautiful theory which connects dynamics to thermodynamic properties. This theory gives a possible answer to the dramatic increase of the relaxation time upon cooling which reflects the existence of an underlying second-order phase transition to a state of zero configurational entropy, a state usually called an ideal glass. This is an attractive scenario, for the believing of the critical phenomena [26,31].

1.1.3 Dynamic models

1.1.3.1 Mode coupling theory (MCT)

Based on current liquid state theories, another theoretical approach, namely mode coupling theory (MCT), was introduced in 1992 by Götze and Sjögren [32] which provides detailed microscopic

density fluctuations. This theory involves an analysis of a set of non-linear integral differential equations describing the evolution of pair correlation functions of a wave-vector and time dependent fluctuations that characterize the liquids [32]. The MCT theory explain the relaxation time evolution in terms of a phase transition at a critical temperature $T_C = T_{MCT}$ $(T_C > T_g)$, where a phase transition from an ergodic $(T > T_C)$ to a non-ergodic $(T < T_C)$ states takes places. For the ergodic state MCT theory predicts that the α- relaxation time can be scale by the following law.

$$\tau_\alpha(T) \sim \left(\frac{T_{MCT}}{T - T_{MCT}}\right)^\gamma, \; T > T_{MCT} + 20K \tag{1.3}$$

where the power exponet γ is a constant and $\tau_\alpha < \tau_\alpha(T_{MCT}) \approx 10^{-7}s << \tau(T_g) \approx 100s$.
Two relaxation processes are also predicted: a slow α-process and a fast β-process. The α-process is identical with the structural relaxation process and exhibits strong temperature dependence. Due to this relaxation the molecules or atoms of the liquids finally loose all correlation in space and time. The β-process is an intermolecular secondary relaxation process. Both processes are described by power laws with exponents which are interrelated. In opposition to structural phase transitions these exponents are not universal. They depend on the individual interaction potential of the particles. Great progress made by MCT is to describe the change of the dynamic mechanism with temperature and to predict the existence of a crossover temperature T_C, where the two relaxation processes no longer merge and begin to diverge.

1.1.3.2 Dynamic scaling model (DSM)

Probably, the only model for portraying dynamics on vitrification and directly coupled to critical phenomena is the dynamic scaling model (DSM) put forward by Colby [33]. This model is predicted under the consideration that the cluster random walk created by the diffusion of the free volume have cooperatively rearranged. It found a power law dependence for the relaxation modulus $G(t) \sim t^{-\frac{2}{z}}$, being z the dynamic critical exponent which relates the relaxation time of a cluster with its size. For all glass-forming materials this exponent was suggested as $z = 6$.
Colby [33] explains the dramatic increase of the relaxation time upon cooling proposing a power law relationship between the relaxation time and the correlation length ξ of cooperative rearranging regions, which is associated with dynamic heterogeneities. Using data obtained by four-dimensional (4-D) NMR experiments, Colby found an universal scaling temperature dependence of this length scale of cooperative motion (see Figure (1.3)) [34]. It allows to argue that a dynamic scaling form, where the relaxation time and the size of cooperatively rearranging regions diverge at a critical temperature T_C can be expressed as:

$$\tau \sim \xi^z \sim \left(\frac{T - T_C}{T_C}\right)^{-\phi = -\nu z = -9}, \; T_A > T > T_g \; and \; T_0 < T_C < T_g \tag{1.4}$$

where T_0 is the Vogel temperature, $z = 6$ is the dynamic (critical) exponent and $\nu = 3/2$ is the

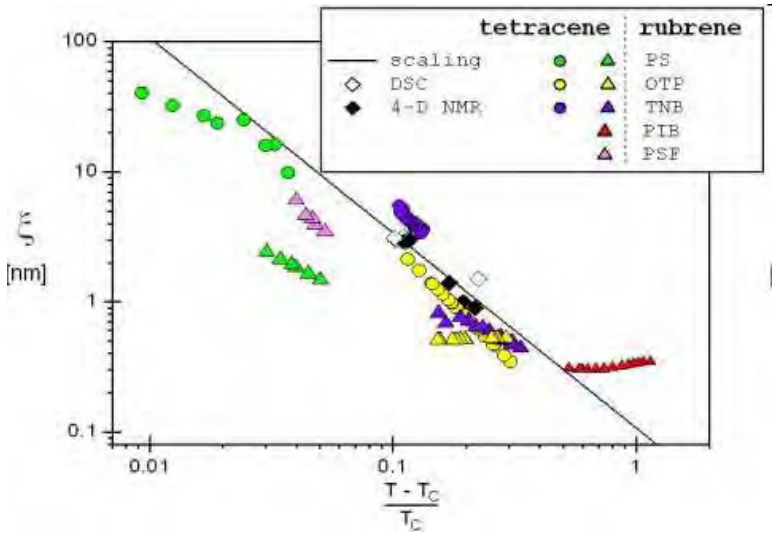

Figure 1.3: *Temperature dependence of the cooperative size, plotted in the form expected by dynamic scaling model. The symbols represent cooperative size measured by DSC (open diamonds), 4-D NMR (closed diamonds), and diffusive experiments with tetracene (circles) and rubrene (triangles). The solid line is the slope of $-3/2$ expected by dynamic scaling model. The figure was taken from [34].*

exponent describing the divergence (at T_C) of the correlation length ξ of cooperative rearranging regions, also understood as precritical fluctuations. The temperature T_A denotes the caging temperature which stands for the temperature above which all entities are moving without cooperative motions.

The DSM assumes the same universal critical-type description for any polymer melt or low molecular weight supercooled liquid. Nevertheless, universal behavior for the cooperative length scale and non-universal behavior of the relaxation time were previously found [34] in such a way that the non-universal dependence of τ is understood as the difference for each glass former owing to the fact that energetic barriers for molecular motion depend on the chemical structure details. It means that each liquid has a distinct low temperature activation energy E_{low} and the above equation can be written as:

$$\tau \sim \tau_0 \left(\frac{T - T_C}{T_C} \right)^{-\phi} \exp \left[\frac{E_{low}}{RT} \right] , \; T > T_g \; and \; T_0 < T_C < T_g \tag{1.5}$$

where the Arrhenius term is the same as the one appearing for the behavior in the glass state, i.e. for $T < T_g$.

1.2 Temperature dependence of the primary relaxation time

Generally, one may expect to apply the Arrhenius-like equation for portraying the non-Arrhenius dynamics with the apparent (temperature dependent) activation energy, namely [3,4,8]:

$$\tau(T) = \tau_0 \exp\left[\frac{E_a(T)}{T}\right] \tag{1.6}$$

However, the form of the evolution of $E_a(T)$ is unknown, so efforts of researchers focused on equations which empirically proved their validity [3-5,17-19]. Undoubtedly for the last decades the most commonly accepted was the Vogel-Fulcher-Tammann (VFT) equation, namely [3,8,17,35-37]:

$$\tau(T) = \tau_0 \exp\left[\frac{B}{T - T_0}\right] = \tau_0 \exp\left[\frac{D_T T_0}{T - T_0}\right] \tag{1.7}$$

where T_0 is the VFT estimation of the ideal glass transition temperature and D_T is the fragility strength coefficient.

For several basic theoretical models significant efforts were devoted to produce this relation as the checkpoint. The free volume and Adam – Gibbs based approaches may serve as best examples [3]. Comparing the equations (1.6) and (1.7) one can also easily obtain $E_a(T) = {}^{DT_0}/_{(T-T_0)}$[3,8,17]. This equation introduces also one of basic metrics for the fragility [3,8,38], the coefficient D_T. However, just this issue has been fundamentally criticized by Johari [39], who indicated that the introduction $B = D_T T_0$ does not yield the Arrhenius equation for $T_0 = 0$. A problem seems to exist also for the prefactor τ_0, for liquids usually linked to quasi-universal value $\tau_0 \approx 10^{-14} s$, which was related to the average phonon frequency [3,8]. However, there are several dynamical domains in glass forming systems, each associated with different set of parameters in the VFT equation [8]. The mentioned value of τ_0 can be associated only with the high temperature dynamical domain, however experiments show also values close to $\tau_0 \approx 10^{-11} s$ [40]. Moreover, for the pressure counterpart of the VFT equation the prefactor can be related to the absolute stability limit of the liquid state, located in the negative pressures domain [41,42]. It seems that a similar assumption is possible for the VFT equation if its corrected form is introduced [43]:

$$\tau(T) = \tau_0 \exp\left[\frac{D_T (T_{SL} - T)}{T - T_0} \frac{T_0}{T_{SL}}\right] \tag{1.8}$$

where T_{SL} is the absolute stability limit temperature.

The dynamics of supercooled liquids is usually tested below the melting temperature, i.e. for $T_g < T < T_m$. In this domain the condition $T_{SL} >> T$ and then the condition $T_{SL} - T \approx T_{SL}$ is fulfilled. Consequently in the ultraviscous domain the equation (1.8) converts into equation (1.7). The "Johari objection" can be minimized when taking into account that the Arrhenius domain occurs far above the melting temperature $T - T_0 \approx T$ what yields the crossover to the quasi-Arrhenius equation with finite T_0 [43]:

$$\tau(T) = \tau_0 \exp\left[\frac{D_T ({}^{T_0}/_{T_{SL}}) T_0}{{}^{T}/_{\Delta T}}\right] \tag{1.9}$$

Recently, Hecksher et al.[19] carried out analysis of $\tau(T)$ data for 42 ultraviscous molecular liquids

using the VFT equation and recalling the popular in recent years "Avramov" equation [44]:

$$\tau(T) = \tau_0 \exp\left[\frac{A}{T^D}\right]_{P=const} = \tau_0 \exp\left[\varepsilon\left(\frac{T_g(P=0.1MPa)}{T}\right)^D\right] \tag{1.10}$$

where A and ε are constant coefficients, $T_g(P)$ is the pressure dependence of the glass temperature and D is related to fragility.

The state of the art analysis led to the surprising conclusion of the superiority of the "Avramov" equation over the VFT one [19]. Then it was concluded [19] "*Thus, with Occam's razor in mind—'it is vain to do with more what can be done with fewer'—we suggest that in the search for the correct theory for ultraviscous liquid dynamics, theories not predicting a dynamic divergence of the VFT form should be focused on.*"

It is noteworthy that substituting for $T_g(P)$ the equation recently derived by Drozd-Rzoska et al. [41,42] one obtains the link of the prefactor τ_0 to the absolute stability limit of the metastable supercooled/superpressed liquid.

Despite the strong empirical validation of the non-divergent description of $\tau(P)$ evolution the subsequent analysis in glass formers where a dominant element of symmetry exists [45], lead to the clear validity of the critical-like behavior:

$$\tau(T) = \tau_0\left(\frac{T-T_C}{T_C}\right)^{-\phi}, \; T_C < T_g \tag{1.11}$$

The value of the power exponent was close to predictions of the dynamical scaling model (DSM) [33, 34], $\phi \approx 9$, which is inherently associated with the presence of heterogeneities and the hidden phase transition at $T_C < T_g$. Here the prefactor has formal mathematical meaning $\tau_0 = \tau(2T_C)$. The superiority of description via equation (1.11) is particularly evident for liquid crystalline glass formers and orientationally disordered crystals.

The situation becomes even more puzzling when recalling two "non-divergent" equations recalled recently. Elmatad et al [46] as the output of the random energy model derived the equation:

$$\tau(T) = \tau_0 \exp\left[J'\left(\frac{T_0'}{T} - 1\right)^2\right] \tag{1.12}$$

where $J' = (J/T_0')^2$ is the parameter to set the energy scale for excitations of correlated dynamics originated at $T_m > T_0' > T_g$.

The overlapping of 67 sets of data $\log_{10}(\tau/\tau_0)$ in vs. $J' = (J/T_0' - 1)^2$scales was shown [46], although for many glass formers the temperature range of validity was extremely narrow. For this model the prefactor is defined by $\tau_0 = \tau\left(T = T_0'\right)$ condition.

Very recently Mauro et al. [47] employed constraint theory to the Adam-Gibbs basic equation and obtained the relation earlier introduced empirically by Waterton in 1932 [48], namely:

$$\tau(T) = \tau_0 \exp\left[\frac{K}{T}\exp\left(\frac{C}{T}\right)\right] \tag{1.13}$$

As indicated in ref. [47] the model offers an improved description of the viscosity or relaxation time vs. temperature relationship for both inorganic and organic liquids using the same number of parameters as VFT and "Avramov" descriptions. Lunkenheimer et al. [49] tested this equation for a set of $\tau(T)$ and concluded that it "*seems to be a good alternative to the VFT equation, especially as in many cases it can parameterize broadband relaxation-time data with a single formula without invoking any transitions between different functions. Thus, taking into account Occam's razor, (this equation) often seems to be preferable to other approaches*."

The anomalous increase of primary relaxation time or viscosity is the most fundamental experimental feature for the pre-vitreous dynamics. It seems that after the collapse of the long period of the dominance of the VFT equation the situation is puzzling.

1.3 Fragility

Liquid fragility, an important parameter used to classify the dynamic behavior of the glass-forming liquids, measures the degree of non-Arrhenius behaviour. The strength of liquid fragility shows the differences in the tendency of the liquid structure to change with temperature.

In 1985 Angell first introduced the concept of "liquid fragility"[50]. He adopted a reduced plot, namely "Angell" plot as Figure (1.4), to display the changes of viscosity for the liquid state, with particular interest being focused on the possibility of using a general criterion to evaluate the dynamic behavior as well as nonlinear structural relaxation of the liquids. Concretely, the logarithm of viscosity of the liquids is plotted against reduced temperature T_g/T . According to it, glass-forming liquids are classified into two types: strong glass formers which show an Arrhenius behavior and display nearly a line in 'Angell" plot, and fragile glass formers of which the temperature dependence of viscosity, displays a curve in such plot.

The strong/fragile classification has been used to indicate the sensitivity of the liquid structure changes. From the microscopic point of view, it is believed that strong liquids would have strong chemical bonds, showing a strong resistance to structural changes, even if large temperature variations are applied. From a calorimetric point of view such behaviour corresponds to very small jumps in the specific heat ΔC_p at T_g. Fragile liquids usually have a less stable structure and the physical property changes dramatically, showing large jumps of such quantity.

The slope of the curve at the point where $T_g/T = 1$ is conveniently defined as a fragility parameter, m, to display the fragility of different liquids [50]:

$$m = \frac{\partial \log_{10}\tau(T)}{\partial\left(T_g/T\right)}\,|_{T=T_g} = \frac{\partial \log_{10}\eta(T)}{\partial\left(T_g/T\right)}\,|_{T=T_g} \tag{1.14}$$

Here τ is the average relaxation time at the temperature T and η the shear viscosity. A large

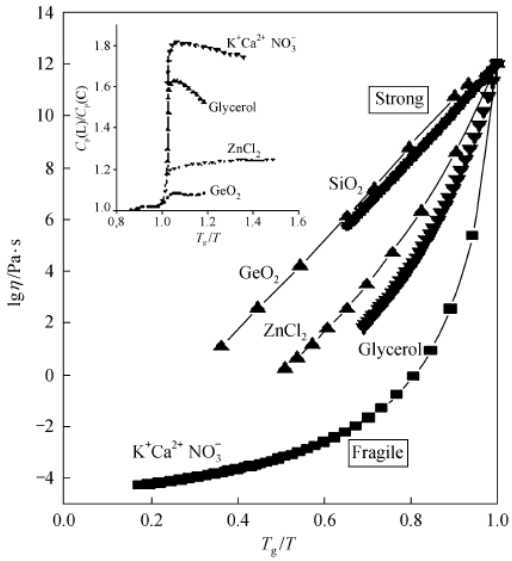

Figure 1.4: *Arrhenius plots of the viscosity data of some organic compounds scaled by T_g values showing the "strong/fragile" pattern of liquid behaviour. As is shown in the insert, the jump in $C_p(T_g)$ is generally large for fragile liquids and small for strong liquids, although there are a number of exceptions, particularly when hydrogen bonding is present. The figure was taken from[51].*

value of m means that the liquid is fragile. Figure (1.4) shows the different changes of viscosity approaching to T_g. The ratio of the heat capacity of supercooled liquids to that of amorphous solids $C_p(L)/C_p(S)$ is showed in the inset of Figure (1.4) [51]. The jump in this graph is generally large for fragile liquids and small for strong liquids. According to it, SiO_2 and G_eO_2 belong to typical strong liquids in the limit of 16 for fragility parameter m; Arrhenius behavior is characterized by $m = 16$. Only a few glass formers have fragility below 25. Glycerol is intermediate with $m = 50$, while, e.g., the molten salt $K_3Ca_2(NO_3)_7$ has $m = 90$. A high-fragility liquid takes values around $m = 150$.

Taking in to account that the stronger than Arrhenius behavior derives from $\triangle E$ increasing with decreasing temperature, an alternative measure of the degree of non-Arrhenius behaviour can be provided by the "index" $I = I(T)$[52-54]:

$$I(T) = -\frac{\partial \ln \Delta E(T)}{\partial \ln T} \tag{1.15}$$

where I quantifies Arrhenius deviations in a way inspired by the Grüneisen parameter [55]. A straightforward calculation shows that the fragility is related to the Index by

$$m = 16(1 + I(T_g)) \tag{1.16}$$

The Arrhenius case has $I = 0$ and $m = 16$. Typical values of I at $T_g(\tau = 100s)$ are ranging from $I = 3$ to $I = 8$ corresponding to fragility values from $m = 47$ to $m = 127$.

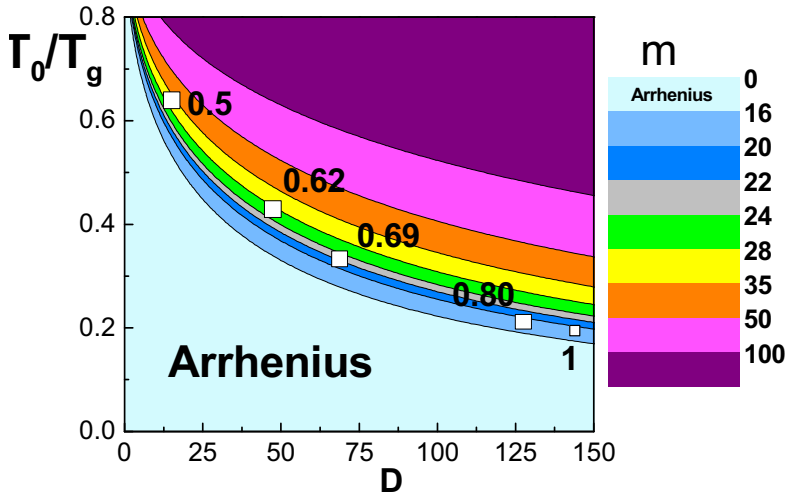

Figure 1.5: *3D plot of equation (1.17) for mixed crystals of* $(CNadm)_x(CLadm)_{1-x}$. *The figure shows the coherence between the dynamic values obtained for each mixed crystal. It nicely evidences the increase of the strength parameter D when the mole fraction of CNAadm decreases together with a continuous and coherent change of the* T_0/T_g *ratio [56].*

For all glass model equations is possible to define the corresponding fragility index equation. In the last section we showed that, a common characteristic for all glass forming equations describing the variation of the characteristic relaxation time or viscosity is that they involve three parameters $(u_1 = \tau_0, u_2, u_3)$. Bypassed through the derivative definition of the index fragility, the number of parameters involved are reduced from three to only two, allowing for all of them an index fragility equation with two variables $m(u_1, u_2)$. It means that for all of them, the fragility index can be showed as defined a $3D$-surface, where the variables u_1 and u_2 will be related with the model parameters. Using the original definition (equation (1.14)), we can define the fragility index as follows:

- VFT equation

$$m(D,\ T_0/T_g) = \frac{1}{\ln 10}\left(\frac{D\,(T_0/T_g)}{\left(1-\frac{T_0}{T_g}\right)^2}\right) \tag{1.17}$$

- DSM equation

$$m\left(\phi\,,\,\frac{T_C}{T_g}\right) = \frac{1}{\ln 10}\left(\frac{\phi}{1-\frac{T_C}{T_g}}\right) \tag{1.18}$$

- Elmatad equation

$$m\left(J'\,,\,\frac{T_0'}{T_g}\right) = \frac{2J'}{\ln 10}\left(\frac{T_0'}{T_g}\right)\left(\frac{T_0'}{T_g}-1\right) \tag{1.19}$$

- Avramov equation

$$m\left(A\,,\,D\right)=\frac{1}{\ln 10}\left(\frac{AD}{\left(T_g\right)^D}\right) \tag{1.20}$$

- Mauro equation

$$m\left(K\,,\,\frac{C}{T_g}\right)=\frac{1}{\ln 10}\frac{K}{T_g}\left(1+\frac{C}{T_g}\right)\exp\left(\frac{C}{T_g}\right) \tag{1.21}$$

The $3D-$fragility representation can be useful for testing the quality of the fitting parameters of the glass model equations. The value of fragility parameter m can be subjected to big discrepancies, depending on the method used to calculate it. The most popular method is to obtain it from the analysis of the fitting parameters, mostly determined from data far away from T_g and so affected by big uncertainties. The parameters will represent a point in a tridimensional fragility surface and their quality can be tested by the possible correlations between the variables u_1 and u_2 easily showed in a Contourplot bidimensional graph.

One example result is showed in Figure (1.5) [56]. The dynamic characterization of the mixed crystals was carried out by the use of the VFT equation. The points in Figure (1.5) correspond to different mixed crystals, showing a nice coherence between the dynamic values obtained for each mixed crystal. It nicely evidences the increase of the strength parameter D when the mole fraction of *CNAadm* decreases together with a continuous and coherent change of the T_0/T_g ratio.

Bibliography

[1] P. W. Anderson, Science **267**, 1615, (1995).

[2] Science **309**, (2005): Special issue for 125th anniversary.

[3] E. Donth, *The Glass Transition. Relaxation Dynamics in Liquids and Disordered Material*, Springer Series in Material Sci. II, Vol. 48 (Springer Verlag, Berlin, 1998).

[4] P. G. Debenedetti, F. H. Stillinger, Nature **410**, 259, (2001).

[5] L. O. Hedges, R. L. Jack, J. P. Garrahan, D. Chandler, Science **323**, 1309, (2009).

[6] K. Chang, *The Nature of Glass Remains Anything but Clear*, The New York Times, July 29th issue (2008).

[7] R. A. L. Jones, Soft condensed matter (Oxford Univ. Press, NY, 2002).

[8] F. Kremer, A. Schoenhals, *Broadband Dielectric Spectroscopy*, (Springer Verlag, Berlin, 2003).

[9] J. Mattsson, H. M. Wyss, A. Fernandez-Nieves, K. Miyazaki, Z. Hu, D. R. Reichman, D. A. Weitz, Nature **462**, 83, (2009).

[10] S. J. Rzoska, A. Drozd-Rzoska, A. R. Imre, *The link between the pressure evolution of the glass temperature in colloidal and molecular glass formers* in NATO Sci. Series II: Metastable Systems under Pressure (Springer Verlag, Berlin, 2010).

[11] A. Crisanti, F. Ritort, Physica A **280,** 155, (2000).

[12] M. Grousson, G. Tarjus, P. Viot, J. Phys.: Condens. Matter **14,** 1617, (2002).

[13] J. Koetzler, M. Kaufmann, G. Nakielski, R. Behr, Phys. Rev. Lett **72**, 2081, (1994).

[14] R. Lortz, Ch. Meingast, A. I. Rykov, S. Tajima, J. Low. Temp. Phys. **147,** 365, (2007).

[15] F. Affouard, M. Descamps, Phys. Rev. B **72**, 012501, (2005).

[16] F. Affouard, M. Descamps, Phys. Rev. Lett **87**, 35501, (2001).

[17] S. A. Kivelson, G.Tarjus, Nature Materials **7**, 831 (2008).

[18] G. B. McKenna, Nature Physics **4**, 672, (2008).

[19] T. Hecksher, A. I. Nielsen, N. B. Olsen, J. C. Dyre, Nature Physics **4**, 737, (2008).

[20] S. J. Rzoska, J. Zioło, Phys. Rev. E **59**, 2460, (1999).

[21] R. Richert, S. Weinstein, Phys. Rev. Lett **97**, 095703, (2006).

[22] C. Crauste-Thibierge, C. Brun, F. Ladieu, D. L'Hôte, G. Biroli, J-P. Bouchaud, Phys. Rev. Lett **104**, 165703, (2010).

[23] S. Brawer, *Relaxation in Viscous Liquids and Glasses,* American Ceramic Society, Columbus, (1985).

[24] C. A. Angell, J. Non-Cryst. Solids **131**, 13, (1991).

[25] P. G. Debenedetti, *Metastable Liquids: Concepts and Principles* (Princeton University Press, Princeton, NJ, 1996).

[26] N. Goldenfeld, *Lectures on Phase Transitions and theRenormalization Group*,(Addison-Wesley, Reading, MA, 19929.

[27] M. H. Cohen, D. Turnbull, J. Chem. Phys **31,** 1164, (1959).

[28] G. S. Grest, M. H. Cohen, "*Liquids, glasses, and the glass transition: A free-volume approach*" in Advances in Chemical Physics, edited by I. Prigogine and S. A. Rice Wiley, New York, Vol. 48, pp. 455–525, (1981).

[29] A. K. Doolittle, J. Appl. Phys **22**, 1471, (1951).

[30] G. Adam, J. H. Gibbs, J. Chem. Phys **43**, 139, (1965).

[31] K. G. Wilson, Rev. Mod. Phys **55**, 583, (1983).

[32] W. Götze, L. Sjögren, Rep. Prog. Phys **55**, 241, (1992).

[33] R. H. Colby, Phys. Rev. E **61**, 1783, (2000).

[34] B. M. Erwin, R. H. Colby, J. Non-Cryst. Solids **225**, 307, (2002).

[35] H. Vogel, Phys. Z **22**, 645, (1921).

[36] G. S. Fulcher, J. Am. Ceram Soc **8**, 339, (1925).

[37] G. Tammann, W. Hesse, Z. Anorg. Allg. Chem **156**, 245, (1926).

[38] R. Böhmer, K. L. Ngai, C. A. Angell, D. J. Plazek, J. Chem. Phys **99**, 4201, (1993).

[39] G. P. Johari, Phil. Mag. **86**, 1567, (2006).

[40] A. Drozd-Rzoska, S. J. Rzoska, Phys. Rev. E **73**, 041502, (2006).

[41] A. Drozd-Rzoska, S. J. Rzoska and C. M. Roland, J. Phys.: Condens. Matt. **20**, 244103, (2008).

[42] A. Drozd-Rzoska, S. J. Rzoska, M. Paluch, A. R. Imre, C. M. Roland, J. Chem. Phys **126**, 165505, (2007).

[43] S. J. Rzoska, A. Drozd-Rzoska, A. R. Imre,NATO Sci. Series II: *Metastable Systems under Pressure* p.95,(Springer Verlag, Berlin, 2010).

[44] I. Avramov, J. Non-Cryst. Solids **351**, 3163, (2005).

[45] A. Drozd-Rzoska, S. J. Rzoska, M. Paluch, J. Chem. Phys **129**, 184509, (2008).

[46] Y. S. Elmatad, D. Chandler, J. P. Garrahan, J. Phys. Chem. B **113**, 5563, (2009).

[47] J. C. Mauro, Y. Yue, A. J. Ellison, P. K. Gupta, D. C. Allan, PNAS **106**, 19780, (2009).

[48] S. C. Waterton, J. Soc. Glass Technol **16**, 244, (1932).

[49] P. Lunkenheimer, S. Kastner, M. Köhler, A. Loidl, Phys. Rev. E **81,** 051504, (2010).

[50] C. A. Angell, J. Non-Cryst. Solids **73,** 17, (1985).

[51] C. A. Angell, Science **267**, 5208, (1995).

[52] K. U. Schug, H. E. King, R. Böhmer, J. Chem. Phys **109**, 1472, (1998).

[53] A.V. Granato, J. Non-Cryst. Solids **307**, 376, (2002).

[54] J. C. Dyre, N. B. Olsen, Phys. Rev. E **69**, 042501, (2004).

[55] C. Kittel, *Introduction to Solid State Physics*, 7th ed.Wiley, New York, (1996).

[56] J. C. Martínez-Garcia, J. Ll. Tamarit, S. Capaccioli, M. Barrio, N. Veglio, L. C. Pardo, J. Chem. Phys **132**, 164516, (2010).

Chapter 2

Theoretical concepts of the dielectric relaxation

Macroscopic theories of dielectric phenomena are based on the pioneering work of Faraday [1] and Maxwell [2] and later work by Clausius and Mossotti and Lorentz [3,4]. These works provided the theory for introducing the Maxwell´s equations which summarizes the interaction of electromagnetic radiation with matter [5]. These equations allow getting information about relaxation phenomena related to molecular fluctuations of dipoles, as well as, the motion of mobile charge carriers which causes conductivity contributions to the dielectric response. From the macroscopic point of view, the basic principles of dielectrics have already been well understood at the beginning of the 20th century, being the work of Debye [6] which provided a vital connection between the macroscopic dielectric theory and the molecular structure.
This chapter is organized as follows. In the first part, the essential points of electrostatics are reviewed. The Kirkwood correlation factor for molecular systems is discussed. In the second part we focus on the dielectric properties under a periodic electric field. We review the theoretical and phenomenological aspects of the primary and secondary relaxation processes. The coupling-model equation is discussed and the corrective functions are introduced.

2.1 Dielectric in an electrostatic electric field

2.1.1 Macroscopic polarization

When an electric field is applied across the faces of a parallel plate capacitor containing a dielectric, the atomic molecular charges in the dielectric are displaced from their equilibrium positions and the material is said to be polarized. In general, a macroscopic polarization can be defined as the number of microscopic dipole moments of the molecules within a volume. In order to describe that effect, a vectorial magnitude $\vec{\mathbf{P}}$ is introduced, which quantifies the way a material reacts to an applied electric field $\vec{\mathbf{E}}$. This magnitude is called polarization, which has the dimension of a

surface charge density and is given by

$$\vec{\mathbf{P}} = \chi \varepsilon_0 \vec{\mathbf{E}} \tag{2.1}$$

where ε_0 is the permittivity constant of vacuum and χ the susceptibility of the material.

[1]For this simple linear case, the polarization is defined as a linear function of the electric field. The susceptibility is a material dependent and dimensionless quantity that describes the linear response reaction of a material to an electric field. This magnitude is related to the material static permittivity dielectric constant in a simple way

$$\chi_s = \varepsilon_s - 1 \tag{2.2}$$

where ε_s is the permittivity of the material

The microscopic dipole moments can have a permanent or an induced character caused by the local electric field which distorts a neutral distribution of charges, yielding numerous mechanisms which can contribute to the polarization, but they can be divided in two categories: (a) electronic polarization $\left(\vec{P}_e\right)$, which is the displacement of the electrons relative to the nucleus and (b) atomic polarization $\left(\vec{P}_a\right)$, which is the displacement of the atoms relative to one another. But, if a polar material is placed between the plates, a polarization in addition to the above mentioned two types will occur. This additional polarization is called orientational polarization $\left(\vec{P}_o\right)$. In short, the total polarization can then be written as

$$\vec{\mathbf{P}} = \vec{P}_e + \vec{P}_a + \vec{P}_o \tag{2.3}$$

The polarization corresponds then to the superposition of two contributions, the electronic and atomic polarization $\vec{P_{ind}} = \vec{P}_e + \vec{P}_a$ and the orientational polarization $\vec{P}_0$. On the other hand, the polarization describes too, the dielectric displacement which originates from the response of a material under the influence of an external field, defined as:

$$\vec{\mathbf{P}} = \varepsilon_0(\varepsilon_s - 1)\vec{\mathbf{E}} = \chi \varepsilon_0 \vec{\mathbf{E}} \tag{2.4}$$

Each one of the three aforementioned contributions is a function of the frequency for an applied alternating electric field. Suppose that we apply an alternating field to the parallel-plate capacitor filled with polar material. The orientation of the material under consideration will be related with the direction of the electric field. When the frequency of the applied field is sufficiently low, all types of polarization will reach the same value as they show in the steady field, which is equal to the

[1]For higher field strengths $(> 10^6 Vm^{-1})$[5]non linear effects may take place. The equation (2.1) can be extended to include higher order terms:

$$P = \chi \varepsilon_0 E + \chi_1 \varepsilon_0 E^2 + \chi_2 \varepsilon_0 E^3 + ...$$

instantaneous value of the alternating electric field. But, as the frequency is raised, the polarization no longer has the time to reach its steady value. This requires studying how the particles respond to the influence of external static or alternating electric field.
There are two aspects that will be addressed, namely the response of the individual particle to an electric field, and the possible modification of the response to an external field by the interaction between the particles. As a starting point, the link between the dielectric phenomena on a macroscopic scale and on the molecular level is needed. The best way to establish such a link is to relate the polarization to the static dielectric constant being done in two ways, (1) the oldest and simplest way based on the concept of the internal or local field introduced by Lorentz, and (2) the more modern approach put forward by Onsager and Froehlich, which is basically to consider the fluctuations occurring at microscopic level.

2.1.2 Onsager and Kirkwood-Froehlich equation

The oldest theories based on the local field are valid only for certain conditions [6-10]. The modern approach put forward by Onsager and Froehlich is more general and based on the statistical mechanical theory of matter [11-14]. The methods of statistical mechanics provide a way for obtaining macroscopic quantitative magnitudes when the related properties of the molecules and the molecular interactions are known. Based on the principles of statistical mechanics and fluctuation-dissipation theorem, e.g. described by Kittel [15], it can be shown that the 'static susceptibility' of the process is given by:

$$\chi_s = \frac{\sum_{i,j=1}^{N} \langle \vec{\mu}_i \vec{\mu}_j \rangle}{3K_B T} \tag{2.5}$$

where the brackets denote a statistical mechanical average of the dipole moments of the system, K_B is the Boltzmann constant and T the temperature in Kelvin. This dipole moment is non-zero even in the absence of any external electric field, and therefore gives account of the spontaneous fluctuations of the electric charge occurring in the system as a result of the thermal energy.
This equation originally results if the system is considered as a thin dielectric slab. But for convenience, it is better to consider a model of a sphere of volume V containing N molecules, immersed in vacuum or embedded in its own medium extending to infinity. The material outside the sphere is treated as a continuum with dielectric constant ε. Based on the continuum approach, for non-polarizable molecules Froehlich showed that

$$\chi_s = \frac{(\varepsilon_s - 1)(2\varepsilon_s + 1)V\varepsilon_0}{3\varepsilon_s} \tag{2.6}$$

This equation applies to any system being solid, liquid, or gas, which is evaluated on the assumption that there are not intermolecular forces and induced dipoles. The statistical mechanical

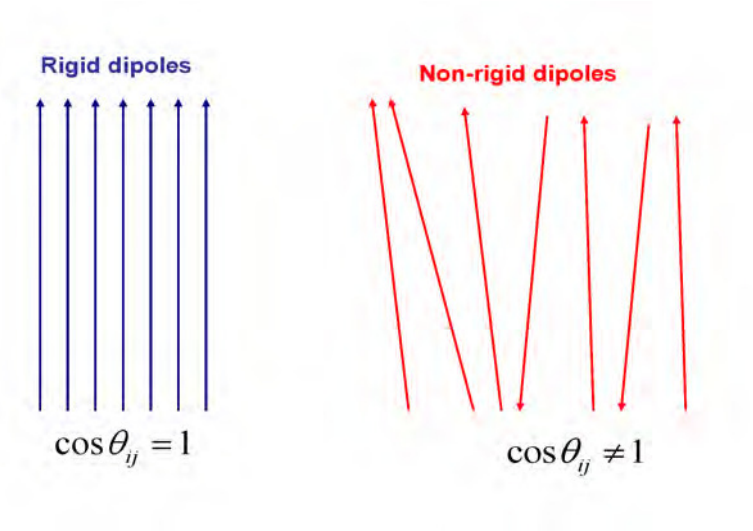

Figure 2.1: *Schematic drawing of two typical cases of dipolar correlation*

average of the dipole moments of the system in case of non-interacting dipoles can be calculated as the average of their scalar product

$$\sum_{i,j=1}^{N} \langle \vec{\mu}_i \vec{\mu}_j \rangle = \mu^2 \sum_{i,j=1}^{N} \langle \cos\theta_{ij} \rangle = N\mu^2 \tag{2.7}$$

The above equation can be written then as

$$\frac{N\mu^2}{VK_BT} = \frac{(\varepsilon_s - 1)(2\varepsilon_s + 1)\varepsilon_0}{\varepsilon_s} \tag{2.8}$$

However, it is well known that liquids and solids, in fact condensed systems, are characterised by short-range as well as long range forces. Therefore correlation between the orientations, also between the positions, will lead to differing values of $\langle \vec{\mu}_i \vec{\mu}_j \rangle$. Kirkwood introduced a correlation factor to account for this difference [11,16]. This correlation factor models the interaction between dipoles with respect to the ideal case of non-interacting dipoles, which are known at the literature as rigid dipoles [10]. In general the Kirkwood-Froehlich correlation factor can be defined by

$$g = \frac{\mu^2_{interact}}{\mu^2} = \frac{\left\langle \sum_{i=1}^{N} \mu_i \sum_{j=1}^{N} \mu_j \right\rangle}{N\mu^2} = 1 + \frac{\left\langle \sum_{i}^{N} \sum_{i<j}^{N} \mu_i \mu_j \right\rangle}{N\mu^2} \tag{2.9}$$

Taking in to account that for non-rigid dipoles $\varepsilon_\infty > 1$, and the equations (2.8) and (2.9), the correlation factor can be written as

$$g = \frac{(\varepsilon_s - \varepsilon_\infty)(2\varepsilon_s + \varepsilon_\infty) VK_BT\varepsilon_0}{3\varepsilon_s N\mu^2} \tag{2.10}$$

In a simple picture, $g = 1 + z\langle \cos(\theta_{ij}) \rangle$[10], where z is the number of the nearest neighbour

surrounding the molecule, and $\langle \cos(\theta_{ij}) \rangle$ is the mean value of the cosine of the angle between the dipole moments of adjacent molecules. The figure (2.1) shows two representative cases of the dipolar correlation. For the case of rigid dipoles the relative angle between them is zero, and $g > 1$. For non-rigid dipoles the Kirkwood factor would take values smaller than the unity.
The Kirkwood parameter g is in fact a tensor, but practically in all applications one can consider it as a scalar. When there is no correlation between the molecular dipoles, the g value is the unity. But the value of g can be greater than unity, when dipoles are aligned in parallel. If the molecular dipoles tend to align anti-parallel (as will be the case for some cases in this thesis) the value is less than unity. In these cases, the dipole moment μ is not simply that of an isolated molecule, which is modified by its polarization. It can be shown that, in this case

$$\mu_g = \frac{3\mu}{\varepsilon_\infty + 2} \tag{2.11}$$

where μ_g is the dipole moment of the molecule in the gas phase and ε_∞ is the permittivity at the optical frequency (which is defined as the square of the refractive index).
Inserting the above equations, into the equation (2.10), one obtains the Kirkwood –Froehlich equation

$$\mu_g^2 g = \frac{9\varepsilon_0 K_B M T (\varepsilon_s - \varepsilon_\infty)(2\varepsilon_s + \varepsilon_\infty)}{N_A \rho \varepsilon_s (\varepsilon_\infty + 2)^2} \tag{2.12}$$

where N_A is Avogadro's number, and M is the molecular weight. When $g = 1$, the above equation reduces to a simple equation

$$\mu^2 = \frac{9\varepsilon_0 K_B M T (\varepsilon_s - \varepsilon_\infty)(2\varepsilon_s + \varepsilon_\infty)}{N_A \rho \varepsilon_s (\varepsilon_\infty + 2)^2} \tag{2.13}$$

The latter equation was already derived by Onsager before Kirkwood's theory and is generally denoted as Onsager equation. In the derivation of Onsager equation, it is supposed that particles are spherical and that no specific molecular interactions between the particles occur. One can therefore consider the Kirkwood-Froehlich equation (2.12) as the generalization of the Onsager equation (2.13).

2.1.3 Kirkwood effective correlation factor (g^{eff})

Theories providing insight into the microscopic origin of the molecules dynamics are still lacking, and thus many experimental and simulation works focus on such a problem by characterizing the dynamics of mono-component systems for which dynamics is analyzed throughout the change of temperature and/or, sporadically, pressure. Another way to change the molecular surrounding of a relaxing entity and thus of the involved cooperativity, consists on mixing different entities [17-19]. The mixture of N compounds formed by molecules displaying a dipole moment μ_i with mole fraction of the species X_i where $(i = n_1 .....n_N)$ is known as multicomponent system. Those systems

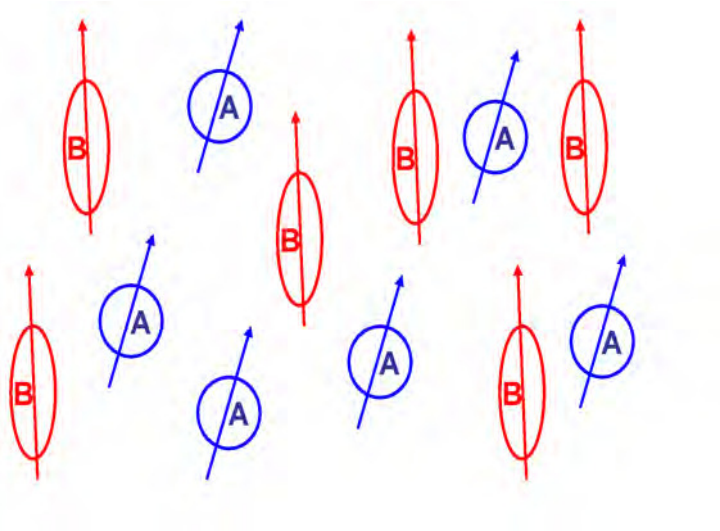

Figure 2.2: *Schematic drawing of a dipolar system formed by molecules of two pure compounds* (A, B). *Its molecules have a permanent dipolar moment.*

consisting of only two components $(n_1 = A, n_2 = B)$ will define the binary systems as follows $A_{1-x}B_x$ where x is the mole fracion of the B component.
As compared to neat systems, binary systems have been dielectrically studied so far to a lesser extent. In particular, the binary mixtures studied in this work are formed by:

1. Both compounds are formed by molecules with dipoles moment.

2. Only one of the compounds has a dipolar molecule, whereas the other one is devoided of the dipolar moment.

Due to recent developments in experimental capabilities, dielectric spectroscopy technique offers the advantage to study the dynamics, over much wider time/frequency ranges. The study of binary systems corresponding to case (2) has the advantage that the dipolar molecules are selectively monitored, whereas their density can be modified by means of mole fraction. As for systems of the case (1), molecular cooperativity and dynamical heterogeneity can be analysed.
In the last section, the orientation and short-range interaction between electric dipoles in a pure polar compound was introduced. How is this equation modified when considering a binary system? As a consequence of mixing effects, the dipole moments of the system μ, the molecular weight M as well as the density ρ, will depend on the composition. In addition, the new Kirkwood equation must recover the limiting cases of pure compounds

$$\lim_{X\to 1,0} g^{eff}(X,T) = \begin{cases} g_A & X_A \to 1 \\ g_B & X_B \to 1 \end{cases} \tag{2.14}$$

Mehrotra et al [20-22] modified the equation (2.13) by considering that for polar binary mixtures the short-range interaction can be described by the molecular association effects, providing the effective Kirkwood factor:

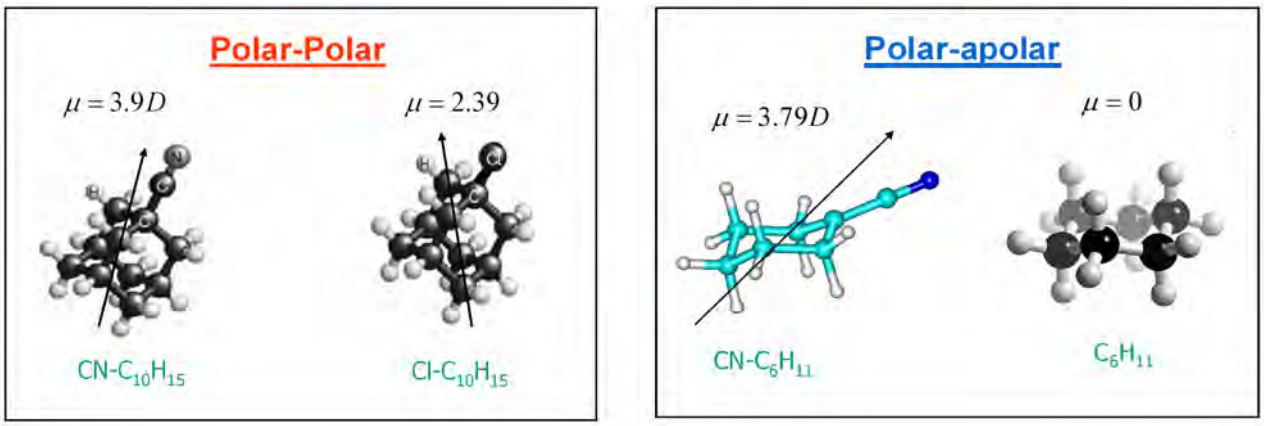

Figure 2.3: *Schematic drawing of polar and apolar molecules of two binary systems. The red one corresponds to the case of a system where both molecules have a permanent dipole moment and the blue one to the case where one of the pure compounds does not has a dipolar permanent moment.*

$$\frac{N_A}{9\varepsilon_0 K_B T}\left(\frac{\mu_A^2 \rho_A}{M_A} X_A + \frac{\mu_B^2 \rho_B}{M_B} X_B\right) g^{eff}(X,T) = \frac{(\varepsilon_s - \varepsilon_\infty)(2\varepsilon_s + \varepsilon_\infty)}{\varepsilon_s(\varepsilon_\infty + 2)^2} \tag{2.15}$$

Taking into account that $\frac{V}{N_{mol} N_A} = \frac{M}{\rho}$ the above equation can be written as

$$g^{eff}(X,T) = \frac{9\varepsilon_0 K_B T M(X)}{\rho(X,T)} \frac{1}{\left[\mu_A^2 X_A + \mu_B^2 X_B\right]} \frac{(\varepsilon_s - \varepsilon_\infty)(2\varepsilon_s + \varepsilon_\infty)}{\varepsilon_s(\varepsilon_\infty + 2)^2} \tag{2.16}$$

The temperature dependence of the static and infinity dielectric permittivity can be determined using the dielectric spectroscopy technique, and the available volume $V(X,T)$ will straightforwardly be calculated from the lattice parameters obtained from the X-ray diffraction for the solid state cases or form direct measurement of the density in the liquid state case [23]. The above equation will have a great experimental application for estimating the short-range interactions in binary systems.

2.2 Dielectric in a periodic electric field

2.2.1 Complex dielectric permittivity

The static dielectric constant discussed above applies only when the external field remains in a steady state. Much of interest in the dielectric studies is, however, concerned with frequency-dependent phenomena, where dielectric dispersion occurs, because dynamic information can be obtained.

When an electric field is applied as step function to a group of dipoles, all the three types of polarization mentioned earlier get affected. Induced polarization is, however, very fast and can be assumed to rise instantaneously. In contrast, the orientational polarization is slow and lags

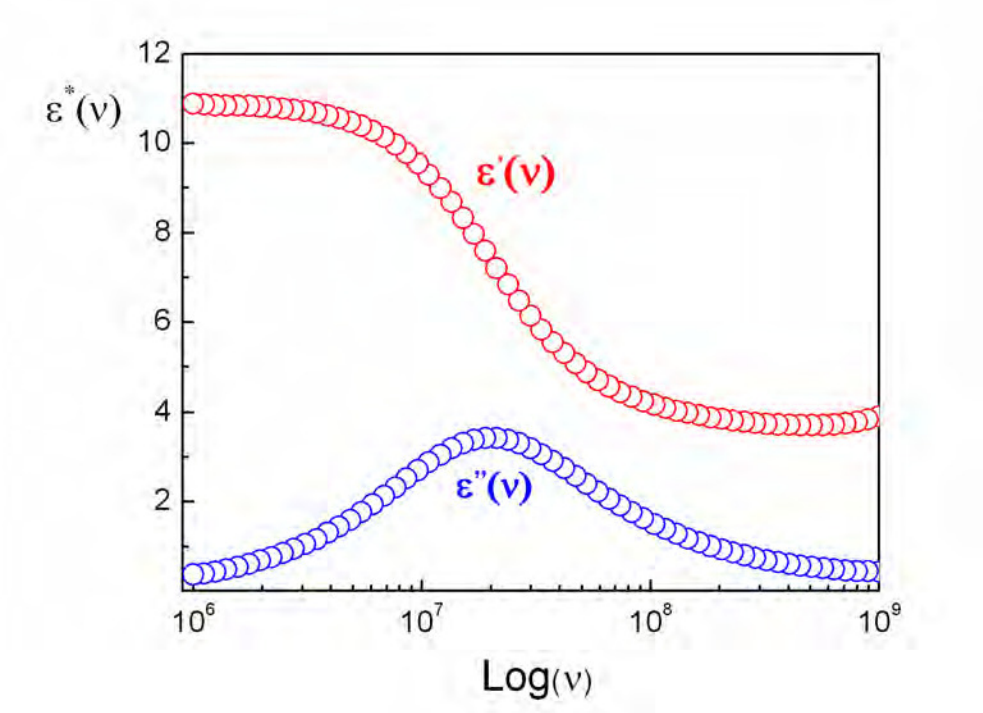

Figure 2.4: Result of the experimental dielectric permittivity measurement of cyclooctanol (C8-ol). The measurement has been performed at $T = 283K$. The blue and red points represent the imaginary and the real dielectric permittivity part.

behind the rise of the electric field. As opposed to the response of a vacuum, the response of normal materials to external fields generally depends on the frequency of the field. This frequency dependence reflects the fact that a material polarization does not respond instantaneously to the applied field. The response must always be causal (arising after the applied field) which can be represented by a phase difference.

The application of the periodic electric field $E(t) = E_0 \exp[-i\omega t]$ with angular frequency $\omega = 2\pi\nu$, to a group of dipoles results in the phase shift between electric field $\vec{\mathbf{E}}$ and the polarization $\vec{\mathbf{P}}$. Under such conditions, a dissipation of electrical energy occurs, and the dielectric constant has to be treated as a complex dielectric or permittivity function

$$\varepsilon^{\star}(\omega) = \varepsilon^{'}(\omega) - i\varepsilon^{''}(\omega) \tag{2.17}$$

where $\varepsilon^{'}(\omega)$ and $\varepsilon^{''}(\omega)$ are the real and imaginary parts, respectively (see figure 2.4).

The real part is related to the reversible energy stored in the material, and the imaginary part is proportional to the dissipated energy which will provide quantitative information about the relaxation process associated with the reorientation of the dipoles. Using the dielectric spectroscopy technique, we can extract both complex dielectric parts. The imaginary part appears as an asymmetric peak for which its maximum will define the relaxation time evolution $\tau(T)$ at the temperature of the systems, and quantitative information about the molecular interactions. On the other

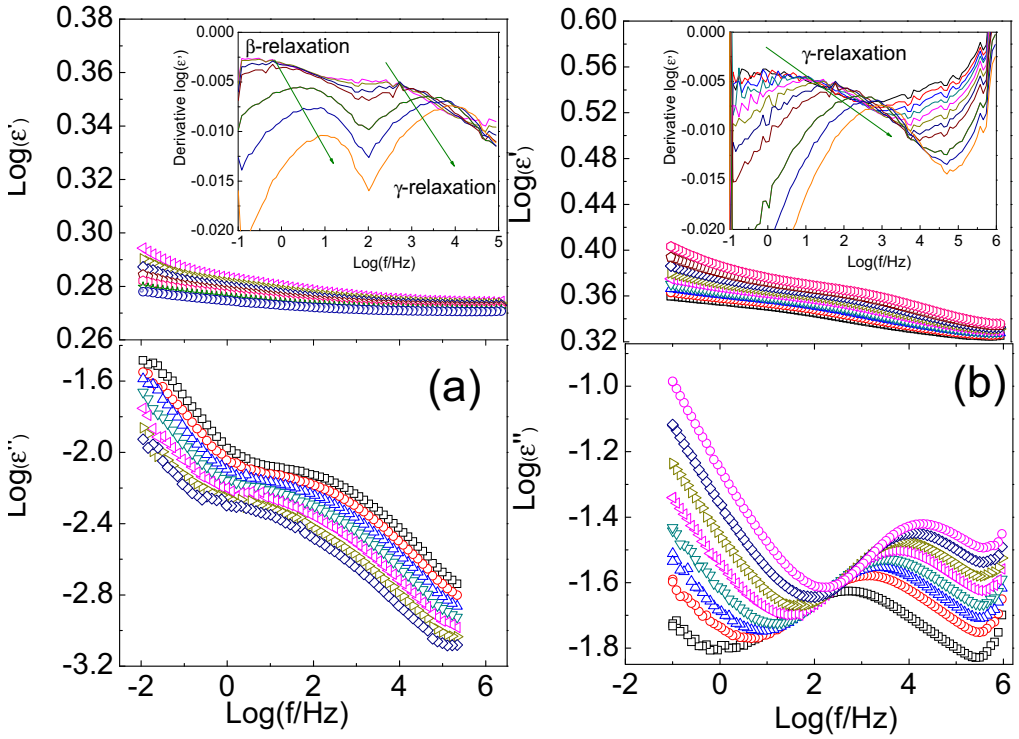

Figure 2.5: *Real (top panels) and imaginary (bottom panels) parts of the complex dielectric permittivity for temperatures lower than the glass transition temperatures as a function of frequency for two mixed crystals,* $(C7-ol)_{0.14}(C8-ol)_{0.86}$*(a) and* $(C7-ol)_{0.39}(C8-ol)_{0.61}$*(b). Insets correspond to the derivative with respect to the frequency.*

hand, the real part is related with the dielectric strength, which gives a link between macroscopic and microscopic properties.

The Kramers–Kronig relationships describe how the real and imaginary part of $\varepsilon^{\star}(\omega)$ are related to each other. The consequence is that it suffices to know the imaginary part for getting the full complex $\varepsilon^{\star}(\omega)$ since the real part can be calculated from the imaginary part, and of course vice versa. The derivation of the Kramers-Kronig relations can be found in the book of Bottcher and Boderwijk [8,9]. They used the Cauchy integral theorem along a closed contour inside a complex region, as well as, the complex conjugated properties of dielectric permittivity. In short, it is shown, based on the superposition principle, that $\varepsilon^{\star}(\omega)$ can be expressed as the Laplace transformation of a pulse response function with certain properties. Complex integration allows deriving the Kramers–Kronig relations:

$$\varepsilon^{'}(\omega)-\varepsilon_{\infty}=\frac{2}{\pi}\int_{0}^{\infty}\frac{\xi\varepsilon^{''}(\xi)}{\xi^{2}-\omega^{2}}d\xi \tag{2.18}$$

$$\varepsilon^{''}(\omega)=\frac{2}{\pi}\int_{0}^{\infty}\frac{\xi\varepsilon^{'}(\xi)}{\xi^{2}-\omega^{2}}d\xi \tag{2.19}$$

The mutual dependence between both magnitudes can be useful for testing the existence of relax-

ation process. In the range below the glass transition temperature T_g where we observe secondary relaxation processes, the real part of the permittivity stays almost constant at values higher than the imaginary part. The relaxation processes will be indentified as an inflexion point in the real part of the permittivity giving rise to a useful procedure for testing the existence of relaxation processes [24,25] (see figure 2.5).

2.2.2 Other phenomena

The expressions given in the previous paragraphs describe the orientational polarization. The polarization at high frequencies (short time scales) is summarized by a dielectric constant ε_∞. The only additions to be made are at low frequencies (long time scales). In this regime, the movements of charge carriers through the samples become important and it can be observed in the dielectric spectra.

The first phenomenon is the electrical conduction. This simple movement of charge carriers leads typically to a response that is the same as an ohmic conductor. As a consequence, the drift motion of mobile charge carriers causes conductivity contributions to the dielectric response and the conduction current is not negligible. This current density is related with the electric field and the derivative of dielectric displacement by the Ohms law and Maxwell's equation giving rise the following relationship

$$\sigma^\star(\omega)\vec{E} = -\frac{d\vec{E}}{dt} = i\omega\varepsilon_0\varepsilon^\star(\omega)E_0\exp[-i\omega t] \tag{2.20}$$

This relationship provides us the connection between the complex dielectric permittivity and the complex conductivity, which can be written as

$$\sigma^\star(\omega) = i\omega\varepsilon_0\varepsilon^\star(\omega) \tag{2.21}$$

The contribution of the conductivity to the imaginary part of the dielectric permittivity is acounted by addition of a term, in such a way that we can write:

$$\varepsilon^{''}(\omega) = \varepsilon_{relaxation} + \frac{\sigma_0}{(\varepsilon_0\omega)^s} \tag{2.22}$$

The first term of that equation gives us information about the dielectric relaxation which will be discussed in the next section. The second term will define the conductivity additive contribution where s defines a phenomenological exponent that has a value of $s = 1$ for pure ohmic conduction and σ_0 is the DC electrical conductivity. Note that because of its purely imaginary character this term only contributes to the imaginary part $\varepsilon^{''}(\omega)$.

Electrode polarization can be seen as a large rise of $\varepsilon^{'}(\omega)$ at low frequencies. The explanation is that, for slowly varying fields, the mobile charge carriers can reach the electrodes. This occurs because they cannot leave the sample and they build up a charged layer. This layer masks the

electric field in the bulk of the actual sample and gives rise to an increase in $\varepsilon^{'}(\omega)$. Since electrode polarization does not tell much about the sample (actually because it contains free charges), the part with the electrode polarization is often excluded from the analysis. If for some reason it is necessary to include this part, it is fitted with a power law in the real part of complex permittivity:

$$A\omega^n \tag{2.23}$$

The exponent n reaches values typically in the order of -1.5 to -2. A consequence of electrode polarization is that the power law of the conductivity contribution changes, and that a second power law for the conductivity is necessary. The Maxwell–Wagner effect [5,26] is equivalent to electrode polarization, but in this case, the charges accumulate at the internal boundaries of a heterogeneous sample. In the dielectric spectra this shows up as an ordinary relaxation process.

2.3 Primary α-relaxation

In the study of the dynamics of glass forming systems, attention has been payed to the process known as primary or α-relaxation, which characterizes the dynamics of the structural rearrangement of the molecules directly and which is the origin of the glass transition phenomenom. In the present section we will present equations for the frequency dependence of the complex dielectric constant which should hold for the cases of dilute solutions of dipoles in liquids. These equations were first established by Debye [6,10] who considered dipoles with identical relaxation time, relaxing independently to each other for the description of the α-relaxation. This consideration seems unrealistic because in most materials the Debye consideration fails to describe the experimental results. The loss peaks caused by the primary relaxation are broader and often asymmetric, two aspects which are against the simple Debye model. The impossibility for predicting an analytical model solution to this striking behaviour, gives rise to the introduction of phenomenological frequency- dependent equations.

2.3.1 Debye model

Debye theory considers the reaction of dipolar non-interacting molecules with a common relaxation time when an electric field is applied. If we assume that the time scale of the relaxation process is clearly separated from faster processes that may be present in the material, an almost instantaneous polarization P_∞ due to the fast processes will occur as shown in figure (2.6). According to the Debye model, dipoles will relax (i.e., come back to the original equilibrium state) with a rate proportional to the difference from the instantaneous polarization to that at the equilibrium state. The rate of increase of orientation polarization $P_0(t)$ during transient period will be described by a first order differential equation given by

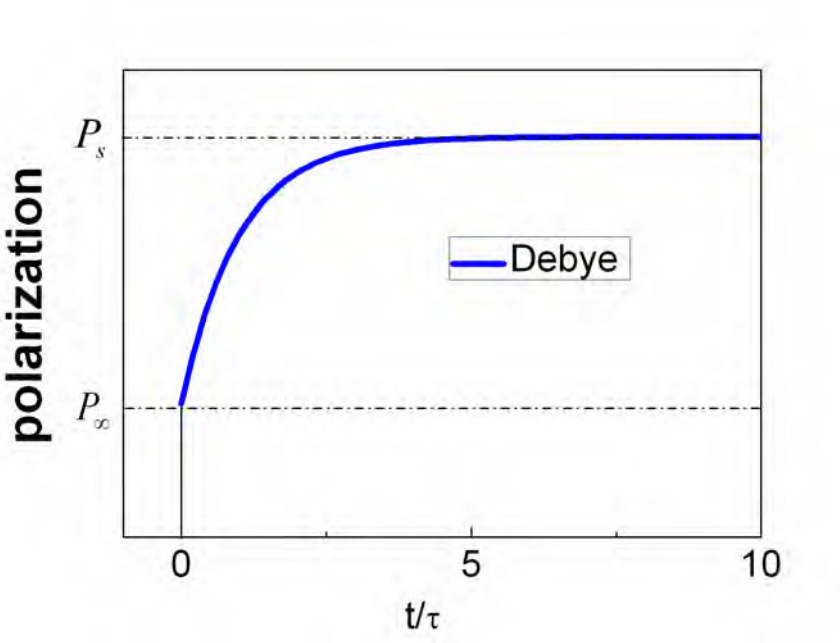

Figure 2.6: *Polarization time dependence of a material after the application of an electric field at t=0. The blue line shows the theoretical response of dipolar non-interacting entities with a commoon relaxation time (Debye model).*

$$\frac{dP_0(t)}{dt} = \frac{P_s - P_0(t)}{\tau_D} \tag{2.24}$$

where P_s is the static polarization and τ_D is a characteristic relaxation time.
Defining $u = P_s - P_0(t)$ the above differential equation can be written as

$$\int_{P_s-P_\infty}^{P_s-P_0(t)} \frac{du}{u} = -\int_0^t \frac{dt}{\tau_D} \tag{2.25}$$

and integrating the equation (2.25) results in an exponential approach to the static polarization P_s

$$P_0(t) = P_s + (P_\infty - P_s)\exp\left[-\frac{t}{\tau_D}\right] \tag{2.26}$$

The application of a Fourier transformation leads to the following expression:

$$\varepsilon^\star(\omega) = \varepsilon_\infty + \frac{\varepsilon_s - \varepsilon_\infty}{1 + i\omega\tau_D} \tag{2.27}$$

Equation (2.27) is known as the Debye equation where ε_s and ε_∞ are the low and high frequency limits of dielectric constant, determined by all slower and faster processes that may be present in the investigated material. The real and imaginary part leads to a sigmoidally shaped curve for $\varepsilon^{'}(\log_{10}\nu)$ and to symmetric loss peaks with half widths of 1.14 decades for $\varepsilon^{''}(\log_{10}\nu)$ as showed in the figure (2.7).

Introducing the frequency domain response function to the the Debye equation, it can also be written in another equivalent way as:

$$\Phi^{\star}(\omega) = \frac{\varepsilon^{\star}(\omega) - \varepsilon_{\infty}}{\varepsilon_s - \varepsilon_{\infty}} = \frac{1}{1 + i\omega\tau_D} \tag{2.28}$$

This equivalent way for the Debye equation will be very important for the microscopic treatment of dielectric phenomena. The left part of this equation is related by Fourier transformation with a simple exponential decay function $\phi = \exp\left[-\frac{t}{\tau_D}\right]$ as

$$\Phi^{\star}(\omega) = \mathscr{F}\left[-\frac{d\phi(t)}{dt}\right] \tag{2.29}$$

What is the physical meaning of the exponential decreasing polarization function that appears as a result of the Debye model? Thermodynamic quantities which characterize a macroscopic sample are average values [27]. Due to the stochastic movement of the molecules these quantities fluctuate around their mean values. Under the electric field effect the induced polarization is, however, very fast and can be assumed to rise instantaneously and it will fluctuate as a consequence of reorientacional dipolar movement.
Taking in to account this consideration, the dipolar fluctuation can be described by a normalized correlation function which for the Debye model leads the same exponential decay function

$$\phi(t) = \frac{\langle \triangle P(t) \triangle P(0) \rangle}{\langle \triangle P(0)^2 \rangle} = \exp\left[-\frac{t}{\tau_D}\right] \tag{2.30}$$

The assumption of dipoles with identical relaxation time (homogenous scenario), relaxing independently to each other allows an analytical connection between the frequency and time domain, giving rise to a link between macroscopic and microscopic properties.

In complex real systems, the dipoles interact with each other and the equation (2.30) will also remain valid, but with a stretched exponential and an asymmetric function for the time and frequency domains respectively. In real cases, the equation (2.29) has not analytical solution [28,31]; several numerical methods have been used for calculating the Fourier transform and to interpret relaxation data from spectroscopy in the frequency domain. However, it is also well known that the computation of the Fourier transform has numerical problems originating from unwanted oscillations effects, especially when treating real data. Phenomenological functions need then to be introduced. A brief description about these functions is given in the next section.

2.3.2 The Havriliak-Negami (HN) equation

Complex dielectric spectra of certain systems reported in the literature show multiple relaxation time behaviour. The spectra of such systems show deviations from the Debye dispersion curve. It is a striking fact that, despite of the variety of materials used and of experimental techniques employed such as photon correlation spectroscopy, mechanical relaxation experiments, as well as

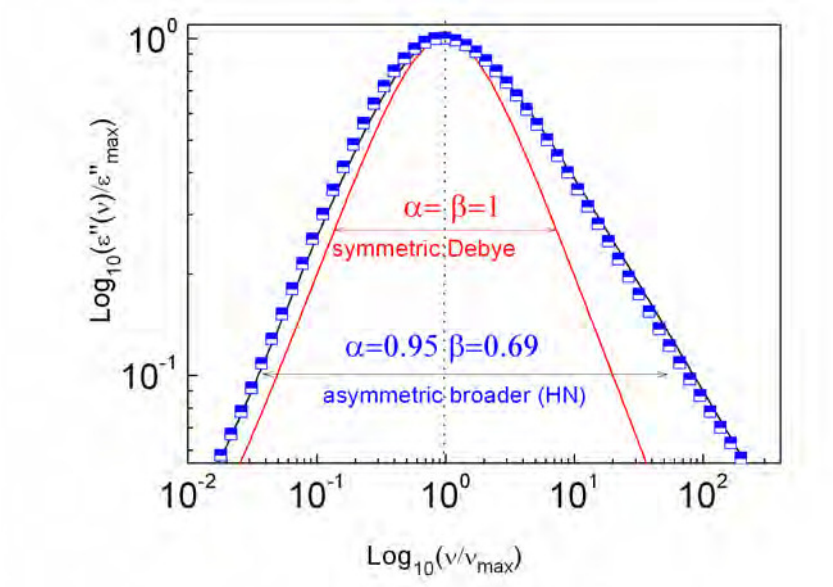

Figure 2.7: *Result of the experimental imaginary dielectric permittivity measurement of (C8-ol)(blue points) at $T = 185K$. The functions are normalized at the frequency and permittivity values of the maximum. The blue and red line represents the fits of (HN) function and the ideal Debye case,respectively.*

dielectric spectroscopy, the relaxation behaviour is very similar. Rigorous theories which fully describe the observed behaviour have not yet been developed. As a result, almost all the experimental data have been represented in terms of empirical functions in the frequency and time domain. The representation of the dispersion curve therefore needs some mathematical modifications to the Debye equation. For this purpose, empirical fitting functions were suggested.

In the frequency domain, the imaginary part of response function is broader than that corresponding to a Debye process (1.14 decades width at half maximum as is showed at the figure (2.7)). This width has been modelled by different empirical functions, such as the Cole and Cole function [32], the Fuos and Kirkwood function [33], the Cole and Davidson [34] function, the Jonscher function [35], where the common characteristic for all of them is the power law dependences at high and low frequencies. The Havriliak and Negami (HN) function has been the most extensively used in literature [36] and can be defined by the following equation:

$$\Phi^*_{HN}(\omega) = \frac{\varepsilon^*_{HN}(\omega) - \varepsilon_\infty}{\varepsilon_s - \varepsilon_\infty} = \frac{1}{[1 + (i\omega\tau_{HN})^\alpha]^\beta} \tag{2.31}$$

where α and β are shape parameters ranging between 0 and 1 and τ_{HN} is a characteristic relaxation time. The Cole-Cole(CC) function corresponds to the case $0 < \alpha < 1$ and $\beta = 1$ and the Cole-Davidson to $\alpha = 1$ and $0 < \beta < 1$. The Debye case is recovered with $\alpha = \beta = 1$.
The separation of the real and imaginary parts gives a rather complex expression for $\varepsilon^{'}(\omega)$and $\varepsilon^{''}(\omega)$ written by

$$\varepsilon^{'}(\omega) = \varepsilon_{\infty} + \Delta\varepsilon \frac{\cos(\beta\varphi)}{[1+(\omega\tau_{HN})^{\alpha}\sin(\pi\alpha/2)+(\omega\tau_{HN})^{2\alpha}]^{\beta/2}} \tag{2.32}$$

$$\varepsilon^{''}(\omega) = \Delta\varepsilon \frac{\sin(\beta\varphi)}{[1+(\omega\tau_{HN})^{\alpha}\sin(\pi\alpha/2)+(\omega\tau_{HN})^{2\alpha}]^{\beta/2}} \tag{2.33}$$

where $\Delta\varepsilon = \varepsilon_s - \varepsilon_{\infty}$ describes the dielectric strength and φ also known as loss angle is defined as

$$\varphi = \arctan[(\omega\tau_{HN})^{\alpha}\frac{\cos(\pi\alpha/2)}{1+(\omega\tau_{HN})^{\alpha}\sin(\pi\alpha/2)}] \tag{2.34}$$

Although (HN) equation has 5 fitting parameters, the advantage for obtaining relaxation data in the frequency domain makes of this equation one of the most extensively used in literature.

2.3.3 The Kohlrausch Williams Watts (KWW) function

In the time domain the dipole normalized correlation function is more stretched than a simple exponential which would correspond to a Debye process as can be seem in figure (2.8). It has been observed over the past 15 years that experimental frequency-dependent dielectric constant for a broad class of materials may be interpreted in terms of the Kohlrauch-Williams-Watts function which often proves to be more appropriate in modelling relaxation processes of non-exponential character.

This function was introduced by Kohlrausch as early as 1847 to describe the mechanical creep in glassy fibres [37]. Williams and Watts modified it to describe relaxation processes in polymers [38] leading to the following functional form:

$$\phi_{KWW}(t) = \exp\left[-(\frac{t}{\tau_{KWW}})^{\beta_{KWW}}\right] \tag{2.35}$$

where τ_{KWW} represents the characteristic relaxation time and β_{KWW} is a stretching exponent ranging between 0 and 1 which depends on the material and fixed external conditions such as temperature and pressure. In fact, the equation (2.35) is a modified form of equation (2.30).

At short times (high frequencies), the stretching exponent leads to an asymmetric broadening of $\phi_{KWW}(t)$ compared with a simple exponential decay showed in figure (2.8). At the glass transition temperature T_g, the β_{KWW} exponent has been related with the fragility of the material by an empirical linear decreasing function [39], which allows the conection between a Debye process with complex interacting systems

The above function can be correctly described from the mathematical point of view as a superposition of uncoupled Debye processes, weighted by a broad distribution of relaxation time functions $\rho_{KWW}(\tau)$

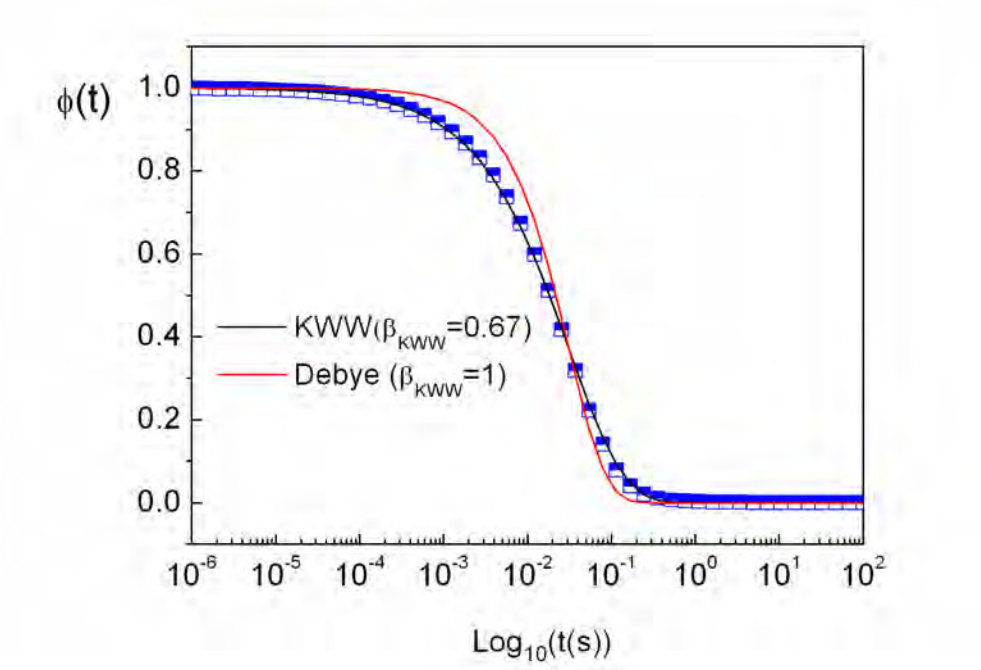

Figure 2.8: *Kohlrauch-Williams-Watts (KWW) functions for the ideal case of Debye process (red line β_{KWW}=1) and the case of an isotherm $T = 185K$ of (C8-ol)(blue line $\beta_{KWW} = 0.67$). The points have been obtained by a numerical Fourier Transformation of the imaginary dielectric part [40].*

$$\exp\left[-(\frac{t}{\tau_{KWW}})^{\beta_{KWW}}\right] = \int_0^\infty \exp\left[-(\frac{t}{\tau_{KWW}})\right] \rho_{KWW}(\tau) d\tau \tag{2.36}$$

The above equation has some restrictions related to the feasibility of the function itself. First, the physical meaning of the Williams-Watts distribution function is not completely clear. Therefore, in many of the calculations it can be regarded only as a potential mathematical tool. Furthermore, the analytical evaluation of equation (2.36) remains as a critical problem and appears more complicated, although some attempts have been made to solve the issue [41]. Moreover, it is not possible to provide a closed analytical expression for $\varepsilon^\star(\omega)$ for the KWW function. These problems render the KWW representation difficult to apply. However, fortunately there are ways to circumvent the above mathematical problems. To this end, some numerical expressions have been derived which allow the connection between the HN shape parameters and the KWW stretched parameter. Discussions of these analytical expressions are given in the subsequent section.

2.3.4 Interconnection between frequency and time domain

Computation of the distribution function by calculating the preceding integral of the equation (2.36) is not an easy mathematic problem. This integral can be evaluated in an alternative way introducing an integral series transformation. There are terms of the series which can get values

some orders of magnitude larger than the final result. On the other hand, algorithms which yield values for trigonometric functions can fail when their arguments are high, and this can become another source of error. The main problem is how to calculate or to modelate the relaxation time distribution function. Two examples commonly used are described in the next sections.

2.3.4.1 Alvarez-Alegria -Colmenero relatioships (AAC)

Patterson and Lindsay [42] derived a relationship between the Cole-Davidson and KWW functions. This work was extended by Alvarez et al [43] which interrelated the Havriliak-Negami (HN) and the Kohlrauch-Williams-Watts (KWW) functions using the numerical iterative Adachi-Kotaka algorithms [44] and the Provencher's CONTIN program [45]. They found a connection between the HN exponents (α,β) and the stretching parameter β_{KWW}, as well as a relationship between the associated relaxation times:

$$\beta_{KWW} = (\alpha\beta)^{1/1.23} \tag{2.37}$$

$$\ln\left(\frac{\tau_{HN}}{\tau_{KWW}}\right) \backsimeq 2.6(1-\beta_{KWW})^{1/2}\exp[-3\beta_{KWW}] \tag{2.38}$$

The validity of the above equations was tested by means of dielectric measurements, performed around the primary relaxation. Two spectroscopic techniques were used: one acting in the time domain called the transient current method which measures the depolarization current of a constant dc voltage and the other in the frequency domain, the Broadband dielectric spectroscopy (BDS) yielding an accurate description of real data [43,46]. Nevertheless, these relationships cannot be an analytical one, since it is known that the HN and the KWW relaxation functions are not exactly Fourier transforms of each other, but is one of the most extensively relationship used in the experimental results reported in literature

2.3.4.2 Generalized gamma distribution. Rajagopal function

Another way to connect both domains is modelating the relaxation time distribution function. Using the logarithmic Stilje-transformation [47,48], the above analytical functions for the time and frequency domains can be written as a superposition of the Debye processes with different relaxation time as follows:

$$\varphi(t) = \int_{-\infty}^{\infty} g(\log\tau)\exp\left[-\frac{t}{\tau}\right] d\log\tau \tag{2.39}$$

$$\Phi^*(\omega) = \int_{-\infty}^{\infty} g(\log\tau)\frac{1}{1+i\omega\tau} d\log\tau \tag{2.40}$$

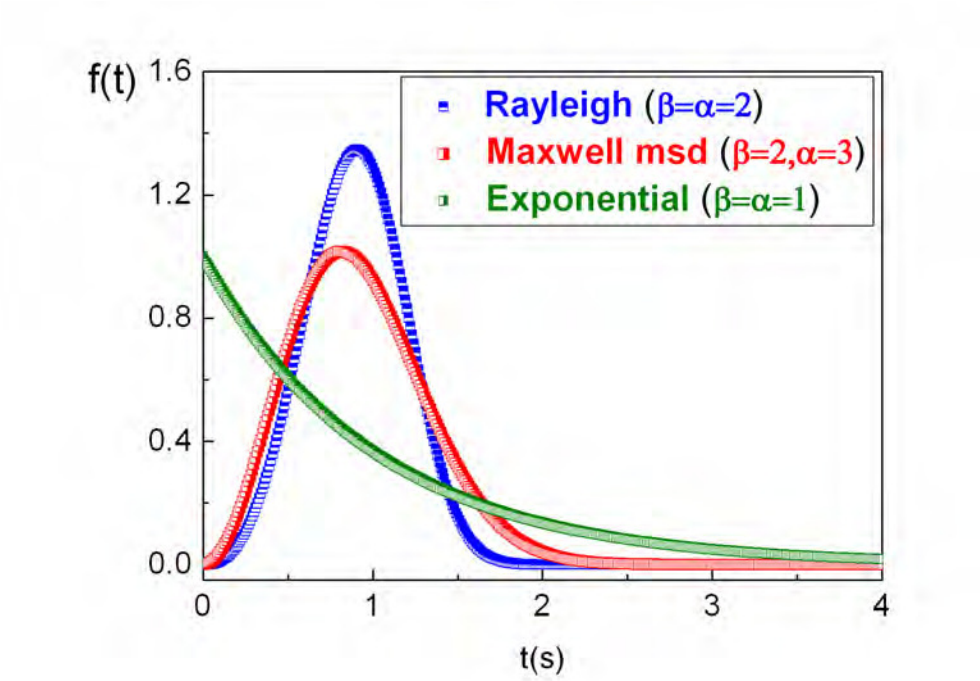

Figure 2.9: *Typical representative examples of the generalized gamma distribution function. All examples have been obtained for the simple case of K=1*

where $g(\log\tau)$ is the distribution function of relaxation times.

Modelling this function has to be compatible with the experimental dielectric spectra. Taking into account the shape of experimental dielectric profiles which are obtained by spectroscopy techniques, this function will need to fulfill the following conditions

- *Its spectral line shape should be asymmetric.*
- *At high frequencies its spectral line shape should yield a power law with variable exponent.*
- *Its spectral density should not diverge at zero frequency.*

The generalized gamma distribution function fulfill this condition and can be defined as:

$$f(t) = \left[\frac{\beta}{\Gamma(\alpha/\beta)}\left(\frac{\alpha}{\beta K}\right)^{\alpha/\beta}\right] t^{\alpha-1}\exp\left[-\frac{\alpha}{\beta}\frac{t^{\beta}}{K}\right] \tag{2.41}$$

where α, β, and K should be positive so that $f(t) \geq 0$, and Γ is the gamma function.
The history of this family of distributions was reviewed and further properties were discussed in 1962 by Stacy [49]. Subsequent work on statistical problems associated with the distribution has been done by Bain and Weeks [50]. This function has been obtained by applying a statistical method to a physical model. The parameters α, β, and K are associated with the scale of the distribution, the number of ways in which the event can occur and a moment of the distribution, respectively. By varying the parameters, a large number of probabilistic models for the description

of random phenomena can be obtained. Special cases of the generalized distribution include a number of familiar distributions which can be obtained as special cases by making certain choices for their parameters as it is showed in figure (2.9). The following functions show examples of this special case which are extensively used in literature.

- *The Rayleigh distribution:* $\beta = \alpha = 2$

$$f(t) = \frac{2}{K} t \exp\left[-\frac{t^2}{K}\right] \tag{2.42}$$

- *The Maxwell molecular speed distribution:* $\beta = 2,\ \alpha = 3$

$$f(t) = \left[\frac{(54/\pi)^{1/2}}{K^{3/2}} t^2\right] \exp\left[-\frac{3}{2}\frac{t^2}{K}\right] \tag{2.43}$$

- *The exponential distribution:* $\beta = \alpha = 1$

$$f(t) = \frac{1}{K} \exp\left[-\frac{t}{K}\right] \tag{2.44}$$

Rössler et al.[51] have used the generalized distribution function for processing experimental data obtained by dielectric spectroscopy. Using the logarithmic Stilje-transformation, they transform the originally generalized gamma distribution function to one commonly used for calculating the equations (2.39) and (2.40) but with a mathematical parameter $\beta > 1$. Taking into account the generalized gamma distribution function and the previous experimental mathematical conditions, Rajagopal et al.[52] proposed a relaxation distribution function with a β_{rj} parameter that perfectly accounts for the relaxation shape:

$$g_{rj}(\log\tau) = \ln 10 \left(\frac{\beta_{rj}}{2\pi(1-\beta_{rj})}\right)^{1/2} \left(\beta_{rj}\frac{\tau}{\tau_0}\right)^{\beta_{rj}/2(1-\beta_{rf})} \exp\left[-(1-\beta_{rj})\left(\beta_{rj}\frac{\tau}{\tau_0}\right)^{\beta_{rj}/(1-\beta_{rf})}\right] \tag{2.45}$$

where τ_0 is a characteristic relaxation time, in the limiting case $\beta_{KWW} = \beta_{rj} = 0.5$ and $\tau_{KWW} = \tau_0$, equation (2.45) yields exactly a KWW function.
Gomez and Alegria [53] established a detailed comparison between the Rajagopal distribution function and the frequency and temporal distribution function obtained as a consequence of the AAC relationship. They found a relationship between the parameters of the KWW and the Rajagopal function described by a fourth order polynomial which gives an exact correspondence for $\beta_{KWW} = \beta_{rj} = 0.5$. In this way the following equation results:

$$\beta_{KWW} = 0.5 + 1.3237(\beta_{rj} - 0.5) + 0.4648(\beta_{rj} - 0.5)^2 - 1.2436(\beta_{rj} - 0.5)^3 - 2.0129(\beta_{rj} - 0.5)^4 \tag{2.46}$$

$$\frac{\tau_{KWW}}{\tau_0} = 1 + 1.4459(\beta_{rj} - 0.5) - 3.2598(\beta_{rj} - 0.5)^2 + 2.385(\beta_{rj} - 0.5)^3 - 2.1424(\beta_{rj} - 0.5)^4 \tag{2.47}$$

From the comparison of different functions with experimental data, they concluded that for polymeric materials the AAC function is the most adequate for describing the frequency dependence. However, in the case of non-polymeric materials the Rajagopal distribution function is a better choice that avoids the Fourier transform of the KWW relaxation function.

2.4 Secondary relaxation processes

2.4.1 β- relaxation process

Usually, supercooled liquids show more than one relaxation process near to the glass transition temperature T_g. In many glass forming materials, besides the α-peak, further relaxation processes lead to additional peaks in $\varepsilon^{''}(\omega)$, which are called β-relaxation (or γ, δ...relaxations if there are more than one).

The slowest relaxation process is called the alpha (α) process, which corresponds to molecular overall tumbling. Secondary relaxation processes occur on shorter time scales usually located in the high-frequency region as showed in figure (2.10). In some glass-formers, additional loss peaks in the dielectric response show up due to the intramolecular degrees of freedom which can modify the dipole moment of the molecule [54-56]. Such secondary relaxations are ascribed to internal changes of molecular conformations. The secondary β-relaxation may appear as a clear peak in the $\varepsilon^{''}(\omega)$ or as a shoulder in the high-frequency part of slower $\alpha-$relaxation. For decades, this process was called simply the β relaxation; "slow" has recently been added to distinguish it from much faster processes β_f which correspond to a complex collective anharmonic cage rattling process, predicted by model coupling theory (MCT).

One of the most typical processes appearing at frequencies above the structural α-relaxation is the commonly referred to as Johari-Goldstein (JG) β-relaxation [57-62]. The microscopic process behind this kind of β (JG) relaxation is still controversially discussed. This process has been shown to occur even in single rigid molecules generally ascribed to the motion of small angle restricted reorientations of all entities and according to the coupling mode theory (CM), is considered as the primitive relaxation [63,64]. The JG β -relaxation can appear as a wing on the high-frequency side of the main α-relaxation, the so-called "excess wing" or simply as a pronounced and well

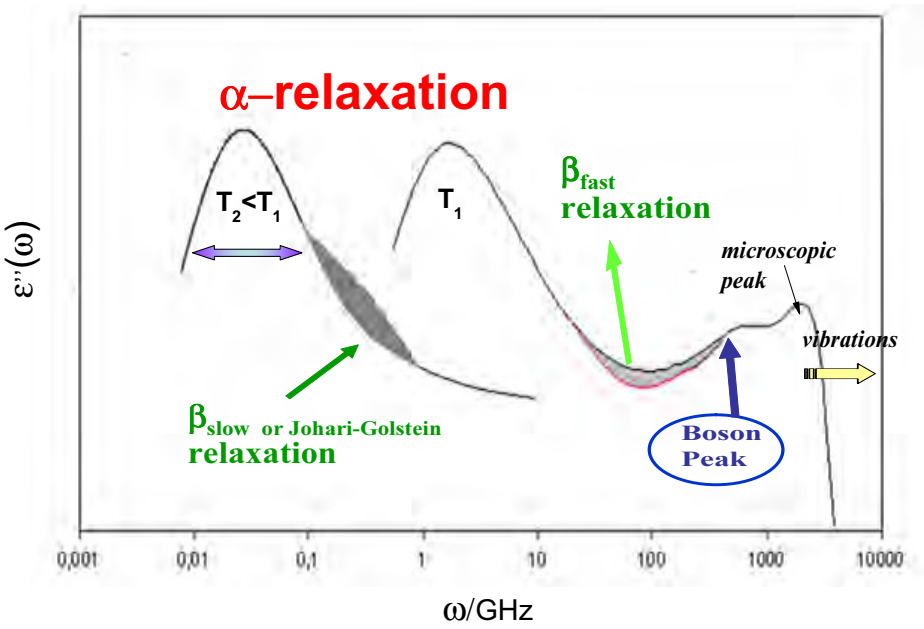

Figure 2.10: *Schematic figure of a Broadband dielectric spectroscopy of frequency range. The slowest relaxation process is called the α- process, and the secondary relaxation processes, occur on shorter time scales usually located in the kHz-MHz. Due to vibrational and excitations of the molecules, small microscopic peaks can appear in the infrared region.*

separated second relaxation [65,66]. Such a difference gives rise to a controversial classification of glass-forming materials [60-67]. Usually, the existence of two types of slow β relaxation are assumed: The first type is believed to be due to internal change of molecular conformations as a result of partial reorientation of molecules, and the second one is the so-called Johari-Goldstein β relaxation (JG).

In the high-frequency domain some additional peaks can appear, as the fast relaxation process predicted by MCT, as is showed at the figure (2.10). On the other hand, at some THz, another peak called the boson peak shows up, and many experimental works by neutron and light scattering experimental techniques [68,69] have been published, being at the present one of the unsolved problems of the condensed matter physics. Finally in the infrared region, small microscopic peaks appear as a consequence of vibrational and rotational excitations of the molecules.

In this work we will study the dynamics of materials in the frequency domain between $10^{-2} \leq \nu \leq 10^{9}$ focusing in to the α and secondary relaxations.

2.4.2 Properties of the β-relaxation process

Several properties have been attributed to the slow β relaxation process which seem to be universal features of these localized and subtle molecular motions. The most prominent one is the Arrhenius dependence of the characteristic relaxation time $\tau(T)$. The Arrhenius equation is usually given in

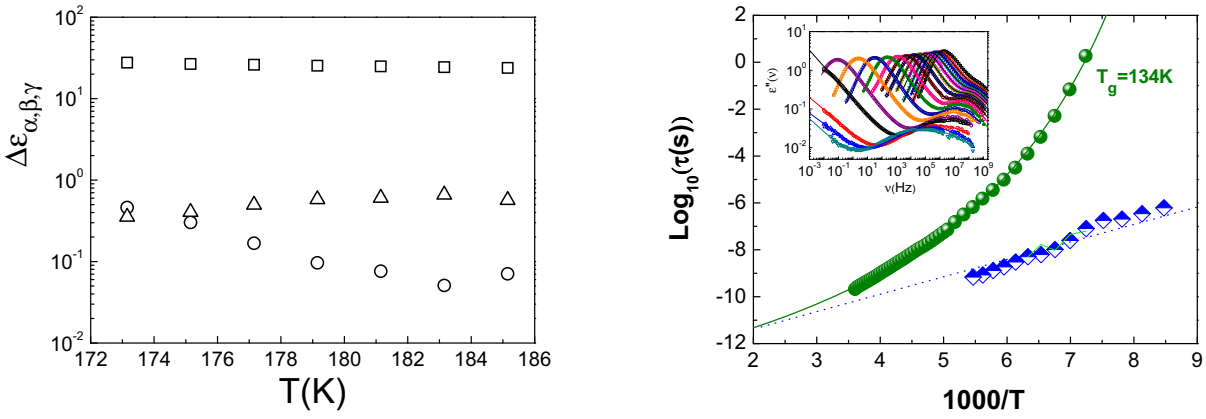

Figure 2.11: *The dielectric strengths (in log scale) for the α-(squares), β-(circles) and -γ (triangles) relaxation processes as a function of temperature for the low-temperature domain of the $(C7-ol)_{0.14}(C8-ol)_{0.86}$ OD mixed crystal is shown on the left graph. The right figure gives the Arrhenius plot for cyanoclyclohexane $(CNC6)$ OD crystal, which shows the temperature relaxation time evolutions of the $\alpha$and β relaxation processes.*

the form

$$\tau_\beta(T) = \tau_0 \exp[\frac{E_\beta}{K_B T}] \tag{2.48}$$

where τ_0 is a temperature independent factor, and E_β, the activation energy, which does not depend on temperature either.

The Arrhenius equation describes the temperature dependence of the relaxation times of a process for which a temperature-independent potential barrier has to be crossed. Typical values are in the range 20 to 50 kJ/mol. Linearization of this equation shows that an Arrhenius process shows up as a straight line when the logarithm of the relaxation time is plotted versus the inverse temperature, where the slope of the linearization analysis gives the activation energy as is showed in figure (2.11). Therefore the relaxation time data in this work will mainly be presented in such a so-called Arrhenius plot.

The following properties are also known for this process:

1. *Symmetric peaks*: The slow β relaxation is assigned to local motion processes, displaying in general a symmetric relaxation time distribution function $g(\tau_\beta)$.

2. *Wide peaks*: The loss peaks are very broad with half widths of $(4-6)$decades.

3. *Small strength*: The definition of the dielectric strength are related with the area below the dielectric loss curve and as an experimental consequence leading that $\triangle\varepsilon_\beta << \triangle\varepsilon_\alpha$. The figure (2.11) shows representative examples of the temperature evolution of the dielectric strength for $(c7-ol)_{0.14}(c8-ol)_{0.86}$ OD mixed crystal which has three relaxation process. It shows that $\triangle\varepsilon_\beta << \triangle\varepsilon_\alpha$ and $\triangle\varepsilon_\gamma << \triangle\varepsilon_\alpha$. Nevertheless for some compounds the strength of both α and β processes are inversed.

4. Extrapolations of the Arrhenius curves $\tau_\beta(T)$ to high temperature related with the β relaxation process tend to intercept the trace of the α relaxation process at a temperature T_β, at which the structural relaxation times seems in many cases to attain values near to $\tau_\beta(T_\beta) = 10^{-7}s$.

2.4.3 Coupling model equation(CM)

Theoretical and experimental studies, such as Quasielastic neutron scattering measurements in poly(vinylchloride), poly(isoprene), and polybutadiene [70] and simple Hamiltonian models that exhibit chaos [71], as well as analysis of molecular dynamics data [72], have shown the existence of a dynamic crossover transition at a time $\tau_c = 2ps$. For longer time than τ_c many body dynamics becomes to take place and a time-dependent relaxation rate probability distribution function $W(t)$ will describe this cooperative motions (explained as a consequence of an environment that provides a time dependent entropy contribution to the free energy which controls the transitions) and will decrease with the time [73-76].

A possible answer to the interconnection of the dynamic physical properties from short and long time, can be explained by the concept of the coupling model (CM) equation, put forward by Ngai [77-79]. At times shorter than τ_c, the basic molecular units relax independently of each other(non-cooperative Debye regimen) and the normalized correlation function follows a simple Kohlrausch exponential dependence $\phi(t) = \exp\left[-\frac{t}{\tau_0}\right]$. The characteristic time of the dynamics without many-body effects is τ_0 and it is called as the primitive relaxation time which for this case is also defined as τ_{KWW}=τ_0. At times longer than τ_c, the molecular interactions increase, yielding a cooperative regimen. In these cases, Ngai et al considered the averaged correlation function as a Kohlrausch stretched exponential $\phi(t) = \exp\left[-(\frac{t}{\tau_\alpha})^{1-n(T)}\right]$ where (τ_α) defines the primary relaxation time and $n(T) = 1 - \beta_{KWW}(T)$ is called as the coupling parameter which represents a measure of the degree of non-exponentially, being a positive fraction of unit and temperature dependent.

Ngai et al introduced a relationship between the primitive and the cooperative primary relaxation time. They considered three aspects:

1. *Dynamic crossover*: Dynamic crossover at a time $\tau_c = 2ps$.

2. *Continuity*: The time-dependent relaxation rate probability distribution function $W(t)$ has to be continuous at τ_c: $\lim_{t\to\tau_c^+} W(t) = \lim_{t\to\tau_c^-} W(t)$ and to fulfill the following probability dynamic transition equation $\frac{\partial\phi(t)}{\partial t} = -W(t)\,\phi(t)$

3. *Relaxation time approximation*: They assumed that τ_{KWW}=τ_α

Taking into account the above considerations, they found as a function of the temperature a power law relationship of the coupling parameter $n = 1 - \beta_{KWW}(T_g)$, which connects the cooperative motion with the secondary β- process. It is known as the CM equation defined by :

$$\tau_0 = (\tau_\alpha)^{1-n} \tau_c^n \tag{2.49}$$

Thus, according to the CM, for a given value of τ_α, the separation of the inherent JG peak (τ_0) should be larger for greater values on the coupling parameter n, i.e., for smaller values of $\beta_{KWW}(T_g)$.

At shorter times than τ_c, the primitive independent relaxation time τ_0 has Arrhenius temperature dependence and experimental evidence proves that a good approximation matches with the most probable JG β-relaxation time being $\tau_0 = \tau_{JG} = \tau_\beta$. At temperatures below T_g, a possible JG process will fulfill the following relationship [80]:

$$\tau_{JG}(T) = \tau_\infty \exp\left[\frac{E_\beta(T)}{RT}\right] \tag{2.50}$$

where $E_\beta(T)$ can change with the temperature but it is constant in the glassy state.

Using the CM equation and following the convention where T_g is conveniently defined as the temperature at which the dielectric relaxation time τ_α reaches $10^2 s$, the normalized activation energy and the β-relaxation time at T_g can be written as:

$$\frac{E_\beta(T_g)}{RT_g} = 2.303\,[2 - 13.7n - \log\tau_\infty] \tag{2.51}$$

$$\log[\tau_0(T_g)] = (1-n)\log[\tau_\alpha(T_g)] + n\log\tau_c \tag{2.52}$$

These equations involve two members that are related with the parameters characterizing the α and β processes. The right members of the above equations can be calculated by two empirical relationships, which involves the α-relaxation broadening parameter n, the infinity relation time τ_∞ and the crossover time τ_c. The left member of these equations can be calculated directly from the experiment, which defines the activation energy of the β process rescaled at T_g and the β-relaxation time at T_g. From the experimental point of view, the above equations will be useful for testing the existence of a possible JG β-relaxation. These correlations give us a useful experimental criterion to distinguish motions of essentially all parts of molecules (i.e. intermolecular JG relaxation).

2.4.4 Corrective functions $C(n)$ and $\triangle E(n)$.

The CM equation comes from three conditions as previously presented. First the dynamic crossover at a critical time τ_c, second, the continuity at this time τ_c and the last one the assumption that the characteristic relaxation time τ_{KWW} is always the α-relaxation time τ_α. The first two considerations are clear, there are strong experimental and theoretical evidences of the existence of this dynamic crossover at τ_c and the continuity can be resolved by the introduction of a relaxation rate $W(t)$ defined as a fractional power law. However in frequency domain is usually chosen for τ_α the

relaxation time τ_{max} which is defined as the inverse of the frequency where $\varepsilon^{''}(\omega)$ has its maximum, or the Havriliak-Negami relaxation relaxation time τ_{HN}. The best time to be considered as τ_α is not very clear. Can both relaxation times be considered as the structural α-relaxation time for testing a possible JG β-relaxation with the CM equation?

The α-relaxation time τ_α is approximately related with the HN relaxation time τ_{HN}, which is also connected with the HN shape parameters and the KWW relaxation time τ_{KWW}. For times longer than τ_c, the dynamic of the system will be cooperative and the coupling parameter will take values ranging $0 < n < 1$ yielding a transition (NonDebye-Debye). In that case, the normalized correlation function can not be written with the cooperative α-relaxation time τ_α represented by τ_{max} or τ_{HN}, and thus considering $\tau_{KWW} = \tau_\alpha$ or $\tau_{KWW} = \tau_{max}$ will contradict the dynamic crossover predicted for the experimental evidences. How is it possible that CM equation still works for a lot of glass formers? The purpose of this section is to find answer to this question.

As we discussed in the last section, Alvarez et al. [43] interrelated the Havriliak-Negami (HN) and the Kohlrausch-Willliams-Watts (KWW) functions, establishing a numerical connection between the relaxation times as a numerical function of the stretching parameter $\beta_{KWW}(T)$, yielding a coupling dependence behaviour $f(n)$ written as:

$$\ln\left(\frac{\tau_{HN}}{\tau_{KWW}}\right) = f(n) \backsimeq 2.6\sqrt{n}\exp\left[-3\,(1-n)\right] \tag{2.53}$$

On the other hand, AAC relationship allows us also the interconnection between the shapes parameters as:

$$n = 1 - (\alpha\beta)^{\frac{1}{1.23}} \tag{2.54}$$

$$\beta = 1 - 0.812(1-\alpha)^{0.387} \tag{2.55}$$

The substitution of the equation (2.55) in (2.54) yields us

$$n = 1 - (\alpha(1 - 0.812(1-\alpha)^{0.387}))^{\frac{1}{1.23}} \tag{2.56}$$

For a set of values of the coupling parameter, the numerical solution of the equation (2.56) gives us numerical functions of $\alpha(n)$ and $\beta(n)$. Changing the coupling parameter for a set of values $0 \leq n \leq 1$, the numerical solution of (2.56) for the cases of $n < 0.2$ gives numerical complex solutions, which is in perfect agreement with the validity of AAC relationship [43].

The numerical solution of the equations (2.55) and (2.56) will give real values for a coupling region ranging $0.2 < n < 0.8$ as is showed at the figure (2.12b). On the other hand, by searching experimental results reported in the literature for different materials such as amorphous polymers (PA), small molecules (SM), plastic crystals (PC) and inorganic materials (IM) there are no reported values of n smaller than 0.2 and higher than 0.8. The majority of glass formers has n lying within

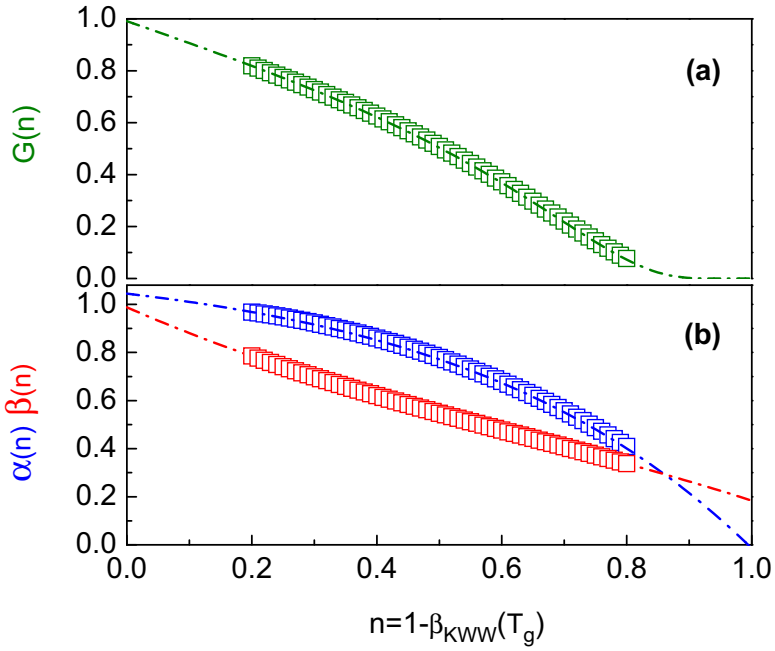

Figure 2.12: *Numerical coupling parameter dependence of the HN shape parameters (bottom panel (b)) and G(n) function (top panel- (a)) calculated within the HN validity domain.*

the approximate range of $0.40 \leq n \leq 0.65$ [80], which is in perfect agreement with the validity of AAC relationship. Thus we can use the above relationship for testing the CM equation.

For times longer than τ_c the α-relaxation peaks are broader with respect to the Debye peaks. The relaxation times which correspond to the maximum of the loss peak are different and can be calculated as the product of a multiplicative function $G(n)$ and the HN relaxation time τ_{HN} as follows [8,9]:

$$\tau_\alpha = \tau_{HN}\left[\frac{\sin\left[\frac{\pi\alpha(n)\beta(n)}{2(\beta(n)+1)}\right]}{\sin\left[\frac{\pi\alpha(n)}{2(\beta(n)+1)}\right]}\right]^{\frac{1}{\alpha(n)}} = \tau_{HN}G(n) \tag{2.57}$$

For the limiting case of a Debye process ($n \to 0$), the multiplicative function $G(n)$ will tend to unity and, it will decrease by increasing the cooperative molecular motions as is showed in the figure (2.12a). It will provide us one way for connecting the AAC relationship with the CM equation.
If we substitute the equation (2.57) in (2.53) the following relationship is obtained

$$\tau_{KWW} = \tau_\alpha \frac{exp\left[-f(n)\right]}{G(n)} \tag{2.58}$$

For times shorter than τ_c, the dynamics of the system will be non-cooperative like a Debye case ($n = 0$), and the numerical function will fulfill the following condition: $\lim_{n\to 0} f(n) = 0$ and $\lim_{n\to 0} G(n) = 1 \Rightarrow \tau_{KWW} = \tau_a = \tau_0$. For times longer than τ_c, the coupling parameter will take values $0 < n < 1$ and both functions $f(n)$ and $G(n)$ will have a strong dependence with n. In that case $\tau_{KWW} \neq \tau_\alpha$, and the normalized correlation function can not be written with the cooperative α-relaxation time τ_α.

In order to compare the quantitative difference between both relaxation times, we calculated the relative discrepancy for a set of coupling values ranging with in the experimental typical values. The relative discrepancy can be defined as:

$$\delta\tau(n) = \left|\frac{\tau_{KWW} - \tau_\alpha}{\tau_\alpha}\right| \cdot 100 = \left|\frac{\exp[-f(n)]}{G(n)} - 1\right| \cdot 100 \tag{2.59}$$

For the Debye case there is no discrepancy between both relaxation times, and the above function will tend to zero. For the cases of cooperative motions, both relaxation times will become more different leading to a dramatically increase of the discrepancy, taking values higher than 100%, as showed in figure (2.13a). How is it possible that both relaxation times are so different and the CM equation remains valid for a large number of glass formers?
The CM equation can be rewritten with the true relaxation time which will appear as a result of the KWW function. Taking into account this result we can rewrite the CM equation as follows

$$\tau_0^C = (\tau_{KWW})^{1-n}\,\tau_c^n \tag{2.60}$$

where we call the corrective primitive relaxation time as τ_0^C. Inserting the equation (10) in (12) we obtain:

$$\tau_0^C = (\tau_\alpha)^{1-n}\,\tau_c^n\left(\exp[f(n)(n-1)]\,G(n)^{n-1}\right) = \tau_0 C(n) \tag{2.61}$$

The corrective CM equation can be defined as the product of two terms. The first one will be the original primitive relaxation time τ_0, introduced by Ngai and the second new term will be a function which will only depends on the coupling parameter n, being insensible to the relaxation crossover time τ_c. We call this new term as the corrective relaxation time function $C(n)$ and for the limiting cases it will take the following values:

$$C(n) = \exp[f(n)(n-1)]\,G(n)^{n-1} = \begin{cases} 1 & n = 0 \\ 1.15 & n = 0.65 \end{cases} \tag{2.62}$$

In the Debye limiting case $(n = 0)$, the corrective function will tend to unity, recovering the original primitive relaxation time from Ngai. But in the coupling domain, the corrective function will take values ranged between $1.07 < C(n) < 1.30$ as showed in figure (2.13b). On the other hand, for the experimental cases $0.40 \leq n \leq 0.65$, the corrective function takes values $C(n) < 1.15$. The CM equation has been defined as a power law function with exponent smaller than unity. This is the key point that gives validity also when it is used with different relaxation times.This conclusion can be summarized in the following mathematical relationship

$$\forall_{0\leq n<1} \Rightarrow (\tau_{HN} \neq \tau_{KWW} \neq \tau_\alpha) \Rightarrow ((\tau_{HN})^{1-n} \approx (\tau_{KWW})^{1-n} \approx (\tau_\alpha)^{1-n}) \tag{2.63}$$

Taking into account this finding, we can rewrite the normalized corrective activation energy.

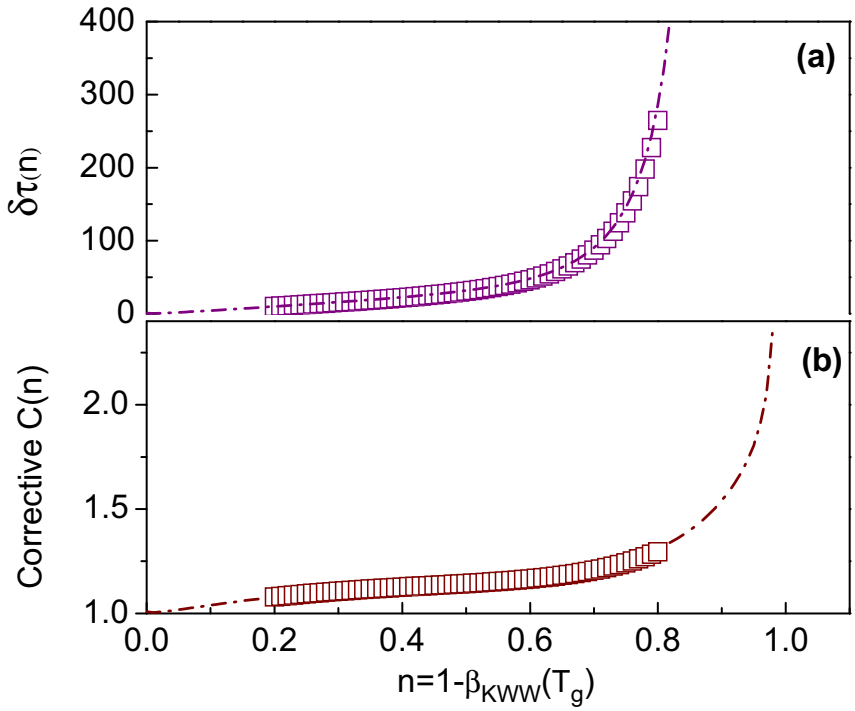

Figure 2.13: *Numerical coupling parameter dependence of the relaxation time corrective function $C(n)$ (bottom panel (b)) and the relative discrepancy $\delta\tau(n)$ (top panel- (a)) calculated within HN validity domain.*

In this case the new term appears additively, which is a direct consequence of the definition of corrective functions $C(n)$ and the equation (2.51) will be modified as follows

$$\frac{E_\beta^C}{RT_g} = 2.303\,[2 - 13.7n - \log\tau_\infty] + 2.303\log C(n) \tag{2.64}$$

The normalized corrective activation energy can be then written as the sum of two contributions. The first one is the equation (3) and the second one comes from the definition of the corrective function, which we call the corrective energy function $\Delta E(n)$.

$$\triangle E(n) = \left(\frac{E_\beta^C}{RT_g} - \frac{E_\beta}{RT_g}\right) = 2.303\log C(n) = \begin{cases} 0 & n = 0 \\ 0.17 & n = 0.65 \end{cases} \tag{2.65}$$

For the Debye limiting case $(n = 0)$ the corrective energy function will tend to zero, recovering the original equation (2.51). But in the coupling domain, the corrective energy function will take values $0 < C(n) < 0.22$ as showed in figure (2.14). On the other hand, for the experimental real cases $0.40 \leq n \leq 0.65$ the corrective function takes values $\triangle E(n) < 0.17$.
These values are close to zero, and do not have physical influence. These values will correspond to an ideal and unfeasible relaxation process. On the other hand, for a genuine JG β-relaxation process, Kudlik et at. [81,82] proposed an empirical relation of the normalized activation energy which can be written by the following experimental ratio:

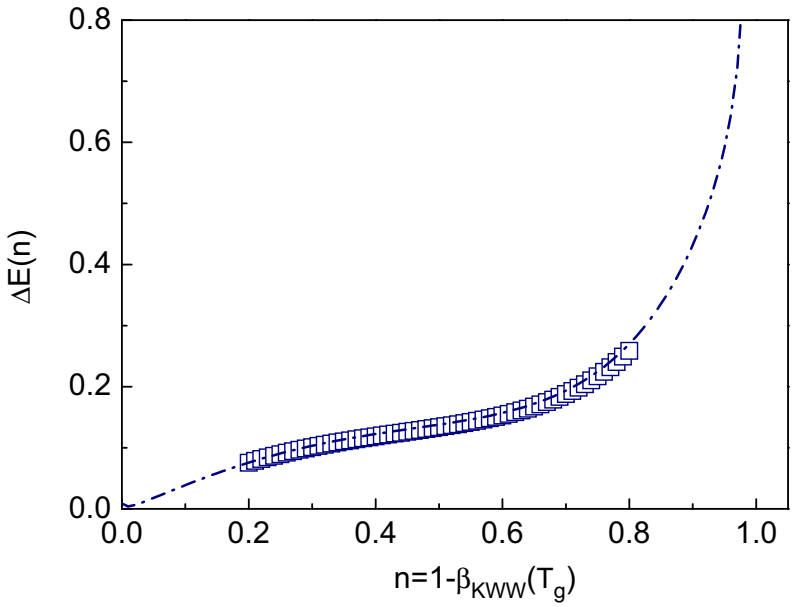

Figure 2.14: *Numerical coupling parameter dependence of the energy corrective function* $\Delta E(n)$ *calculated within HN validity domain*

$$E_{Kudlik} = \frac{E_\beta}{RT_g} \approx 24 \tag{2.66}$$

If we compare, in the experimental coupling domain, the ratio of the genuine JG process with the maximum value of the corrective energy function, a negligible corrective energy contribution is found. For all experimentally reported coupling domains $0 \leq n \leq 1$, independently of the relaxation time that has been chosen for the experiment (τ_{HN}, τ_{max} or τ_{KWW}), the corrective functions $C(n)$ and $\triangle E(n)$ will take values around the unity and zero respectively, and the CM equation will remain unchanged to testify the JG processes.

Bibliography

[1] M. Faraday, Phil. Trans **128**, 79, (1837).

[2] J. C. Maxwell, Phil. Trans**155**, 459, (1865) Ibid, **158**, 643,(1868): *Treatise on Electricity and Magnetism*; Dover: New York, (1954).

[3] R. Clausius, Die Mechanische Wärmetheorie, **vol II**; Braunschweig, (1879): F. P. Mossotti, Bibl. Univ. Modena **6**, 193, (1847).

[4] L. Lorentz, Ann. Phys. Chem **11**, 70 ,(1880), H. A. Lorentz, Verh. Kon. Acad. Van Wetenschappen; Amsterdam, (1879), Ann. Phys **9**, 641, (1880) *Theory of Electrons*, Dover: New York, (1952).

[5] J. C. Maxwell, *Electricity and magnetism*, **vol. 1** Clarendon: Oxford, (1892).

[6] P. Debye, *Polar Molecules*; Dover: New York, (1929).

[7] H. Fröhlich, *Theory of Dielectrics*; Clarendon Press: Oxford, (1958).

[8] C. F. J. Böttcher, O. C. Belle, P. Bordewijk, Rip, A.; *Theory of Electric Polarisation*; **Vol I (2nd edition)**, Elsevier: Amsterdam, (1973).

[9] C. F. J. Böttcher, P. Bordewijk, *Theory of Electric Polarisation*, **Vol II (2nd edition)**, Elsevier: Amsterdam, (1978).

[10] F. Kremer, A. Schönals, *Broadband Dielectric Spectroscopy*, Springer: Berlin, (2003).

[11] L. Onsager, J .Am. Chem Soc **58**, 1486, (1938).

[12] J. G. Kirkwood, J Chem. Phys **58**, 911, (1939).

[13] J. G. Kirkwood, Ann NY. Acad. Sci **40**, 911, (1940).

[14] J. G. Kirkwood, Trans. Faraday. Soc **42A**, 7, (1939).

[15] C. Kittel, *Elementary Statistical Physics*; Wiley: New York, (1971).

[16] J. G. Kirkwood, J. Chem. Phys **4**, 592 (1936), Ibid, **58**, 1486, (1936).

[17] J. Ll. Tamarit, M. A. Perez-Jubindo, M. R. de la Fuente, J. Phys.Condes. Matter **9**, 5469, (1997).

[18] W. Huang, R. Richert, J. Chem. Phys **124**, 164510, (2006).

[19] G. Katana, E. W. Fischer,Th.Hack, V. Abetz , F. Kremer, Macromolecules **28**, 2714, (1995).

[20] A. C. Kumbharkhane, S. M. Puranik, S. C. Mehrotra, J. Mol. Liq **51**, 261, (1992).

[21] A. C. Kumbharkhane, S. M. Puranik, S. C. Mehrotra, J. Sol. Chem **22,** 219, (1993).

[22] G. Parthipan, T. Thenappan, J. Solution. Chem **36**, 1231, (2007).

[23] J. C. Martinez-Garcia, J. Ll. Tamarit, S. Capaccioli, M. Barrio, N. Veglio, L. C. Pardo, J. Chem. Phys **132**, 164516 (2010).

[24] A. Rivera, E. A. Rössler, Phys. Rev. B **73**, 212201, (2006).

[25] J. C. Martinez et al, Phys.Status. Solid A, (in press).

[26] K. W. Wagner, Arch. Electrotech **2**, 317, (1914).

[27] L. D. Landau, E. M. Lifschitz, *Textbook of theoretical physics*, **Vol.V.Statistical physics**. Akademie-Verlag:Berlin.(1979).

[28] C. T. Moynihan, L. P. Boesch, N. L. Laberge, Phys. Chem. Glasses **14**, 122, (1973).

[29] G. Williams, D. C. Watts, S. B. Dev, A. M. North, Trans. Faraday Soc **67**, 1323, (1977).

[30] R. P. Brent, A.C. M Trans. Math. Sotfware **4**, 57, (1978).

[31] J. L. Blue (Bell Laboratories, private communication).

[32] K. S. Cole, R. H. Cole, J. Chem. Phys **9**, 341, (1949).

[33] R. M. Fuoss, J. G. Kirkwood, J. Am. Chem. Soc **63,** (1941).

[34] D. W. Davidson, R. H. Cole, J. Chem. Phys **18**, 1417, (1951).

[35] A. K. Jonscher, Colloid Polymer. Sci **253**, 231, (1975).

[36] S. Havriliak, S. Negami, Polymer **8**, 101, (1967).

[37] R. Kohlrausch, Ann. Phys **12**, 393, (1847).

[38] G. Williams, D. C. Watts,Trans. Faraday. Soc **66**, 80 (1970), G. Williams, M. Cook, P. J. Hains, J. Chem.Soc. Faraday Transactions II, **2**, 1045, (1972).

[39] R. Böhmer, K. L. Ngai, C. A. Angell, D. J. Plazek. J. Chem. Phys **99**, 4201, (1993).

[40] J. C. Martinez-Garcia, et al: Mathematic procedure routine(in preparation).

[41] N. Miura, N. Shinyashiki, S. Mashimo, J. Chem. Phys, **97**, 8722, (1992), R. W. Rendell, K. L. Ngai, S. Mashimo, J. Chem. Phys **87**, 2359, (1987).

[42] C. P. Lindsey, G. D. Patterson, J. Chem. Phys **73**, 3348, (1980).

[43] F. Alvarez, A. Alegria, J.Colmenero, Phys. Rev. B **44**, 7306, (1991).

[44] S. W. Provencher, Comput.Phys.Commun.**27**, 213, (1982).

[45] Y. Imanischi, K. Adachi, T. Kotaka, J. Chem. Phys **89**, 7593, (1988).

[46] A. Alegria, J. Colmenero, P. O. Mari, I. A. Campbell, Phys. Rev. E **59**, 6888, (1998).

[47] T. J. Stieltjes, *Recherches sur les fractions continues*. Ann. d. fac. d. sciences Toulouse **8, No. 4**, J1-J122, (1894).

[48] H. Kestelman, *Riemann-Stieltjes Integration*. Ch. 11 in Modern Theories of Integration, 2nd rev. ed. New York: Dover, pp. 247-269, (1960).

[49] E. W. Stacy, *A generalization of the gamma distribution*, Ann. Math. Statist **33**, 1187, (1962).

[50] L. J. Bain, D. L. Weeks, *Tolerance limits for the generalized gamma distribution*. J. Amer. Statist. Assoc **60**, 1142, (1965).

[51] C. Tschirwitz, S. Benkhof, T. Blochowicz, E. Rössler, J. Chem. Phys **117**, 6281, (2002).

[52] A. K. Rajagopal, K. L. Ngai, in: K. L. Ngai, G. B. Wrigth, (Eds.), Relaxations in Complex Systems, North-Holland: Amsterdand, (1991).

[53] D. Gomez, A. Alegria, J. Non-Crystalline Solids **287**, 246, (2001).

[54] K. L. Ngai, M. Paluch, J. Chem. Phys **120**, 857, (2004).

[55] R. Brand, P. Lunkenheimer, A. Loidl, J. Chem. Phys **116**, 10386, (2002).

[56] K. Pathmanathan, G. P. Johari, J. Phys. C **18,** 6535, (1985).

[57] G. P. Johari, M. Goldstein, J. Chem. Phys **53**, 2372, (1970).

[58] K. L. Ngai, Comments. Solid .State Phys **9**, 127, (1979).

[59] K. L. Ngai, *Disorder Effects on Relaxational Properties*, edited by R. Richert and A. Blumen, Springer: Berlin, p. 89, (1984).

[60] K. L. Ngai, J. Phys. Condens. Matter **15**, S1107, (2003).

[61] S. Capaccioli, K. L. Ngai, J. Phys. Chem. B **109**, 9727, (2005).

[62] P. Lunkenheimer, L. C. Pardo, M. Köhler, A. Loidl, Phys. Rev. E **77**, 031506, (2008).

[63] K. L. Ngai, Phys. Rev. E **57**, 7346, (1998).

[64] K. L. Ngai, J. Phys. Condens. Matter **15**, 1107, (2003).

[65] U. Schneider, R. Brand, P. Lunkenheimer, A. Loidl, Phys. Rev. Lett. **84**, 5560, (2000).

[66] K. L. Ngai, P. Lunkenheimer, C. León, U. Schneider, R. Brand, A. Loidl, J. Chem. Phys **115**, 1405, (2001).

[67] A. Kudlik, S. Benkhof, T. Blochowicz, C. Tschirwitz, E. Rössler, J. Mol. Struct **479**, 201, (1999).

[68] W. Götze, J. Phys. Condens. Matter **10A**, 1-45, (1999).

[69] E. Rössler, V. N. Novikov, A. P. Sokolov, Phase Transitions **63**, 201, (1997).

[70] J. Colmenero, A. Arbe, A. Alegria, Phys. Rev.Lett **71**, 2603, (1993).

[71] R. Zorn, A. Arbe, J. Colmenero, B. Frick, D. Richter, U. Buchenau, Phys. Rev. E 52, 781, (1995).

[72] C. M. Roland, K. L. Ngai, L. Lewis, J.Chem.Phys **103**, 4632, (1995).

[73] R.-J. Roe, J. Chem. Phys **100**, 1610, (1994), K. L. Ngai, *ibid.***98**, 7588, (1993).

[74] K. L. Ngai, J. Chem. Phys **98**, 7588, (1993).

[75] K. L. Ngai, C. M. Roland, G. N. Greaves, J. Non-Cryst. Solids **182**, 172, (1995).

[76] A. K . Rajagopal, J. Phys. C: Solid State Phys **17**, 6611, (1984).

[77] K. L. Ngai, Comments Solid State Phys **9**, 141, (1979).

[78] K. L. Ngai, K. Y. Tsang, Phys.Rev.E **60**, 4511, (1999).

[79] K. L. Ngai, IEEE Trans.Dielectr.Electr.Insul **8**, 329, (2001).

[80] K. L. Ngai and S. Capaccioli, Phys.Rev.E **69**, 031501, (2004).

[81] A. Kudlik, C. Tschirwitz, S. Benkhof, T. Blochowicz, E. Rössler, Europhys. Lett **40**, 649, (1997).

[82] A. Kudlik, C. Tschirwitz, S. Benkhof, T. Blochowicz, E. Rössler, J. Non-Cryst.Solids **406**, 235, (1998).

Chapter 3

Materials and methods

In this chapter we focus on the materials and experimental techniques that have been used in this work. We focus on two questions: What is measured? How are the measurements performed?
The first section is devoted to the studied materials. We describe the polymorphic behavior of the studied materials displaying orientationally disordered phases. We also enclose a brief description of several materials whose experimental data, although they were not measured by us, have been used to analyse the universal behavior of glasss forming liquids. These materials are a low weight molecular liquid, a polymeric liquid and a liquid crystal.
The experimental techniques are detailed in the second part of this chapter. The basic concept of the dielectric spectroscopy technique as well as a brief description of the experimental setup used in this work is shortly introduced. Two additional experimental techniques, X-ray diffraction and calorimetry, which have been used for complementing the study are presented as well.

3.1 Materials

In this work, all studied materials are obtained from Aldrich Chemical company (*ACC*) and Across Organic (*AO*) with a purity of at least 99%. Cyclooctanol and cycloheptanol were submitted to an additional purification process consisting of a vacuum sublimation at a reference temperature, whereas the other compounds were used as purchased. The purity was checked by means of differential scanning calorimetric by measuring the melting temperature and, when possible the solid-solid phase transitions between the plastic phase and the low-temperature ordered phases. Mixed crystals were prepared from the melting of the pure materials in the selected molar composition as well as by simple addition of liquids in the desired proportions when their melting temperature was below room temperature.

Table 3.1: *Pure compounds usedin this study and suppliers (and purity) together with the glass transition temperature (Tg) of the orientational glass (OG). AO: Across Organics, ACC: Aldrich Chemical Company. Lattice symmetry of the OD phase: simple cubic (sc) and face-centered-cubic (fcc). (*)The OD phase I of Cladam cannot be supercooled to obtain the associated OG.*

Name	Symbol	Chemical Formula	OD Phase	Tg/K	Purity
Cycloheptanol	c7-ol	$C_7H_{13}OH$	I(sc)	140	$AO, > 99\%$
Cyclooctanol	c8-ol	$C_8H_{15}OH$	I(sc)	165	$AO, > 99\%$
Cyano-admantane	CNadm	$C_{10}H_{15}-CN$	I(fcc)	169	$ACC, > 99\%$
Chloro-adamantane*	Cladm	$C_{10}H_{15}-Cl$	I(fcc)		$ACC, > 99\%$
Cyano-cyclohexane	CNc6	$C_6H_{11}-CN$	I(fcc)	134	$ACC, > 99\%$

3.1.1 Plastic crystals

On cooling the liquid of a system formed by, in general, elongated molecules, the orientational order appears while the translational order is still missing, giving rise to the well-known mesogenic phases of liquid crystals and the related glass formers on further cooling [1,2]. On the contrary, for globular shaped molecules, the liquid state can transform to a translationally ordered high-symmetry phase (generally cubic or hexagonal) with orientational disorder. Such orientationally disordered (*OD*) or plastic phases can be supercooled preventing the complete orientational ordering and an orientational-glass (*OG*) state exhibiting translational order and static orientational disorder is achieved [3-10].

Such a particular orientational disorder was described by Timmermans in 1961 [11] who showed that crystals composed of molecules whose shape is more or less spherical have small entropy and volume changes of fusion. In plastic crystals the centers of mass of the molecules form a regular crystalline lattice but the molecules are dynamically disordered with respect to their orientational degrees of freedom. Due to the translational long-range order, plastic crystals are much simpler to treat in theoretical and simulation approaches of the glass transition and therefore these materials are often considered as model systems for structural glass formers.

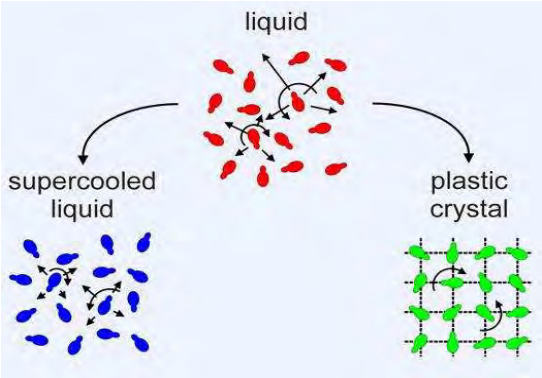

Figure 3.1: *Schematic representation of the possible transitions of a liquid of a dipolar molecules (represented by asymmetric dumbbells) in to a supercooled liquid or a plastic crystal [12].*

Some materials used in this work belong to the group of lower order cyclic alcohols defined as the family $C_nH_{2n-1}OH$ where $n = \{5,6,7,8\}$. These materials are good examples of pseudoglobular molecules displaying *OD* phases [12-14]. A very close related material has been also studied, cyanocyaclohexane, which also displays a globular shaped molecular symmetry.

All these molecules can display a finite number of molecular conformations, giving rise to a rich polymorphism and the polar *OH* or *CN* groups may adopt either of two conformations, the axial and the equatorial with respect to the carbon atom on which the group is bonded, yielding different contributions to the dipole moment orientation, and thus to additional secondary relaxations. On the contrary, adamantane derivatives are also globular shaped molecules giving rise to *OD* phases, but composed from a rigid molecular structure. Within the next sections, a detailed explanation of the polymorphism of the studied materials is given.

3.1.2 Polymorphic behavior of the studied materials

3.1.2.1 Cylooctanol

As far as the polymorphic behavior of Cyclooctanol(C8-ol) is concerned, it exhibits a transition from the liquid state to the simple cubic (sc)*OD* phase I [14-16]. On further slow cooling the *OD* phase transforms to an orientationally ordered state (phase II), in which the α-relaxation corresponding to the dipolar disorder is absent. Such a transition can be bypassed by a relatively fast cooling from the *OD* phase, which enables us to obtain the corresponding *OG* state below T_g (between 142 and 172K) [13,14,16-22]. On heating up above the glass transition, the supercooled *OD* phase remains (metastable) until about 200K, where C8-ol transforms to the orientationally ordered phase II. Details of the polymorphic behavior of C8-ol have been largely discussed [15].
As for the additional β- and γ-relaxation processes in C8-ol, it has been demonstrated that they also show up in the low temperature ordered phase with the same relaxation time for a given temperature, and thus they have been ascribed to the conformations of the ring (β-relaxation) and to those (axial and equatorial, γ-relaxation) adopted by the polar *OH* group with respect to the carbon atom on which the group is bonded [10,14]. It is worth noting that the existence of such a conformational disorder has been claimed as the origin of the difficulty to reach the low-temperature ordered phase for many *OD* phases formed by molecules with intrinsic conformational degrees of freedom.

3.1.2.2 Cycloheptanol

Cycloheptanol (C7-ol) has been far less studied probably because of the existence of two *OD* and two low-temperature ordered phases [8,15,22]. On cooling from the liquid state the simple cubic *OD* phase I appears and can be readily supercooled, giving rise to an *OG*. On the contrary, the tetragonal *OD* (phase II) can be hardly supercooled, although some authors reported a glass transition temperature of the corresponding glass state from an extrapolation of the dielectric data [15,22]. One of the striking differences between cycloheptanol and cyclooctanol concerning the relaxation processes appearing in their simple cubic *OD* phases is that the former shows, in addition to the α-relaxation, only one secondary fast process, which according to the molecular conformational disorder is ascribed to the axial and equatorial orientations of the $-OH$ group and

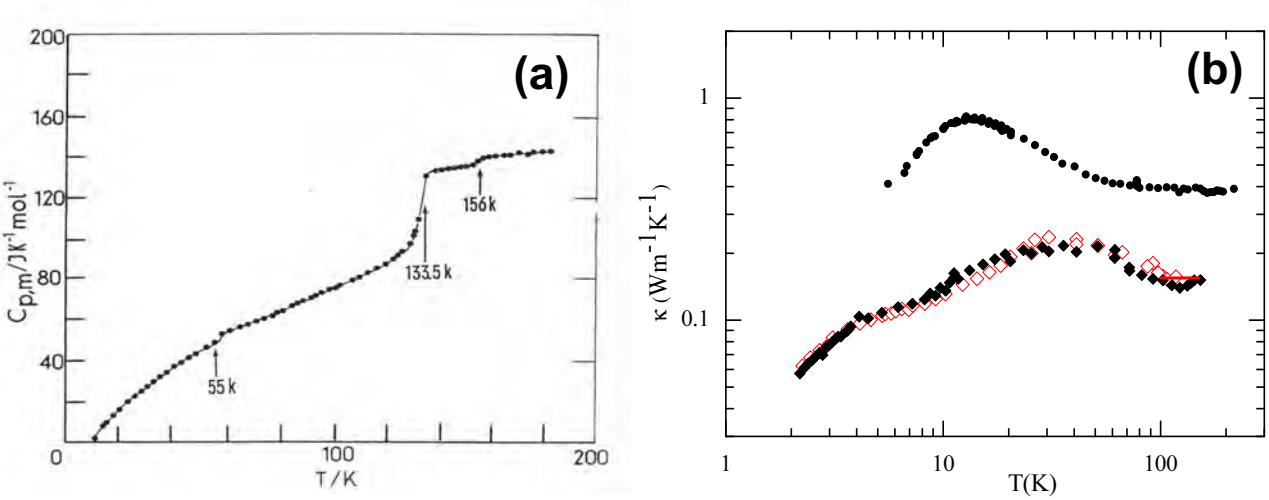

Figure 3.2: *(a) Molar heat capacity of Cyanocyclohexane (unpublished results from PhD of Pinvidic, University of Orsay, Paris. (b) Thermal conductivity of solid (upper curve) and orientational glass (lower curve) of Cyanocyclohexane. Red diamonds correspond to orientational glass of Cyclohexanol (unpublished results)*

by analogy with cyclooctanol is called γ-relaxation [15,17,22]. It should be mentioned that some authors argued the existence of a β-relaxation also for cycloheptanol [23].

3.1.2.3 Cyanocyclohexane

Cyanocyclohexane (CNc6) is a well-known example of materials displaying an *OD* phase which gives easily rise to an *OG*. It turns out to be an ideal candidate because of its stability in temperature. From calorimetric measurements, it has been seen that the crystallization of the liquid takes place at $T_m = 285K$, forming a crystalline phase (phase I) stable up to $T_t = (217 \pm 3)\,K$ [24], being below this temperature still sufficiently stable to be examined on considerably long time scales. Nevertheless, it was shown that applying higher pressure or annealing the sample for long times, another crystalline phase (phase II) may form. It has been suggested that phase II is the orientationally ordered crystal that always exists in parallel to a supercooled plastically crystalline phase [25]. In addition, cyanocyclohexane is not a rigid molecule and conformational disorder also exists [26]. Depending on the orientation of the carbonitrile $(C \equiv N)$ group with respect to the cyclohexane ring, an axial and an equatorial conformation exist. The conversion from one to the other molecular conformation is possible and involves an energy barrier of ca. $\triangle E/K_B = 4500K$ and, according to recent Raman measurements, the chair ring conformation together with axial for *CN* was reported with an abundance of $58 \pm 8\%$ in the liquid state [27].
The molar heat capacity C_p as a function of temperature is represented in figure (3.2a), and beside the prominent glass step that can be seen around $133.5K$ (T_g of the orientational freezing), two additional weak step-like signals appeared at $55K$, i.e., within the orientational glass, and at $156K$,

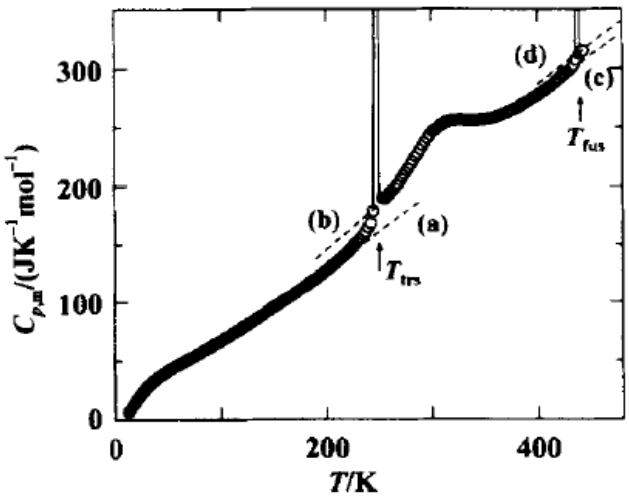

Figure 3.3: *Calorimetric results from [29]. A calorimetric jump is to be seen in the plastic phase at* $310K$

within the supercooled (phase I). The latter has been tentatively ascribed to the freezing of the axial-equatorial conformation conversions, but the origin of the former, which also has been reported for some Freon derivatives [28], is still a matter of debate, although it seems that the freezing of molecular conformations is involved. In fact, the Raman study was performed as a function of temperature, but by dissolving the sample, so all the transitions (even that given rise to the *OD* phase) are missed.

Members of our group have recently measured the thermal conductivity (figure 3.2b) down to very low temperatures (down to $2K$). It depicts the typical behaviour for canonical glasses, although the behaviour is found to be dependent on the thermal history and at present we strongly believe that such behaviour should be linked to the freezing of different molecular conformations.

3.1.2.4 Chloroadamantane

Adamantane derivatives form a large and interesting group of substances displaying *OD* phases. The pseudoglobular molecular shape of these compounds together with the dipolar character of the derivatives inferred by the substitution of one hydrogen in the adamantane molecule provides to this group interesting properties which can be used for fine tuning of the required properties. In particular, several properties are known as relevant to make interesting these compounds [30-32]. On the other hand, overall free tumbling is impossible due to the hindering produced by the strong dipolar character for molecules with C_{3v} symmetry as for $1-X$-adamantane substituted compounds $(X = Cl, Br, CN, ...)$[33,34]. On the second hand, fast rotations around the dipolar C_{3v} axis have been characterized to be faster than those concerning the overall molecular rotation, both being then clearly decoupled [34,35] and, finally, these molecules are rigid and non-hydrogen

bonded, so then secondary relaxations, if present, should be uniquely related to "pure" Johari-Goldstein $\beta-$relaxations [35].

Chloro-Adamantane (Cladm) is a huge molecule, but in spite of its size, it is completely rigid. This makes very easy to study both its dynamics and structure. The *OD* fcc phase ($Fm3m$ space group symmetry) of Cladm ($\mu = 2.39D$)[34,33] ranges from $249K$ until the melting point at ca. $439K$. The specific heat of this substance in the plastic phase is however puzzling: it has a calorimetric hump at about $310K$ [36] that has been associated with a change in the dynamics of the system [37]. At low temperature the molecule performs "free small-step rotational diffusion", and at high temperature the dynamics is described by an "activated jump-like motion". Although molecular dynamics simulations [38] claim for the existence of an *OG* with $T_g < 217K$, as far as we know, no experimental evidence has been published till now.

3.1.2.5 Cyanoadamantane

Cyanoadamante(CNadm) is another example of a rigid molecule with C_{3v} molecular symmetry as those belonging to the $1-X$-adamantane derivatives. As in the previous case of Chloro-adamantane, fast rotations around the dipolar C_{3v} molecular axis have been characterized to be faster than those concerning the overall molecular rotation existing in the plastic phase, both being then clearly decoupled from a dynamical point of view.

The $(C \equiv N)$ radical group confers to CN a strong dipolar moment ($\mu = 3.83D$). The only internal degree of freedom corresponds to the motion of $(C-C \equiv N)$ group, the associated dynamics being far away from the frequency range analysed in this work [39]. This compound has been studied by means of an extended number of experimental techniques as dielectric spectroscopy, *NMR*, thermal analysis, inelastic X-ray scattering, calorimetry, thermally stimulated discharge currents and Raman spectroscopy [39-42]. Some molecular dynamics studies have also been reported [34,43]. As far as its polymorphism is concerned, it has been clearly stated that the melt crystallizes into an *OD* cubic plastic phase with $Fm3m$ symmetry at ca. $462K$ [44]. This phase is dynamically characterized by restricted tumbling in such a way that 6 equilibrium orientations along the $< 001 >$directions can be distinguished, as well as threefold uniaxial rotations around the$(C-C \equiv N)$, i.e., the C_{3v} axis corresponding to the dipolar molecular axis, which means that such disorder is not seen by dielectric spectroscopy [44,45]. At lower temperatures, CNadm transforms to a more ordered crystalline phase, the structure of which is known to be monoclinic (space group $C^2/_m$) with an antiferroelectric order. In fact, the local antiferroelectric order in the *OD* phase is known to be reminiscent of such an order in the low-temperature monoclinic phase [43]. In this low-temperature ordered phase the uniaxial rotations along C_{3v} axis also remain. The *OD* phase can be easily quenched by cooling into a glassy crystal, the non-ergodic state associated with the ergodic *OD* phase, with a glass transition temperature at about $170K$ [46,50]. As far as this glass transition is concerned, Yamamuro et al. [40] argued that in fact orientational degrees of freedom can be frozen in at higher temperatures and, in the recent work from Carpentier et al. [51], this

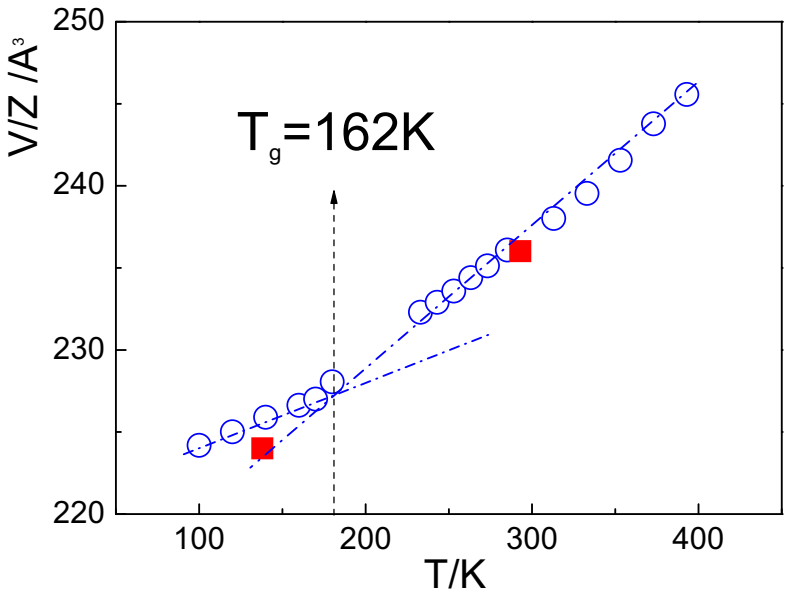

Figure 3.4: *Volume per unit of molecule of the OD fcc phase and the OG for the CNadm on heating after quenched at* 100*K from room temperature and on heating after cooling down until* 233*K. The squares correspond to the values from [46,48]*

transition is much more related with the freezing of the fluctuations of an antiferroelectric local ordering, occurring on a size and time scale larger than those characteristic of the dynamic slowing down (i.e. $\tau(T_g) = 100s$). On further heating after the quenching process or simply ageing at temperatures higher than T_g, the supercooled *OD* fcc phase transforms to the low-temperature ordered phase via an intermediate metastable phase [51,52]. Figure (3.4) depicts the lattice volume per molecule of the *OD* phase and of the non-ergodic state, the orientational glass *OG* state. It clearly evidences the well-known change of the isobaric thermal expansion coefficient at the glass transition. It should be noticed that after the quenching at 100*K* X-ray patterns as a function of the increasing temperature only showed Bragg reflections corresponding to the fcc lattice.

3.1.3 Other materials

In order to analyse the universality of several properties of glass forming materials, we have used three set of dielectric data $\tau(T)$ taken from earlier studies. Its chemical structure is shown in figure (3.2). They are (i) the oligomeric liquid EPON 828, (ii) octyloxycyanobiphenyl (8*OCB) [53], isomer of liquid crystalline 8OCB, which remains in the isotropic phase on supercooling, and (iii) propylene carbonate (PC), a low molecular weigth liquid [54]. The first data was provided from Dr. Silvia Corezzi and the last two datas were provided from Dr. Sylwester Rozka.

EPON 828, oligomeric liquid (polymeric liquids)

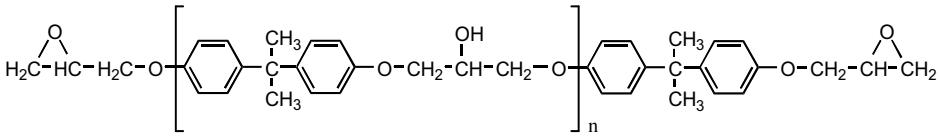

Propylene Carbonate (PC)
a low molecular weight liquid

$C_4H_6O_3$

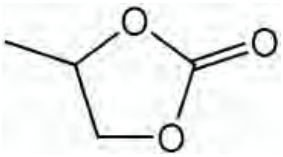

Octyloxy-cyanobiphenyl
isomer of liquid crystalline 8*OCB

C_nH_{2n+10}–C_6H_5–C_6H_5–CN, n=8 (8 OCB)

Figure 3.5: *The chemical formulas of three additional different materials:(i) EPON 828, oligomeric liquid,(ii) propylene carbonate (PC), a low molecular weigth liquid, (iii) octyloxycyanobiphenyl (8*OCB) isomer of liquid crystalline 8OCB, which remains in the isotropic phase on supercooling.*

3.2 Measurements techniques

3.2.1 Dielectric spectroscopy(DE)

3.2.1.1 Basic concepts

There are a number of possibilities to determine $\varepsilon^*(\omega)$. A first classification splits in two possible techniques: time-domain and frequency-domain techniques. Since in this work time-domain techniques have not been used, all our attention will be focused on a number of frequency-domain techniques.

The basis of any measurement of $\varepsilon^*(\omega)$ is essentially a determination of the impedance Z of the sample. It then requires some simple calculations to get the value of $\varepsilon^*(\omega)$. In the simplest case, that of a pure capacitor, the value of the impedance is given by

$$Z_C = \frac{1}{\omega C} \tag{3.1}$$

For the case of a dielectric sample cell, one can use either a measured value of the vacuum capacitance C_0 or the equation for the geometrical capacitance, for example equation (3.1) in the case of a parallel plate capacitor. One gets

$$\varepsilon = \frac{C}{C_0} \tag{3.2}$$

In fact the impedance is a complex value Z^*. The complex form of Z_C can be written as:

$$Z_C^* = \frac{1}{i\omega C} \tag{3.3}$$

This means that also the phase information must be measured to allow the determination of both the real and imaginary parts of $\varepsilon^*(\omega)$. Suppose that a sinusoidal voltage is applied to the sample and the voltage over and current through the sample are determined, including the phase information. This gives:

$$V(t) = V_0 \exp(i\omega t) \tag{3.4}$$

$$I(t) = I_o \exp(i\omega t + i\phi) \tag{3.5}$$

By combining these equations, it follows :

$$Z^* = \frac{V_0}{I_0} \exp(-i\phi) \tag{3.6}$$

which in turn can be used to obtain $\varepsilon^*(\omega)$:

$$\varepsilon^*(\omega) = \frac{-i}{\omega Z^*} \frac{1}{C_0} \tag{3.7}$$

The value obtained for $\varepsilon^*(\omega)$ is that corresponding to the frequency of the applied field, which will also depend on the vacuum capacitance C_0. The value for C_0 can be obtained from a measurement of the empty cell or directly from the knowledge of the geometry of the cell. For the actual measurements, a number of techniques which use equivalent circuit can be used, each having certain limitations, often related to the frequency of the electric field.
The *Impedance Measurement Handbook* from Agilent shows several equivalent circuits which summarize in detail all possible setup combinations [56]. At present, Novocontrol is the leading company that offers complete setups for dielectric spectroscopy measurements that include instruments, high precision heating/cooling control, various accessories as well as a wide range of different software [57].

3.3 Setups used in this work

In this work, the relaxation times were determined by means of broadband dielectric spectroscopy. The measurements were performed with two different setups in two different frequency ranges by using two Novocontrol setups. The first one is the Novocontrol α-analyser spectrometer (HP4192) which makes measurements in the range from 10^{-5}Hz to 10MHz [57,58] which has been used for performing the dielectric measurements of several pure compounds and several mixed crystals.

The measurement at 10^{-5}Hz would require several days to finish, so in practice the low frequency limit is at 1mHz, but even this is only used exceptionally. Typical scans go down to 10mHz or 100 mHz if some signal other that conductivity contributions is expected, otherwise even higher lower limits are used.
The second one is the high frequency: Hewlett–Packard RF Impedance BDS80 (HP4291) which has been used in the Katowice laboratory in Poland for characterizing the pure compounds C8-ol and C7-ol. It covers the frequency range from 1MHz to 1GHz [57,59]. This instrument based on the sample cell connected to a test Head, mounted on a heat sink, from which an insulated cable leads to the analyzer itself. The instrument is very sensitive to the high frequency electrical response of the test head and sample cell and therefore a sometimes tedious calibration procedure is necessary. The calibration procedure starts with a calibration of the instrument and the Test Head using four known standards: an open circuit, a shortcut, a 50Ω resistance and a low-loss capacitor. After this, the sample cell is connected to the Test Head and the so called compensation is started. Now the sample cell is measured as an open circuit, shortcutted and with a standard peace of Teflon as sample. After this procedure, the real sample can be measured.
The low frequency range of the measurements were circumscribed to $10^{-2}Hz$ up $10^{7}Hz$ while the high-frequency were carried out up $10^{9}Hz$. Both Novocontrol setups were equipped with a Quatro temperature controller which is used with a Nitrogen-gas cryostat with the temperature stability at the sample around $0.1K$.

3.3.1 Sample cells

Two diferent cells are used in this work. Both cells form a sandwich capacitor mounted between two different cell: BDS 1200 (for the case of low frequency measurements) and BDS 2200 (for the case of high frequency measurements) [57]. For liquids or powders, additional spacers are used.

3.3.1.1 Low frequency: Liquid Parallel Plate Sample Cell (BDS1308)

For the low frequency case, we used the sample cell BDS1308 which is mounted in our laboratory. This cell has an inner diameter of $20mm$ with two gold plated cup electrode of $14mm$ diameter. The sample is placed between two parallel plates, separated by spacers. A few of $50\mu m$ fibres as a spacer is taken to separate the cup electrode and the top electrode. The liquid sample is then sandwiched between two equally large electrodes from the sample holder. This kind of sample can only be used for samples were evaporation is not a problem: because the sample is in direct contact with the nitrogen flow, it will evaporate. For evaporating samples (i.e those for what the vapor pressure is high) it is then putting in a holder of which the sample space is sealed from the environment by two o-rings and allows adjusting the cell capacity by variation of the electrode spacing. In this case, also teflon spacer rings can be used instead of fibres, allowing thicker samples. The figures (3.6 and 3.7) show the electrode and the cell.

Figure 3.6: *The parallel plate electrodes BDS 1200. The figure was taken from [57]*

Figure 3.7: *The Liquid Sample Cell BDS 1308. The figure was taken from [57]*

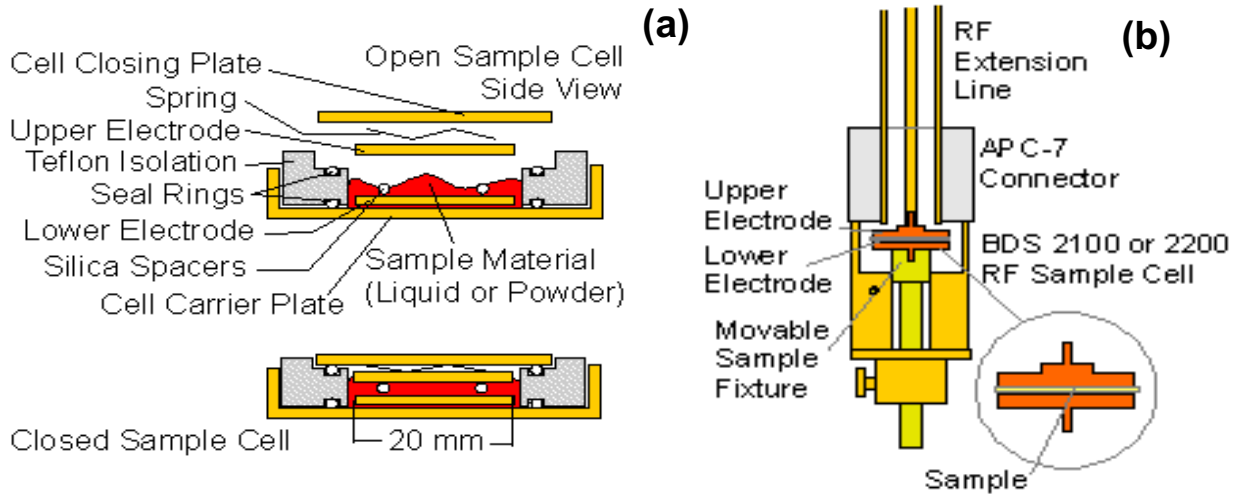

Figure 3.8: *Schematic drawing of the liquid sample cells. The figure (3.8a) and (3.8b) show the cases of the low and high frecuency sample cell. Both figure were taken from [57].*

The figure (3.8a) shows a schematic drawing of the cell in the open and closed state. In the open state, the cell closing plate and upper electrode are removed from the cell, and the sample material covers the lower electrode. The electrode gap is adjusted by silica or Teflon spacers. On the other hand, for the case of closed state, the upper electrode is pressed by the cell closing plate and the spring to the spacers. Liquid sample material, which does not fit between the electrodes, can flow around the upper electrode. The two seal rings attached to the Teflon isolation prevent evaporation of sample materials out of the cell and its connection head is connected to a Pt100 temperature sensor.

3.3.1.2 High frequency: The RF sample cell (BDS 2200)

For the high frequency (radio frequency) case, we used the sample cell BDS2200 which is equipped in the Katowice laboratory in Poland. The sample is prepared between two sandwich electrodes building a sample capacitor similar to the low frequency cell. This cell has an inner diameter $14mm$ with two gold plated cup electrodes of $12mm$ diameter ideal for RF measurements of liquids with low viscosity. Small spacers, for instance $50\mu m$ silica fibers, can be used to separate the cup electrode and the top electrode. The top electrode has a diameter of $10mm$ so that surplus material is pressed out of the electrode area automatically.
The sample is mounted in parallel plate arrangement between two RF external electrodes which are mounted in the RF sample cell as it is showed in the figures (3.9). The RF cell is thermally isolated by the RF extension line which is connected by two-loss precision line with two APC-7 connectors and Pt100 temperature sensor. It is mounted between the impedance input of the RF Analyzer and the RF sample cell for thermal isolation (see figure (3.8b)).
As this setup is very sensitive to mechanical stress, it is supported by the motor driven BDS 2300

Figure 3.9: *The RF parallel plate electrodes BDS 2201. The figure was taken from [57]*

Figure 3.10: *The RF Liquid Sample Cell BDS 2200. The figure was taken from [57]*

Figure 3.11: *The temperature controller experimental setup. The figure was taken from [57]*

mounting rack which allows to move the sample cell in and out of the cryostat by special mechanics, avoiding mechanical forces on the extension line.

3.3.2 Temperature controller: Quatro Cryosystem

The Quatro Cryosystem is a high quality turn key temperature control system for applications in materials research. It can be used with all Novocontrol sample cells for dielectric and impedance spectroscopy. The system was developed to set or ramp the temperature of the sample under test with high accuracy and reproducibility. The system is modular and can be combined with any Novocontrol BDS dielectric or impedance spectrometer. The Quatro controller has four circuits controlling the sample temperature, the gas temperature, the temperature of the liquid nitrogen in the dewar and the pressure in the dewar. In addition the vacuum pressure is measured [57].
The setup consists of a rack, where the electronic parts of the Quatro are mounted, together with a vacuum pump (see figure (3.11)). On a platform on the outside of the rack, a cryostat is mounted. Liquid nitrogen is evaporated from a dewar and the cold gas is sent through a gas heater. After heating the nitrogen continues its way, controlling the temperature of the sample inside the cryostat. The cryogenic part is double-walled and connected to the vacuum pump. The sample holder ends in an active head, from where cables lead to the impedance analyzer. In this work, all measurements have been performed with both impedance analyzers equipped with a Quatro Cryosystem temperature controller using a nitrogen-gas cryostat and with the temperature stability at the sample around $0.1K$.

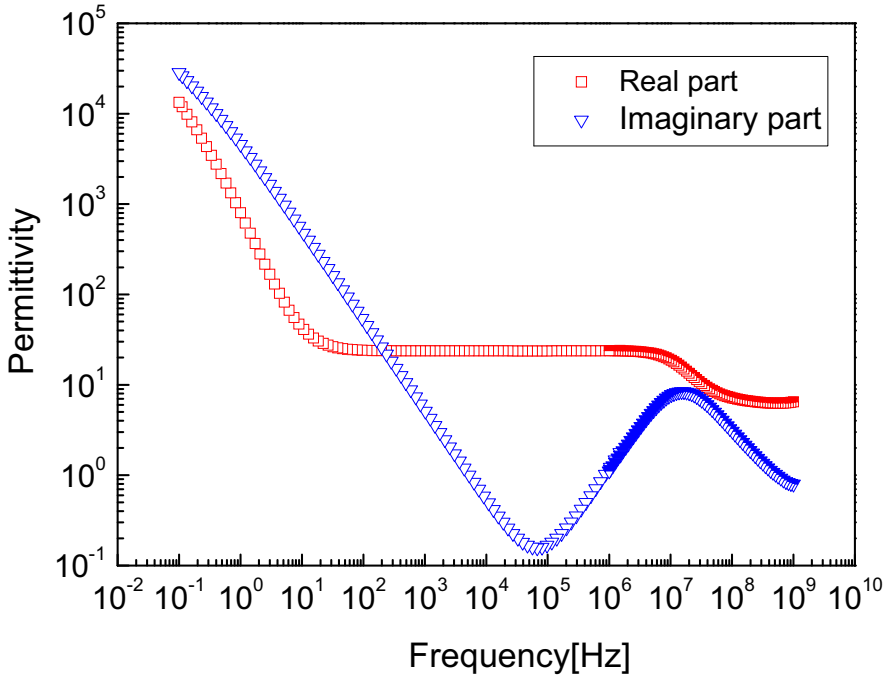

Figure 3.12: *Result of the dielectric measurement of the real and imaginary dielectric permittivity parts of Cycloheptanol (C7-ol). The measurement has been performed at* $T = 273K$.

3.3.3 Example result

Since we will encounter enough dielectric data in the remainder of this work, this section will be limited to one example. In figure (3.12), the result for cycloheptanol C7-ol is shown. The measurements were carried out after slow cooling and stabilization at different temperature steps ($\pm 2K$) to avoid undesirable changes in the kinetics of cooling.

The graph consists of the results of the Novocontrol α-analyser for frequencies below 1MHz and of the HP4291 above this frequency. The high frequency data have been shifted by a multiplicative factor to coincide at 1MHz with those of the Novocontrol. First, between 1MHz and 1GHz one recognizes a relaxation peak in the imaginary part of the permittivity and the corresponding step in the real part. At lower frequencies, the real part stays roughly constant until 103Hz.

In this region, the so-called static value of the permittivity can be obtained. This is the number that appears in literature when looking for "the dielectric permittivity of cycloheptanol". In the same region, and down to 10Hz, the imaginary part shows a rise, matching ohmic conductivity. Around 1Hz the real part shows a downward curvature due to the electrode polarization. In this case, it becomes even so strong that the description with a simple power law is not valid at the lowest frequencies. From about 1Hz on, it is observable that also the steepness of the conductivity in the imaginary part decreases. This gives an impression of what dielectric data look like at a given

temperature. In practice, the analysis of this spectrum would be limited to the region above 1MHz, since the lower frequency part does not contain much information about the molecular dynamics.

3.4 Experimental complementary techniques

In this work, two complementary experimental techniques have been used, the Differential Thermal Analysis (DTA) and the X-ray powder diffraction (XRPD). The first one provides information about the possible phase transitions and their main thermodynamic properties, as temperature and enthalpy or entropy changes, that can appear in a scanned temperature domain. The second one enables to characterize the existence of an underlying crystalline structure for an analyzed phase at a fixed temperature. Both techniques have been used as standard procedures before to engage the dielectric measurements in order to determine the phase behavior of the samples. A brief description of the details concerning the experimental systems used in this work follows in the next sections.

3.4.1 X-ray powder diffraction

High-resolution X-ray powder patterns are isothermically recorded by means of a vertically mounted INEL cylindrical position-sensitive detector $(CPS120)$ [60] equipped with a liquid nitrogen 700 series Cryostream Cooler from Oxford Cryosystems with a temperature accuracy of $0.1K$ and similar for fluctuations. The available temperature range for the system ranges from $500K$ down to $90K$. The detector, used in Debye-Scherrer geometry (transmission mode), consists of 4096 channels and enables a simultaneous recording of the diffraction profile over a 2θ-range between 2 and 115° (angular step of 0.029°in 2θ). Monochromatic $CuK\alpha_1$ radiation ($\lambda(CuK\alpha_1) = 1.5406\mathring{A}$) radiation was selected by means of an asymmetrically focusing incident-beam curved quartz monochromator. The generator power is commonly set to $1.225KW(35kV$ and $35mA)$.
The samples are introduced into 0.5-mm-diameter Lindemann glass capillaries in the liquid or in the solid state at room temperature and are continuously rotated perpendicularly to the X-ray beam during data collection to improve averaging of the crystallites.
External calibration by means of cubic phase $Na_2Ca_3Al_2F_{14}$ [61] is performed for channels to be converted into 2θ-degrees by means of cubic spline fittings. The peak positions were determined after pseudo-Voigt fitting by using the PEAKOC application from DIFFRACTINEL software [62]. Figure (3.13(a))shows a set of examples of experimental X-Ray profiles as a function of temperature obtained on cooling for Cyanocyclohexane within the temperature range of the OD and OG phases. The high symmetry of the lattice (face centered cubic) gives rise to patterns in which a few number of Bragg reflections emerge, in particular for this case, only$[111]$ and$[200]$. Figure (3.13(b)) shows the lattice parameter variation as a function of temperature obtained after the X-ray profiles have been processed according to the procedure previously described. It can be seen

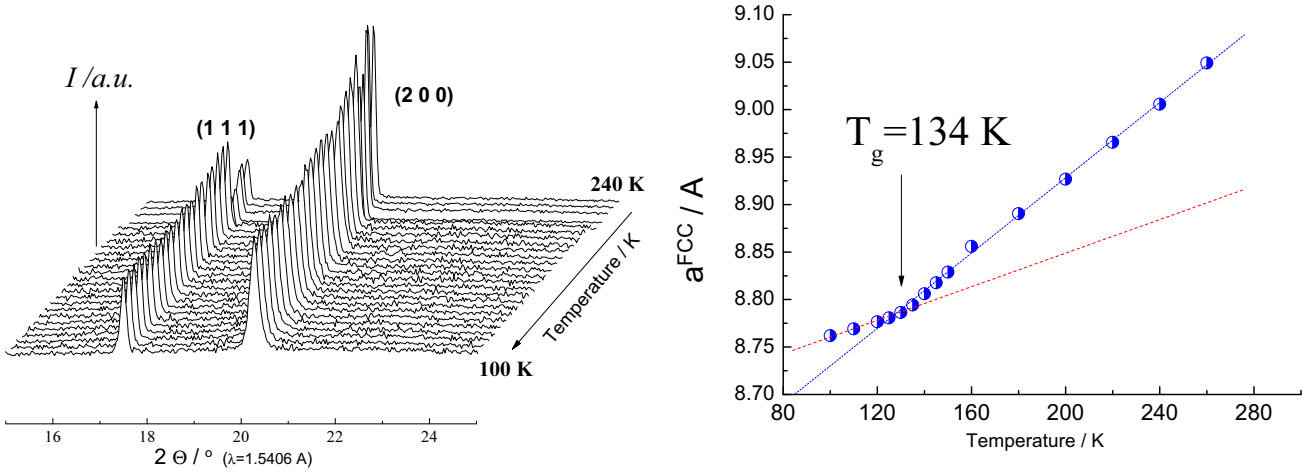

Figure 3.13: *(a) High-resolution X-ray powder diffraction profiles as a function of temperature for the OD phase and the OG of CNc6 below 240K down to 100 K. Miller indexes [hkl] for the two Bragg peaks are indicated. (b) Cubic lattice parameter as a function of temperature obtained from the X-ray profile refinements of CNc6 within the same temperature range as in (a). Dotted lines represent the linear fits for the OD (blue) and OG (red) lattice parameters.*

that the glass transition temperature, from the *OD* to the *OG* on cooling, is clearly visible by a bending of such variation. This finger plot is very characteristic for the glass transitions because it points out the continuity on the volume variation along the transition, but a clear discontinuity on the thermal-expansion, as a consequence of the change of the slope above and below the transition temperature ($134K$ in this case).

3.4.2 Differential Thermal Analysis

Differential Thermal Analysis (DTA) is the most common technique to reveal the thermodynamic changes as a function of temperature for a given sample. When compared with adiabatic calorimetry, DTA has the enormous advantage of requiring less time and less material. Through DTA, samples as small as a few milligrams are scanned at a rate, which is as a rule between 1 and $10Kmin^{-1}$. In adiabatic calorimetry, samples have masses that range from $0.5g$ to some$10g$, and a complete experiment easily takes two weeks. Adiabatic calorimetry, on the other hand, is a byword for accuracy and precision. And not significantly, adiabatic calorimetry is a better guarantee for thermodynamic equilibrium.

The adjective 'differential' expresses the fact that the measured quantity is a difference between the sample and a reference, both being kept under the same experimental conditions [50]. In the case of DTA, the measured difference is a difference in temperature between the sample and an inert reference within the temperature scanned range. This temperature difference is translated to a difference of "heat flow", which is the magnitude measured by means of the differential scanning

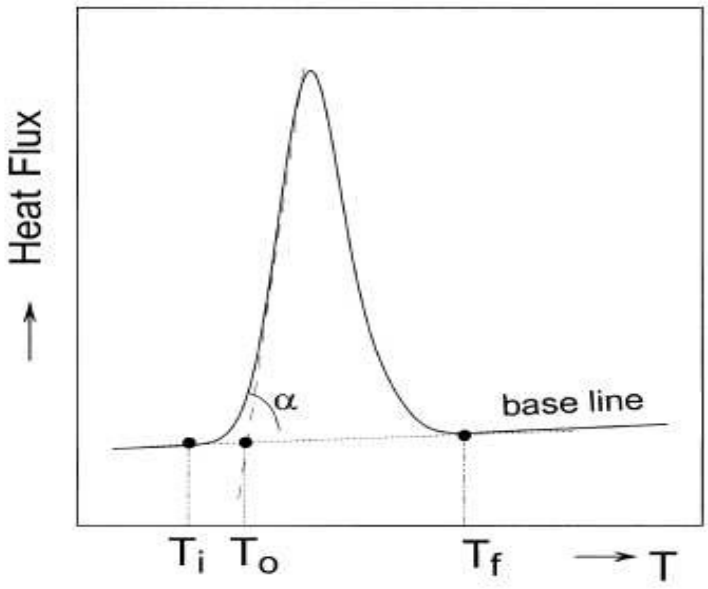

Figure 3.14: *Typical heat flux against temperature for a thermogram that corresponds to the melting or a solid-solid (first order) phase transition for a sample.*

calorimetry technique.

In the case of organic materials, as all involved in this work, it is desirable to encapsulate the sample under an inert atmosphere to prevent evaporation, and to avoid sample oxidation. It must be realized that the material under investigation has a certain vapour pressure, and that the dead volume of the sample container, as a result, will be saturated with vapour. During a heating experiment, the vapour pressure increases, and it means that there is some uncertainty as to the pressure exerted on the material at a solid–solid or a solid–liquid transition. Strictly speaking for the case of containers with no other material than the system to be studied as well as for pure substances, triple points are measured rather than normal melting points [63-65]. In the majority of cases, the influence of vapour pressure on solid–solid and solid–liquid transition temperatures can be neglected as their contribution is less than the experimental uncertainties.

A first order phase transition of a pure substance is an isothermal event, which implies that over the whole rising edge of the thermogram the temperature of the sample does not change (see figure 3.14). At the end of the event, the recording signal returns to the baseline in a more or less exponential manner. At T_f, which is called the final peak temperature, the recording is back at the baseline. At the ascending edge of the thermogram, T_i, which is called initial peak temperature, is the temperature at which the recording starts to deviate from the baseline; and T_o is the so-called onset temperature. Obviously, the onset temperature is representative of the first order phase transition temperature of the process. More precisely, instruments are calibrated with pure substances such that the observed onset temperatures are identified with the melting temperatures of the sub-

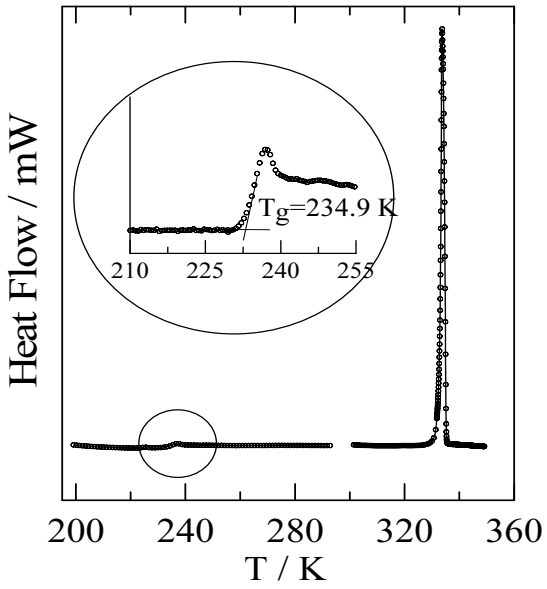

Figure 3.15: *Typical thermogram for a glass forming material. The peak corresponds to the melting of the solid phase, whereas the low-temperature points and the inset (which corresponds to a magnification) depicts the glass transition after the liquid has been quenched at low temperature.*

stances. In this work the melting of Indium has been used as the reference melting temperature for calibration purposes. This calibration enables also to evaluate the area under the peak of the thermogram, making allowance for the course of the baseline, and to establish the corresponding value of the enthalpy change associated with the phase transition.

For a mixed crystalline sample having a certain composition X, the change from solid to liquid or solid to solid, as a rule, are non-isothermal events. The thermogram of these events will be the result of a complex interplay between the characteristics of the instrument, the applied heating rate, the thermodynamic characteristics of the transition and the preparation of the sample. Details are largely detailed in reference [66].

As far as the glass transition is concerned, it should be taken into account that we are dealing with a non-equilibrium phase transition, because it involves a non-equilibrium state, the glass state. It then means that the characteristic thermogram for such a transition strongly depends on the measurements conditions as well as on the aging in the glass state.

In figure (3.15) we show a typical example for a glass forming material. It concerns the case of ternidazole. After the melting process, which manifests as an endothermal peak, the liquid is quenched at low temperature and a subsequent heating makes clear the emergence of the glass transition between the glass state and the supercooled liquid.

In this work the DTA measurements have been conducted by means of a TA Q100 thermal analyzer from TA instruments equipped with a RCS low-temperature device which enables to reach temperatures as low as $183K$. Heating and cooling rates within the range of 2 and $10Kmin^{-1}$ have

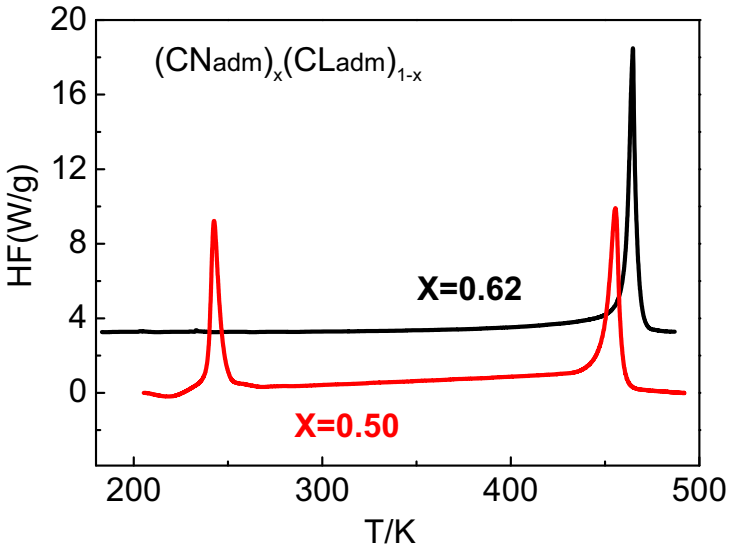

Figure 3.16: *Differential termal analysis thermograms obtained for two mixed crystals, X=0.62 and X=0.50, of the binary system of* $(CNadm)_X(Cladm)_{1-X}$. *For the former, only an endothermic peak revealing the melting of the face centered cubic OD phase emerges, whereas, for the latter, an solid-solid phase transition from low-temperature ordered phase to the OD phase appears in addition to the melting of the OD phase.*

been used. Sample masses between 10 and 25*mg* have been encapsulated into normal *Al* pans from *TA* or into high-pressure stainless steel pans with *Au* covers from Perkin-Elmer. The latter have been used in order to prevent reaction with the container or for compounds with high vapour pressure. The latter correspond to the case of samples involving adamantane derivatives, for which the high-temperature of the melting point combined with the high vapour pressure made necessary the use of such a experimental requirements. Two examples corresponding to mixed crystals of the cyanoadamantane + chloroadamantane two-component system are displayed in figure (3.16). It can be seen that for the mixed crystal with a molar fraction of 0.62 of cyanoadamantane only the melting of the *OD* phase appears, whereas for the equimolar composition a transition from an ordered low-temperature phase to the *OD* is found.

Bibliography

[1] A. Drozd-Rzoska, J. Chem. Phys **130**, 234910, (2009).

[2] A. Drozd-Rzoska, S. J. Rzoska, S. Pawlus, J. Zioło, Phys. Rev. E **72**, 031501, (2005).

[3] *The Plastic Crystalline State*, edited by J.N. Sherwood (Wiley, New York, 1979).

[4] R. Puertas, M. A. Rute, J. Salud, D. O. López, S. Diez, J. C. van Miltenburg, L. C. Pardo, J. Ll. Tamarit, M. Barrio, M.A. Pérez-Jubindo, M.R. de la Fuente, Phys. Rev. B **69**, 224202, (2004).

[5] A. Drozd-Rzoska, S. J. Rzoska, S. Pawlus, J. Ll. Tamarit, Phys. Rev. B. **73**, 224205, (2006).

[6] A. Drozd-Rzoska, S. J. Rzoska, S. Pawlus, J. Ll. Tamarit, Phys. Rev. B. **74,** 064201, (2006).

[7] J. Ll. Tamarit, M. A. Pérez-Jubindo, M. R. de la Fuente, J. Phys.: Condensed Matter **9**, 5469, (1997).

[8] R. Puertas, J. Salud, D. O. López , M. A. Rute, S. Diez, J. Ll. Tamarit , M. Barrio M. A. Pérez-Jubindo, M. R. de la Fuente, L. C. Pardo, Chem. Phys. Lett **401**, 368, (2005).

[9] D. L. Leslie-Pelecky, N. O. Birge, Phys. Rev. Lett **72**, 1232, (1994).

[10] R. Brand, P. Lunkenheimer, A. Loidl, Phys. Rev. B **56**, R5713, (1997).

[11] J. Timmermans, J. Chem. Phys **35**, 331, (1938).

[12] R. Brand, P. Lunkenheimer, A. Loidl, J. Chem. Phys **116**, 10386, (2002).

[13] P. Lunkenheimer, R. Brand, U. Schneide, A. Loid, Phylos. Mag. B **79**, 1945, (1999).

[14] R. Puertas, M. A. Rute, J. Salud, D. O. López, S. Diez, J. C. van Miltenburg, L. C. Pardo, J. Ll. Tamarit, M. Barrio, M. A. Pérez-Jubindo, M. R, de la Fuente, Phys. Rev. B **69**, 224202, (2004).

[15] M. A. Rute, J. Salud, P. Negrier, D. O. López, J. Ll. Tamarit, R. Puertas, M. Barrio. M, Mondieig. D, J. Phys. Chem. B **107**, 5914, (2003).

[16] H. Suga, S. Seki, J. Non-Cryst. Solids **16**, 171, (1974).

[17] L. P. Singh, S. S. N. Murthy, J. Phys. Chem. B **112**, 2606, (2008).

[18] D. L. Leslie-Pelecky, N. O. Birge, Phys. Rev. Lett **72**, 1232, (1994).

[19] D. L. Leslie-Pelecky, N. O. Birge, Phys. Rev. B **50,** 13250, (1994).

[20] P. K. Dixon, L. Wu, S. Nagel, B. D. Williams, J. P. Carini, Phys. Rev. Lett **65**, 1108, (1990).

[21] M. Shablakh, L. A. Dissado, R. M. Hill, J. Chem. Soc., Faraday Trans **79**, 383, (1983).

[22] M. Tyagi, S. S. N. Murthy, J. Chem. Phys **114**, 3640, (2001).

[23] J. Salud et al., J. Non-Cryst. Solids **355**, 2550, (2009).

[24] A. Gonthier-Vassal, H. Szwarc, Chem. Phys. Lett **129**, 5, (1986).

[25] J. Reuter, T. Brückert , A. Würflinger, Z. Naturforsch : Phys. Sci **48**, 705, (1993).

[26] H. J. Schneider, V. Hopper, J. Org. Chem **43**, 3866, (1978).

[27] J. R. Durig et al., J. Mol. Struct **967**, 99, (2010).

[28] K. Kishimoto, Bul. Soc. Japan **51**, 1691, (1978).

[29] K. Kobashi, T. Kyomen, and M. Oguni. J. Phys. Chem. Solids **59**, 667, (1998).

[30] T. Clark, T. Mc, O. Knox, H. Mackle, M. A. McKervey. J. Chem.Soc., Faraday Trans **173**, 1224, (1977).

[31] Y. Huang, D. F. R. Gilson, I. S. Butler, and F. Morin, J. Phys. Chem **95**, 2151, (1991).

[32] L. A. Fraczyk , Y. Huang, Spectrochim. Acta, Part A **57**, 1061, (2001).

[33] M. Descamps, J. F. Willart, G. Odou, and K. Eichhom, J. Phys **I2**, 813, (1992).

[34] F. Affouard, M. Descamps, Phys. Rev. B **59**, R9011, (1999).

[35] K. Pathmanathan, G. P. Johari, J. Phys. C **18**, 6535, (1985).

[36] K. Kobashi, T. Kyomen, M. Oguni, J. Phys. Chem. Solids **5,** 667, (1998).

[37] F. Affouard, E. Cochin, R. Decressain, M. Descamps, Europhys. Lett **53,** 611, (2001).

[38] F. Affouard, J. F. Willart, M. Descamps, J. Non-Cryst. Solids **9**, 307, (2002).

[39] J. L. Sauvajol, M. Bee, J. P. Amoureux, Mol. Phys **46**, 811, (1982).

[40] O. Yamamuro, M. Ishikawa, I. Kishimoto, J. J. Pinvidic, and T. Matsuo, J. Phys. Soc. Jpn. **68**, 2969, (1999).

[41] J. P. Amoureux, J. L. Sauvajol, M. Bee, Acta Crystallogr, Sect. A:Cryst. Phys., Diffr., Theor. Gen. Crystallogr. **37**, 97, (1981).

[42] J. J. M. Ramos, Mol. Phys **90**, 235, (1997).

[43] P. Brol et al., J. Mol. Struct **704**, 115, (2004).

[44] J. P. Amoureux, M. Bee, Acta Crystallogr., Sect. B: Struct. Crystallogr.Cryst. Chem **35**, 2957, (1979).

[45] J. P. Amoureux, M. Bee, J. L. Sauvajol, Mol. Phys **45,** 709, (1982).

[46] M. Foulon, J. P. Amoureux, J. L. Sauvajol, J. P. Cavrot, M. Muller, J. Phys. C **17**, 4213, (1984).

[47] J. P. Amoureux, G. Noyel, M. Foulon, M. Bee, L. Jorat, Mol. Phys **52**, 161, (1984).

[48] J. P. Amoureux, M. Castelain, M. D. Benadda, M. Bee, J. L. Sauvajol, J. Phys. Paris **44**, 513, (1983).

[49] M. Tyagi, S. S. N. Murthy, J. Chem. Phys. **114**, 3640, (2001).

[50] M. Descamps, C. Caucheteux, G. Odou, and J. L. Sauvajol, J. Phys.Paris, Lett **45**, L719, (1984).

[51] L. Carpentier, R. Decressain, and M. Descamps, J. Chem. Phys 1**28**, 024702, (2008).

[52] S. A. Lusceac, I. Roggatz, J. Gmeiner, E. A. Rössler, J. Chem. Phys **126**, 014701, (2007).

[53] S. Pawlus, M. Mierzwa, M. Paluch, S. J. Rzoska, C. M. Roland, J. Phys.: Condens. Matter **22**, 235101, (2010).

[54] A. Drozd-Rzoska, S. J. Rzoska, Phys. Rev. E **73**, 041502, (2006).

[55] S. Corezzi, M. Beiner, H. Huth, and K. Schroeter, S. Capaccioli, R. Casalini, D. Fioretto, E. Donth, J. Chem. Phys **117**, 2435, (2002).

[56] Impedance Measurement Handbook (Agilent Technologies, 2006).

[57] URL http://www.novocontrol.de.

[58] Hewlett-Packard, HP4192 Precision LCR Meter: Operation Manual (1996).

[59] Hewlett-Packard, HP4291 RF Impedance/Material Analyzer: Operation Manual (1998).

[60] J. Ballon, V. Comparat, J. Pouxe, Nucl. Instrum. Methods **217**, 213, (1983).

[61] M. Evain, P. Deniard, A. Jouanneaux, R. Bre, J. Appl.Crystallogr **26**, 563, (1993).

[62] O. Masson, A. Ramponi, PEAKOC Program; Laboratoire de Matériaux Céramiques et Traitements de Surfaces, CNRS-ENSCI, Limoges, France, (1996).

[63] A. Drozd-Rzoska, S. J. Rzoska, S. Pawlus, J. Ll. Tamarit, Phys. Rev.B **73**, 224205, (2006).

[64] A. Drozd-Rzoska, S. J. Rzoska, S. Pawlus, J. Ll. Tamarit, Phys. Rev.B **74,** 064201, (2006).

[65] J. P. Amoureux, M. Sahour, C. Fernandez, and P. Bodart, Phys. StatusSolidi **143**, 441, (1994).

[66] H. A. J. Oonk, J.Ll. Tamarit, in: R.D. Weir, T.W. de Loos (Eds.), Measurement ofof Thermodynamic Properties of Multiple Phases Experimental Thermodynamics (IUPAC), vol. VII, Elsevier, Amsterdam, 2005 (Chapter 9).

Chapter 4

Data Analysis

In this chapter we focus on the data analysis procedure used in this work. Three subjects will be covered. The brief first section is devoted to the basic procedure of dielectric data analysis. We show the basic procedure for processing dielectric experimental data, in particular to obtain the relaxation time, as well as the procedure to analyze the temperature dependence of the derived relaxation time. Some details are given for the developed program (vitreousparameter.nb) which is supported by means of the Mathemathic platform. A new method for studying the dynamic of glass forming systems is introduced and the minimization procedure is discussed. The last part is devoted to the minimization procedure used for the data refinement according to the Mauro's equation.

4.1 Dielectric data analysis

4.1.1 Basic procedure

As a characteristic and well known feature of glass forming materials, we observed that dielectric loss is asymmetrically broadened with respect to the simplest Debye behaviour. This dispersion can numerically be well accounted as a function of radian frequency, using the empirical formula given by Havriliak-Negami (HN). Due to the presence of charged impurities, a dc-conductivity has to be accounted for, so that the total contributions to the dielectric permittivity can be modelated as a superposition of the general Havriliak Negami part, which accounts for all relaxations regions denoted by: $k = \{1,2,3\}$ and a conductivity term [1]. It allows the following equation

$$\varepsilon^{\star}(\omega) = -i\left(\frac{\sigma_0}{\varepsilon_0 \omega}\right)^N + \sum_{k=1}^{3}\left[\frac{\Delta\varepsilon_k}{\left(1+(i\omega\tau_k)^{\alpha_k}\right)^{\beta_k}} + \varepsilon_{\infty k}\right] \tag{4.1}$$

For ohmic contacts and no Maxwell-Warner-polarization $N = 1$ holds, but in the most practical cases $0.5 < N < 1$ is obtained.
The figure (4.1) shows an schematic representation of the equation od the real $\left(\varepsilon^{'}\right)$ and imaginary

$\left(\varepsilon^{''}\right)$ parts of equation (4.1). The increase at low frequencies in $\varepsilon^{''}$ is due to the conductivity term, where the slope of the increase is determined by the exponential factor N.

For each relaxation process, the dielectric strength $\Delta\varepsilon_k = \varepsilon_{sk} - \varepsilon_{\infty k}$ gives the diference in $\varepsilon^{'}$ at very low and infinity frecuencies, being also proportional to the area below $\varepsilon^{''}$ relaxation peak. The value $\varepsilon^{'}$ at infinite frequencies is determined by ε_{∞}. For common values of the Havriliak Negami shape parameters α,β, the maximum of the relaxation peak in $\varepsilon^{''}$ is approximately situated at $1/(2\pi\tau)$. The width parameter α specifies the slope of the low frequency side whereas $-\alpha\beta$ gives the slope of the high frequency side of the relaxation in $\varepsilon^{''}$. Each parameter can be estimated by a standard fitting procedure, which involves a minimization process of the following equation

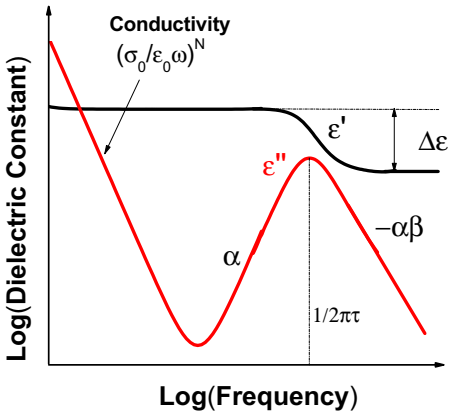

Figure 4.1: *Schematic representation of the real (black) and imaginary (red) dielectric permittivity parts of the equation (4.1).*

$$\sum_i \Gamma_i \left[\varepsilon^{\star}_{exp} - \varepsilon^{\star}(\omega_i)\right]^2 \Rightarrow min \tag{4.2}$$

where Γ_i is a weigthing factor which can be used to take into consideration the different accuracy of data measured with different setups, while i counts the experimental points.

4.1.1.1 Evaluation of dielectric spectra

Figure (4.2) shows two examples of the dielectric loss spectra of C8-ol (A) and C7-ol (B) at a given temperature in their simple cubic OD phases [2]. In addition to the well-pronounced α-relaxation peaks with a continuous temperature shift (characteristic for the freezing of the molecular dynamics), secondary relaxations clearly show up. The combination of the HN function for the α-relaxation process and Cole-Cole (CC) functions for the secondary processes (β and γ for C8-ol and γ for C7-ol) provides more than acceptable fits with a very good physical consistency for the obtained parameters.

The model functions used in this work were fitted to dielectric data by the standard software package **WinFIT**, which is especially designed for dielectric and impedance fits [3]. It gives a fast routine for the optimization of the equation (4.2), allowing an analytical evaluation of dielectric spectra. The main feature of **WinFIT** is non linear curve fitting of the measured data in the frequency and time domain. We used it for evaluating the dielectric relaxation function with up to three terms and a conductivity term. The measured data can be imported in several binary and flexible ASSCII formats, displaying the data and fit function in an online window. A two-dimensional

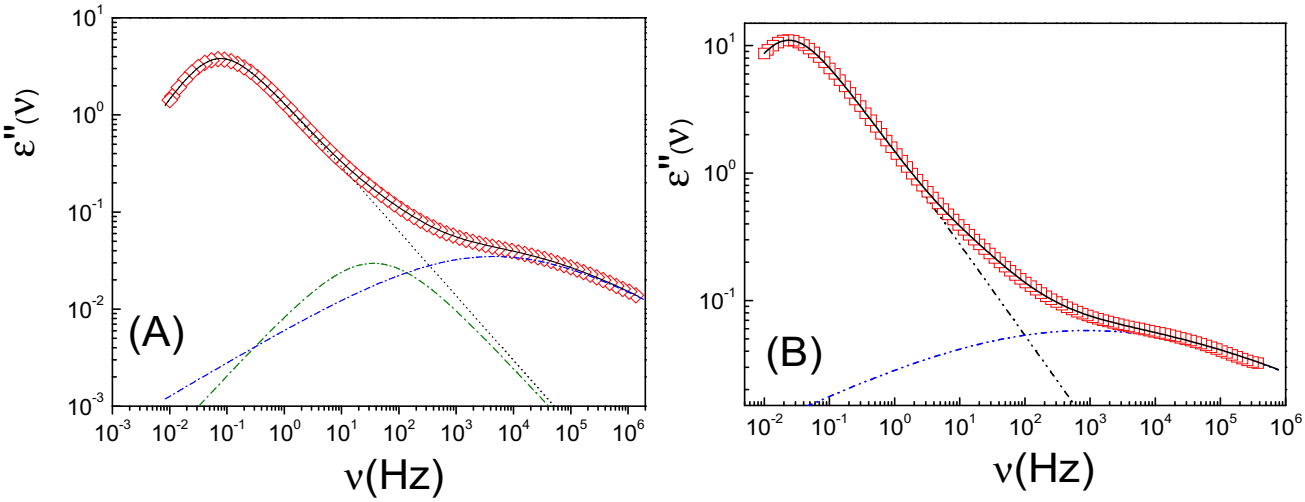

Figure 4.2: *Double logarithmic representations of the dielectric loss spectra of C8-ol (A) and C7-ol (B) at two representative temperatures (176 K and 148 K, respectively). Solid lines are fitted curves corresponding to the sum of a HN and one (B) or two (A) CC functions for the cases of (C7-ol) and (C8-ol), respectivetly. The dashed lines show the CC parts of the fits for the β-and γ-relaxation processes.*

structure is supported, allowing to handle data not only in dependence on frequency, but also on another independent variable like temperature.

A large number of diagrams and windows options are available. Data and fit functions can be displayed in several two-dimensional representations as a series of curves, where the graphic of the measured data can be manipulated intercatively. This includes shifting, deleting and inserting data points with a mouseclick. Multiplication of whole data curves in a selectable frequency range and connection of data curves being measured in different frequency ranges is just one mouseclick away. In order to do a fit, the mean square deviation $\mathscr{L}$ of the measured data is optimized. It is defined by the following equation

$$\mathscr{L}(\sigma_0, N, \Delta\varepsilon, \varepsilon_\infty, \tau, \alpha, \beta) = \sum_{i=1}^{n} \frac{\left[\varepsilon''(\omega_i, \sigma_0, N, \Delta\varepsilon, \varepsilon_\infty, \tau, \alpha, \beta) - \varepsilon''_{mes}(\omega_i)\right]^2}{i-1} \tag{4.3}$$

were $\varepsilon''_{mes}(\omega_i)$ are the measured data points for ε'' at circular frequency ω and the sum is taken over all data points having been measured. As the mean square deviation has more than one local minimun, **WinFIT** finds the optimal fit only if the initial paramters (the parameters before the automatic fit is started) are close enough to the optimal minimun.

Figure (4.3) shows examples of dielectric spectra of C7-ol for two representatives temperatures below and above the glass tansition temperature T_g. **WinFIT** also provides the way for processing datas below T_g .

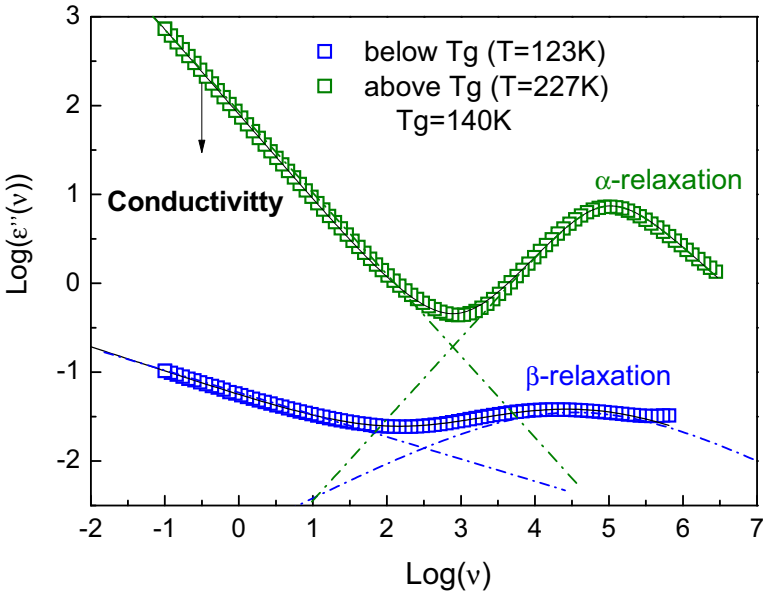

Figure 4.3: *Double logarithmic representations of dielectric loss spectra of (C7-ol) at two representative temperatures, below (123 K, blue squares) and above (227 K, green squares) the glass transition temperature (140 K). The solid line curves are fits corresponding to a sum of a power law to account for the conductivity and a CC function for the β- relaxation for the spectrum at 123 K, and to a sum of a power law and a Havriliak-Negami function for the spectrum at 227 K.*

4.1.2 The temperature dependence of the relaxation times

Once the relaxation times have been determined with the procedures described in the previous section, the temperature dependence of the relaxation times can be analysed. In practice two expressions are commonly used to express the temperature dependence of the primary and secondary relaxation processes. The first one is the Arrhenius equation, originally introduced to describe chemical reactions. The second one is the Vogel–Fulcher–Tamman (VFT) equation, introduced to describe the non-Arrhenius dependence in many glass-forming systems. We have performed a program working under the Mathemathic framework (vitreousparameter.nb) which allows us the possibility to estimate the set of parameters for a selected model as well as the fragility index.

4.1.2.1 Arrhenius dependence

The mathematical expression characterizing, the temperature dependence of a chemical reaction time in terms of an activation energy, was discovered by Arrhenius [4] acording to the law:

$$\tau = \tau_0 \exp\left(\frac{\Delta E}{RT}\right) \tag{4.4}$$

where τ_0 is a time independent factor, which was related to the average phonon frequency which is associated only with the high temperature dynamical domain and $\triangle E$ is the activation energy,

that does not depend on temperature either. The Arrhenius equation describes the temperature dependence of the relaxation times of a process where a temperature-independent potential barrier has to be crossed as the case of secondary relaxation processes.
Linearization of this equation shows that an Arrhenius process shows up as a straight line when the relaxation times are plotted versus the inverse temperature, and the slope of this line is proportional to the activation energy. Thus, the plane logarithm of the relaxation time – reciprocal of the temperature (the so-called Arrhenius plot) is commonly used to show up the temperature dependence of the dynamics.

4.1.2.2 VFT equation

The variation of the primary relaxation time with temperature is generally non-Arrhenius. That is, on cooling, almost always increases faster than predicted by the Arrhenius equation. For ultra-viscous liquids, it is generally found that $\triangle E(T)$ increases significantly on cooling. There are no liquids where $\triangle E(T)$ decreases [5], which is in itself a striking fact.
The form of the evolution $\triangle E(T)$ is unknown, so efforts of researchers are being focused on equations which empirically proved their validity [6-11]. Undoubtedly for the last decades the most commonly accepted was the Vogel-Fulcher-Tammann (VFT) equation [12-14], which was introduced as a fitting function for the curved relaxation time behaviour for glass-forming liquids. Later on it has received some different theoretical explanations, mainly based on free volume and Adam – Gibbs theories [6].
The VFT equation is usually given in the form

$$\tau = \tau_0 \exp\left(\frac{DT_0}{T - T_0}\right) \tag{4.5}$$

where τ_0 is the high temperature limit of the relaxation time, D is related to the fragility of the glass-former and T_0 is the Vogel temperature associated with the estimation of the ideal glass transition temperature.

4.1.2.3 Estimation of the vitreous parameters

Using the temperature relaxation time dependence we can estimate the glass transition temperature T_g (the temperature at which the dielectric relaxation time reaches 10^2s) and the fragility index m (estimated as $\frac{\partial \log_{10}\tau}{\partial(T/T_g)}|_{T_g}$) by the fits of the functions in the Arrhenius plot ($f_{1000/T} = \log_{10}\tau\left(\frac{1000}{T}\right)$) and in the Angell plot ($f_{T_g/T} = \log_{10}\tau\left(\frac{T}{T_g}\right)$). We have been developed a mathematic notebook (**vitreousparameter**.nb) which gives us the possibility for getting these fitting functions.
The **vitreousparameter** function allows us to find a least squares fit for a set of relaxation time data according to a model. The model argument of **vitreousparameter** must be completely specified by the symbols in the variables argument and the symbols in the parameters argument as is showed in

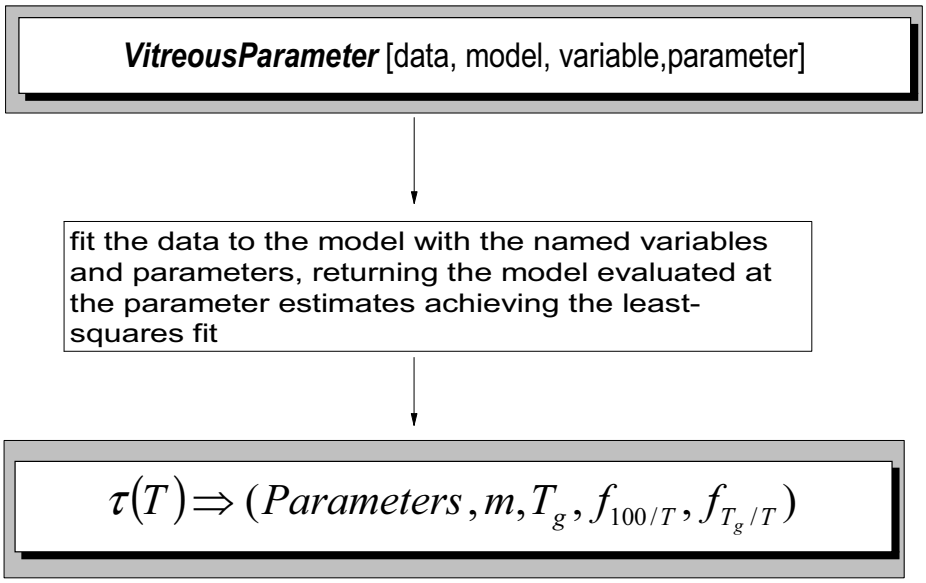

Figure 4.4: *The figure shows a squematic representation of the mathematic file notebook (**vitreousparameter**.nb) routine. Once the temperature dependence of the relaxation times have been determined, the data is enter to the program which allows us the fit of functions in the Arrhenius ($f_{1000/T} = \log_{10}\tau\left(\frac{1000}{T}\right)$) and the Angell ($f_{T_g/T} = \log_{10}\tau\left(\frac{T}{T_g}\right)$) representations. The fragility index m and the glass tansition temperature T_g are also calculated by the use of (**vitreousparameter**.nb).*

figure (4.4). The variables argument specifies the independent variables represented in the relation time data. The parameters argument specifies the model parameters for which we would like estimates. The data argument can be a list of vectors of the independent variables. The estimates of the model parameters are chosen to minimize a function of merit given by the sum of squared residuals. The figures (4.5) and (4.6) show example results obtained by the use of this program.

4.1.3 Derivative Analysis

The following equation can be obtained from [15]:

$$\frac{d\ln\tau}{d\left(1/T\right)} = \frac{H_a(T)}{R} = H_a^{'} \tag{4.6}$$

where $H_a(T)$ is the apparent activation enthalpy and R is the universal gas constant.
As shown in [15] a derivative based analysis of the VFT equation yields:

$$\left[\frac{d\ln\tau}{d\left(1/T\right)}\right]^{-1/2} = \left[\frac{H_a(T)}{R}\right]^{-1/2} = \left(H_a^{'}\right)^{-1/2} = \left[\left(D_T T_0\right)^{-1/2}\right] - \frac{\left[T_0\left(D_T T_0\right)^{-1/2}\right]}{T} = A - \frac{B}{T} \tag{4.7}$$

where a linear regression analysis gives $T_0 = B/A$ and $D_T = 1/AB$.

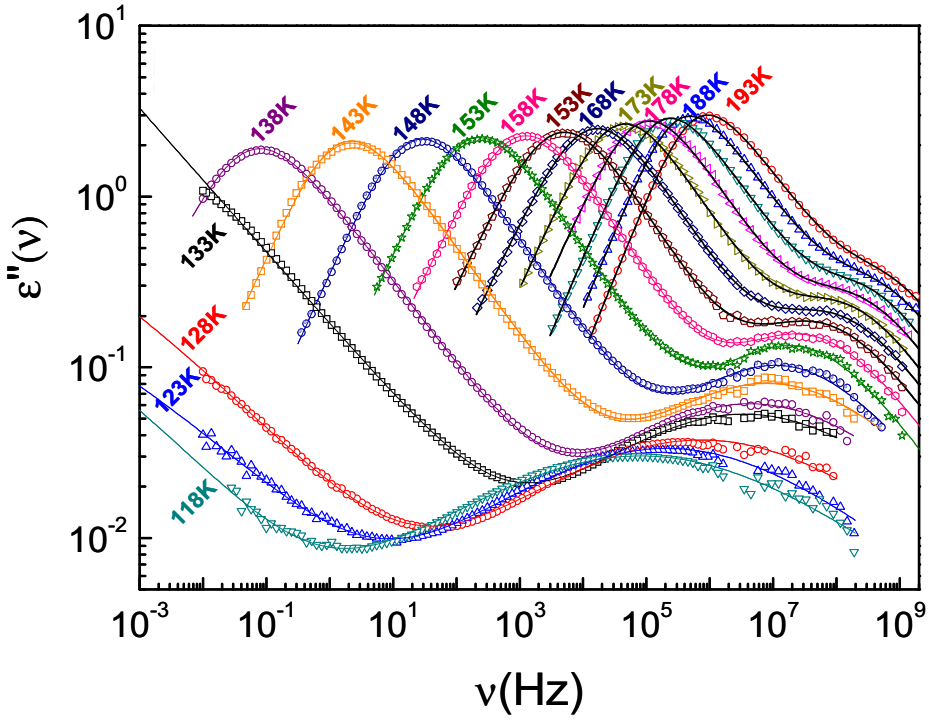

Figure 4.5: *Double logarithmic representations of dielectric loss spectra of CNc6. The curves from left to rigth correspond to the temperatures 118 to 193 K with a temperature step of 5K. For temperatures below and above $T_g = 134K$, two diferent fitiing functions are used. For temperature above T_g the lines show fits to the data by using the equation (4.1). For temperatures below T_g the lines show fits with the sum of a power law and a Cole-Cole (CC) function. Both fittings have been performed using the basic procedure described in the previous section.*

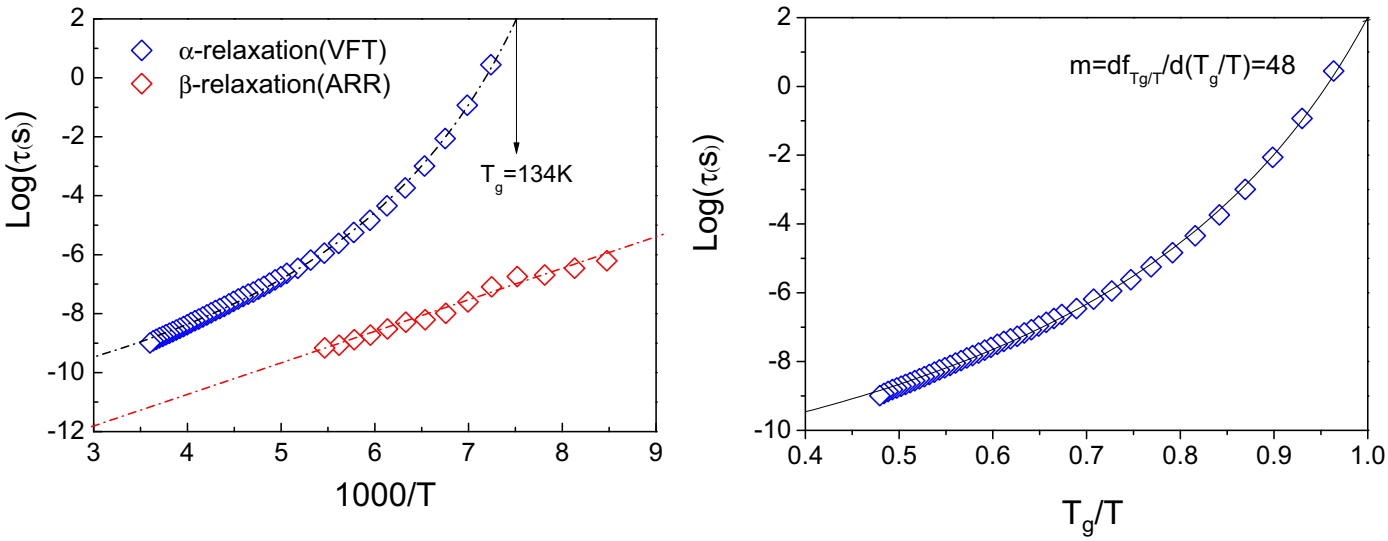

Figure 4.6: *Arrhenius (left) and Angell (rigth) plot of the temperature relaxation time data for the case of (CNc6). The blue and red points in the left figure show the non-Arrhenius and Arrhenius behaviour respectively. The solid lines show the fitting functions $f_{1000/T}$ and $f_{T_g/T}$ which have been obtained using the mathematic notebook (**vitreousparameter**.nb).*

The analysis indicated above resembles the transformation introduced by Stickel et al. [16], although the latter did not introduce explicitly the activation enthalpy and solely focused on detecting the dynamical crossover. Following equation (4.7), the domain of validity of the VFT equation in the plot $\left(H_a^{'}\right)^{-1/2}$ vs $1/T$ is directly visualized by a linear dependence. The linear regression yields optimal values of T_0 and coefficient D_T. Consequently, they can be substituted into the VFT equation, reducing the final fit solely to prefactor τ_0 [15].
For the "Avramov" equation, a similar linearized, derivative based analysis leads to [17]:

$$\log\left[\frac{d\ln\tau}{d\left(1/T\right)}\right] = \log H_a^{'} = \log\left(CD\right) + \left(1-D\right)\log T = A + B\log T \tag{4.8}$$

On the plot $\log H_a^{'}$ vs $\log T$, the linear domain indicates the range of validity of the Avramov equation. Then the linear regression yields optimal values of coefficients: $D = 1 - B$ and $C = {10^A}/{(1-B)}$.
Similar reasoning can be used for the DSM model equation, which is giving [17]:

$$\frac{T^2}{H_a^{'}(T)} = \frac{T_c}{\phi} - \frac{T}{\phi} = A - BT \tag{4.9}$$

Experimental data presented in the plot ${T^2}/{H_a^{'}(T)}$ vs T, should exhibit a linear behaviour in the domain of validity of the critical like equation. The subsequent linear regression yields the optimal values of parameters $T_c = {A}/{B}$ and $\phi = 1/B$. The final fitting is reduced $\tau(T)$ solely to prefactor τ_0. The analysis via equation (4.10) indicates also the high temperature domain of validity of the mode-coupling theory (MCT) [8,18]:

$$\tau(T) = \tau_0\left[\frac{T - T_C^{MCT}}{T_C^{MCT}}\right]^{-\phi^{'}} \tag{4.10}$$

where T_C^{MCT} denotes the crossover temperature from the ergodic to the non-ergodic behavior. The 'critical' temperature T_C^{MCT} correlates with the dynamical crossover temperature acording to the MCT.
Similar reasoning as above can be used for Elmatad et al. equation [19], leads to the dependence:

$$\frac{d\ln\tau}{d\left(1/T\right)} = H_a^{'}(T) = \frac{2J^{'}T_0^{'2}}{T} - 2J^{'}T_0^{'} = \frac{B}{T} - A \tag{4.11}$$

On the plot $H_a^{'}(T)$vs $1/T$, the domain of validity of equation (4.12) is indicated by a linear dependence. Following the linear regression yields the $J^{'}$ and $T_0^{'}$ parameters.
The form of the equation introduced by Mauro et al. [20] does not allow a similar straightforward linearization procedure. In fact, the application of the derivative procedure to the Mauro et al. equation gives rise to the enthalpy function in the form:

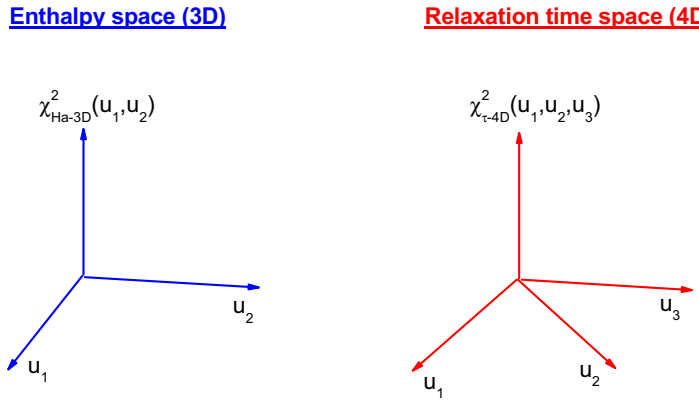

Figure 4.7: *A schematic representation of the figure of merit functions χ^2 which defines the cases of a $(3D)$-space for the enthalpy energy and a $(4D)$-space for the relaxation time. The three-dimensional chi-square space obtained after a derivative transformation of the relaxation time-temperature evolution, defines the enthalpy space which is called $(H_a - 3D)$.*

$$H_a^{'}(T) = \frac{d\ln\tau}{d\left(1/T\right)} = K\left(1+\frac{C}{T}\right)\exp\frac{C}{T} \tag{4.12}$$

Unlike the previous models, the parameters (K, C) are not correlated with the slope and the intercept of a linear function, thus both variables being necessarily and simultaneously involved in the data analysis.

4.1.3.1 $3D$-Enthalpy space. Relative weighted functions

A common characteristic for all glass forming equations describing the variation of the characteristic relaxation time or viscosity is that they are involving three parameters $(u_1 = \tau_0, u_2, u_3)$. Bypassed through the derivative procedure, the numbers of parameters involved are reduced from three to only two, allowing for all of them an enthalpy model function with two variables

$$\tau\left(\tau_0, u_1, u_2\right) \underbrace{\Rightarrow}_{Derivative} H_a\left(u_1, u_2\right) \tag{4.13}$$

The figure of merit functions χ^2 involved in both magnitudes will define for the case of the relaxation time a $(4D)$-space and for the enthalpy energy a $(3D)$- space. ***We define the enthalpy space as the three-dimensional chi-square space, obtained after a derivative transformation of the relaxation time- temperature data, which is called*** $(H_a - 3D)$. The relaxation time space$(\tau - 4D)$ is defined as the four-dimensional chi-square space with the variables introduced in the temperature relaxation time evolution $\tau(T)$. In figure (4.7) a schematic representation is showed.

The derivate analysis has two advantages: (1) the number of parameters involved in the figure of merit χ^2 are reduced from three $(u_1 = \tau_0, u_2, u_3)$ to only two (u_2, u_3), because τ_0 is bypassed through the derivative procedure and, (2) the fitting procedure is optimized by means of the change of the relaxation time space $\chi^2_{\tau-4D}$ to the enthalpy space χ^2_{Ha-3D} .

This procedure is carried out by performing numerical derivates of $\tau(T)$, so for obtaining a reasonable quality result, the temperature step of the experimental relaxation time data needs to be as small as possible. This can be solved performing dielectric measurements with the largest possible number of isotherms corresponding to a temperature step not higher than $2K$. On the other hand, the experimental relaxation time $\tau(T)$ has an experimental error and after performing numerical derivatives, the standard merit function χ^2(defined as the sum-of-squares of the vertical distances of the data from curve model) can take significantly large values and also increase its error. The procedure would be limited and the efficiency would also be questionable. How can we resolve this problem?

Minimization process is most often done by minimizing a standard function of merit χ^2. Points far away from the curve model contribute more to the sum-of-squares whereas points close to the curve model contribute less. This makes sense when experimental scatter is expected, on average, to be the same for the whole set of experimental data. In many experimental situations like the case of numerical derivative data, the average distance (or rather the average absolute value of the distance) of the points from the curve is expected to be higher when the scatter is higher. The points with the larger scatter will have much larger sum-of-squares and thus they will dominate the minimization procedure. Minimizing the sum of the squares of the relative distances restores equal weighting to all points and a relative weighting method should be selected.

Taking into account this consideration and for comparing the quality of the fittings between the $3D$-enthalpy space and the $4D$-relaxation time space, we define the figures of merit for each space as the square average of the relative distance between the experimental data and the enthalpy model function [21], by means of the following equations:

$$\chi^2_{Ha3D} = \frac{1}{N-2}\sum_{i=1}^{N}\left(\frac{1}{H_{mi}}\right)^2\{H_{ei}-H_{mi}\}^2 \tag{4.14}$$

$$\chi^2_{\tau 4D} = \frac{1}{N-3}\sum_{i=1}^{N}\left(\frac{1}{\log_{10}\tau_{mi}}\right)^2\{\log_{10}\tau_i-\log_{10}\tau_{mi}\}^2 \tag{4.15}$$

These equations give rise, for the Mauro equation to the next explicit figures of merit in both spaces

$$\chi^2_{Ha3D}(C,K) = \frac{1}{N-2}\sum_{i=1}^{N}\left(1-\frac{\frac{d\ln\tau_i}{d(1/T_i)}}{K\left(1+\frac{C}{T_i}\right)\exp\left(\frac{C}{T_i}\right)}\right)^2 \tag{4.16}$$

$$\chi^2_{\tau 4D}(\tau_0, C, K) = \frac{1}{N-3}\sum_{i=1}^{N}\left(1 - \frac{\log_{10}\tau_i}{\log_{10}\tau_0 + \frac{K}{\ln(10)T_i}\exp\left(\frac{C}{T_i}\right)}\right)^2 \tag{4.17}$$

It should be noticed that, for the $3D$-enthalpy space, the final fit of $\tau(T)$ requires a final assesment of the τ_0 prefactor.

The equation (4.17) represents a surface $\chi^2_{Ha3D} = f(C, K)$ associated to the $3D$-enthalpy space, that is, the mean square deviation is only dependent on two parameters (C, K) and should provide an easier and more accurate mathematic solution that the one found by means of $\chi^2_{\tau 4D}(\tau_0, C, K)$, for wich the minimization is performed on $\chi^2_{\tau 4D}$, which is a three-parameter dependent function (τ_0, K, C).

4.1.3.2 Minimization process

Consider a set of m-data points $\{(T_1, H_e(T_1)), ...(T_m, H_e(T_m))\}$, where the enthalpy values $H_e(T_i)$ are obtained as a numerical derivative of the experimental relaxation time $\tau(T)$. Associated with these data, an enthalpy model function can be defined as a derivative of the relaxation time model $\tau(T)$. This model curve defines a multivariable function $H_m(T_i, p_k)$, which in addition to the temperature axis variable T_i also depends on n-parameter model $p_k = \{p_1, p_2, ...p_n\}$ with $m \geq n$ (e.g .for the Mauro model $p_k = \{C, K\}$). It is desired to find the vector of parameters which minimize a function of merit defined as the sum of the residuals squares between the experimental enthalpy data (obtained from a derivative procedure) and a model enthalpy function.

The estimates of the model parameters are chosen to minimize a function of merit given by the sum of weighted squared residuals. The optimization method that has been used in this work is iterative, so starting values are required for the parameter search. Careful choice of starting values may be necessary as the parameter estimates may represent a local minimum in the function of merit. As we discussed in the previous paragraph, we can define the following objective function

$$\chi^2_{3DW}(p) = \frac{1}{m-n}\sum_{i=1}^{m}\frac{1}{H_m(T_i, p_k)^2}\{H_e(T_i) - H_m(T_i, p_k)\}^2 \tag{4.18}$$

The minimum value of equation (4.18) occurs when the gradient of $\chi^2_{3DW}(p)$ with respect to the parameters is zero. Since the model contains n -parameters there are n- gradient equations. The task is to find a parameter vector which minimizes the equation (4.18). This can be expressed by:

$$\frac{\partial \chi^2_{3DW}(p)}{\partial p_k} = 0 \tag{4.19}$$

This results in a set of n-non linear equations given by:

$$\sum_{i=1}^{m} H_e(T_i)\frac{\partial H_m(T_i, p_k)}{\partial p_k} = \sum_{i=1}^{m} H_m(T_i, p_k)\frac{\partial H_m(T_i, p_k)}{\partial p_k} \tag{4.20}$$

In a non-linear system, the derivatives are functions of both the independent variable and the parameters, so these gradient equations do not have a closed solution. Instead, initial values must be chosen for the parameters. Then, the parameters are refined iteratively, that is, the values are obtained by successive approximations.

In order to calculate the local minima, we used the Gauss procedure routine [22], where at each iteration the model is linearized by approximation to a first-order Taylor series expansion about the starting parameter constant value p_0, and $H_m(T_i, p_0)$ is expanded in to $n-$dimensional Taylor series. It allows the following equation:

$$\sum_{i=1}^{m} H_e(T_i) \frac{\partial H_m(T_i, p_0)}{\partial p_k} = \sum_{i=1}^{m} \left(\sum_{j=1}^{n} \frac{\partial H_m(T_i, p_0)}{\partial p_j} \triangle p_j \right) \frac{\partial H_m(T_i, p_0)}{\partial p_k} \tag{4.21}$$

The above relationship can be rearranged to the normal equations forming a *nxn* system of linear equations, which are defined by the following transformation as:

$$\sum_{i=1}^{m} H_e(T_i) \frac{\partial H_m(T_i, p_0)}{\partial p_k} = \sum_{j=1}^{n} \left(\sum_{i=1}^{m} \frac{\partial H_m(T_i, p_0)}{\partial p_j} \frac{\partial H_m(T_i, p_0)}{\partial p_k} \right) \triangle p_j \tag{4.22}$$

If we define a parameter constant vector b and an iterative matrix A as follows

$$b_k = \sum_{i=1}^{m} H_e(T_i) \frac{\partial H_m(T_i, p_0)}{\partial p_k} \tag{4.23}$$

$$A_{kj}^{0} = \sum_{i=1}^{m} \frac{\partial H_m(T_i, p_0)}{\partial p_j} \frac{\partial H_m(T_i, p_0)}{\partial p_k} \tag{4.24}$$

the normal equation become in the following matricial equation:

$$A(p_0) \star \triangle p = b(p_0) \tag{4.25}$$

where $\triangle p$ is a parameter constant vector with the parameter changing as element with respect to p_0, and the iterative parameter will be calculated as:

$$p_{(n+1)} = p_n + \left[A_{kj}^{0}(p_n)^{-1} \right] \star b(p_n) \tag{4.26}$$

For obtaining the optimal values of p_k, an iterative calculus routine has been developed. The final parameter p_f, has been calculated by n-iterations, starting at the constant parameter value p_0 until a convergence to the final parameter p_f, where the chi-square function of merit reaches an asymptotic constant value around its absolute minimum.

The second-order partial derivatives of the chi-square function of merit describes the local curvature of the function and contains the characteristics of the local extremes. For many variables, this can be tested by the determinant of its Hessian matrix [23], which is defined as a square matrix of its second-order partial derivatives. For the above chi-square function of merit, the Hessian matrix

is defined by a *nxn* matrix given as:

$$H_{ess}\left(\chi^2_{3DW}\right) = \begin{pmatrix} \frac{\partial^2(\chi^2_{3DW})}{\partial^2 p_1} & \frac{\partial^2(\chi^2_{3DW})}{\partial p_1 \partial p_2} & \cdot & \cdot & \cdot & \frac{\partial^2(\chi^2_{3DW})}{\partial p_1 \partial p_n} \\ \frac{\partial^2(\chi^2_{3DW})}{\partial p_2 \partial p_1} & \frac{\partial^2(\chi^2_{3DW})}{\partial^2 p_2} & \cdot & \cdot & \cdot & \frac{\partial^2(\chi^2_{3DW})}{\partial p_2 \partial p_n} \\ \cdot & \cdot & \cdot & \cdot & \cdot & \cdot \\ \cdot & \cdot & \cdot & \cdot & \cdot & \cdot \\ \cdot & \cdot & \cdot & \cdot & \cdot & \cdot \\ \cdot & \cdot & \cdot & \cdot & \cdot & \cdot \\ \frac{\partial^2(\chi^2_{3DW})}{\partial p_n \partial p_1} & \frac{\partial^2(\chi^2_{3DW})}{\partial p_n \partial p_2} & \cdot & \cdot & \cdot & \frac{\partial^2(\chi^2_{3DW})}{\partial^2 p_n} \end{pmatrix} \tag{4.27}$$

For all iterations, the determinant of the Hessian matrix has been calculated as the product of their eigenvalues. If it is positive, it means that p_k correspond with a chi-square local minimum. Its sign gives a criteria for accepting o refusing the characteristics of a local extreme.
For the case of the 3D-enthalpy space, the above minimization procedure is reduced to a particular quadratic case, where the above relationships can be rearranged to the normal equations forming a $(2x2)$ system of linear equations. For each glass forming system, p_k will be defined as a two-dimensional parameter constant vector which will be written as:

$$p_k = \{p_1, p_2\} = \begin{cases} \{D_T, T_0\}: & VFT \\ \{D, C\}: & Avramov \\ \{T_c, \phi\}: & MCT\ and\ DSM \\ \{J, T_0\}: & Elmatad \\ \{C, K\}: & Mauro \end{cases} \tag{4.28}$$

For the Mauro equation, the parameter vector b_k and the iterative matrix A_{kj} define a bidimensional and a cuadratic matrix, which are reduced to the following particular equations:

$$b_k^{0(Model)} = \left\{ \sum_{i=1}^{m} H_e(T_i) \frac{\partial H_m(T_i, p_0)}{\partial p_1}, \sum_{i=1}^{m} H_e(T_i) \frac{\partial H_m(T_i, p_0)}{\partial p_2} \right\} \tag{4.29}$$

$$A_{kj}^{0(Model)} = \begin{pmatrix} \sum_{i=1}^{m} \left(\frac{\partial H_m(T_i, p_0)}{\partial p_1} \right)^2 & \sum_{i=1}^{m} \frac{\partial H_m(T_i, p_0)}{\partial p_1} \frac{\partial H_m(T_i, p_0)}{\partial p_2} \\ \sum_{i=1}^{m} \frac{\partial H_m(T_i, p_0)}{\partial p_2} \frac{\partial H_m(T_i, p_0)}{\partial p_1} & \sum_{i=1}^{m} \left(\frac{\partial H_m(T_i, p_0)}{\partial p_2} \right)^2 \end{pmatrix} \tag{4.30}$$

In the same way, for the $3D$-enthalpy space the Hessian matrix of the chi-square function of merit will be reduced to a quadratic matrix, given rise to:

$$H_{ess}^{(Model)}\left(\chi_{3DW}^{2}\left(p_0\right)\right)=\left(\begin{array}{cc}\dfrac{\partial^2\left(\chi_{3DW}^{2}\left(p_0\right)\right)}{\partial^2 p_1} & \dfrac{\partial^2\left(\chi_{3DW}^{2}\left(p_0\right)\right)}{\partial p_1 \partial p_2}\cdot \\ \dfrac{\partial^2\left(\chi_{3DW}^{2}\left(p_0\right)\right)}{\partial p_2 \partial p_1} & \dfrac{\partial^2\left(\chi_{3DW}^{2}\left(p_0\right)\right)}{\partial^2 p_2}\end{array}\right) \tag{4.31}$$

In addition to the above Gauss procedure the Newton method [24] is supported. In the Newton method the objetive function of merit is expanded into a n-dimensional Taylor series up to the second order. For the case of models involving an exponential function, the normal equation matrix A_{kj} contains second order derivatives and the calculation effort is higher and then the fitting procedure is more sensitive to numerical inestabilities. The use of the Gauss method for minimizing glass forming model functions can be a good alternative solution.

4.1.4 Minimization process for the Mauro equation

The application of the derivative procedure to the Mauro et al. equation gives rise to the enthalpy function in the form:

$$H_m\left(T,C,K\right)=K\left(1+\frac{C}{T}\right)\exp\frac{C}{T} \tag{4.32}$$

The partial derivatives at a starting point p_0 will be written as the following relationship:

$$\frac{\partial H_m\left(T,p_0\right)}{\partial p_k}=\left\{\begin{array}{ll}\frac{K_0}{T}\left(2+\frac{C_0}{T}\right)\exp\left(\frac{C_0}{T}\right): & k=1 \\ \left(1+\frac{C_0}{T}\right)\exp\left(\frac{C_0}{T}\right): & k=2\end{array}\right. \tag{4.33}$$

If we substitute (4.33) in the relationships (4.23), (4.24) and (4.27), the magnitudes that define the method of minimization such as the parameter vector b_k, the iterative matrix A_{kj} and the Hessian matrix H_{ess} of the chis-quare function of merit χ_{3DW}^2, can be calculated. For all iterative parameters p_n, the local minimum condition of the Mauro hypersurface, must be verified. This condition is satisfied if the determinant sign of the Hessian matrix evaluated in each parameter is positive. On the other hand, the experimental data $\tau\left(T\right)$ obtained for a particular material will allow getting the experimental enthalpy $H_e\left(T\right)$.

In order to carry out the minimization process of the Mauro equation, the following tasks must be performed:

- *Transform the experimental data of $\tau\left(T\right)$ to $H_e\left(T\right)$, by means of the derivative procedure*
- *Select a starting parameter $p_0=\{C_0,K_0\}$ around the miniminum region of the Mauro hipersurface $\chi_{Ha3D}^2\left(C,K\right)$*
- *Calculate the vector b_k^0 and the matrix $A_{kj}^{0(Mauro)}$*

- *Perform the iterations* $p_{(n+1)} = p_n + \left[A_{kj}\,(p_n)^{-1}\right] \star b\,(p_n)$ *from the starting parameter* p_0 *to a final parameter* p_f *where the Mauro hypersurface* $\chi^2_{Ha3D}\left(p_f\right)$ *will converge to an absolute minimum value.*

- *Test the minimium condition*

4.1.4.1 Example result

An example result of the minimization analysis is showed in figure (4.8). The analysis is based on a set of data of the liquid crystal 8*OCB, where the temperature relaxation time evolution $\tau(T)$ is calculated from the measurements of a set of isotherms of the dielectric permittivity loss curve $\varepsilon^{''}(f)$. The measurements were done in a temperature range from $[200K - 400K]$ with an experimental temperature step of $2K$, allowing 184 isotherms.
Figure (4.8) shows the analysis results of the minimization procedure. The left graph shows the temperature evolution of $H_e(T)$ obtained through the derivative procedure of the relaxation time data $\tau(T)$ which is showed in the inset graph as an Arrhenius representation. The starting parameter p_0 is estimated from the Mauro hypersurface $\chi^2_{Ha3D}(C,K)$ dysplayed in the right graph of figure (4.9) which also shows the projection of the $\chi^2_{Ha3D}(C,K)$ hypersurface as a function of K and C parameters of the Mauro equation.
The right figure shows the sequence of iterations which is carried out by the use of the above minimization procedure. After 15 iterations, a convergent asymptotic value of $\chi^2_{Ha3D}(C,K)$ is obtained, giving the following transformation.

$$p_0 = \{C_0 = 45, K_0 = 1105\} \underbrace{\Rightarrow}_{Iterative\ task} p_f = \{C = 48.35, K = 1108.17\} \tag{4.34}$$

The final parameter vector p_f will provide us the optimal values of the independent Mauro constants C and K, which minimize $\chi^2_{Ha3D}(C,K)$. These values will be useful for testing the domain of validity of the Mauro equation which should appear as a linear curve.
To make the linearization process of the equation (4.12) similar to the previous equations, the plot of $\ln\left[H_a/\left(1+\frac{C}{T}\right)\right]$ vs $1/T$ should appear as a linear curve for the domain of validity of the Mauro equation, as it clearly follows rewritting equation (4.32) as:

$$\ln\left[\frac{H_a}{1+\frac{C}{T}}\right] = \ln K + \frac{C}{T} \tag{4.35}$$

which involves in the left side of the equation not only the enthalpy values derived from the experimental data but also the parameter C obtained for the above minimization process.
Figure (4.9) shows the result of the linearization representation for 8*OCB. The experimental enthalpy values are rescaled by the constant C which is correlated with K. Both constants are obtained by the above iterative minimization process. A linear curve for this kind of material appears for

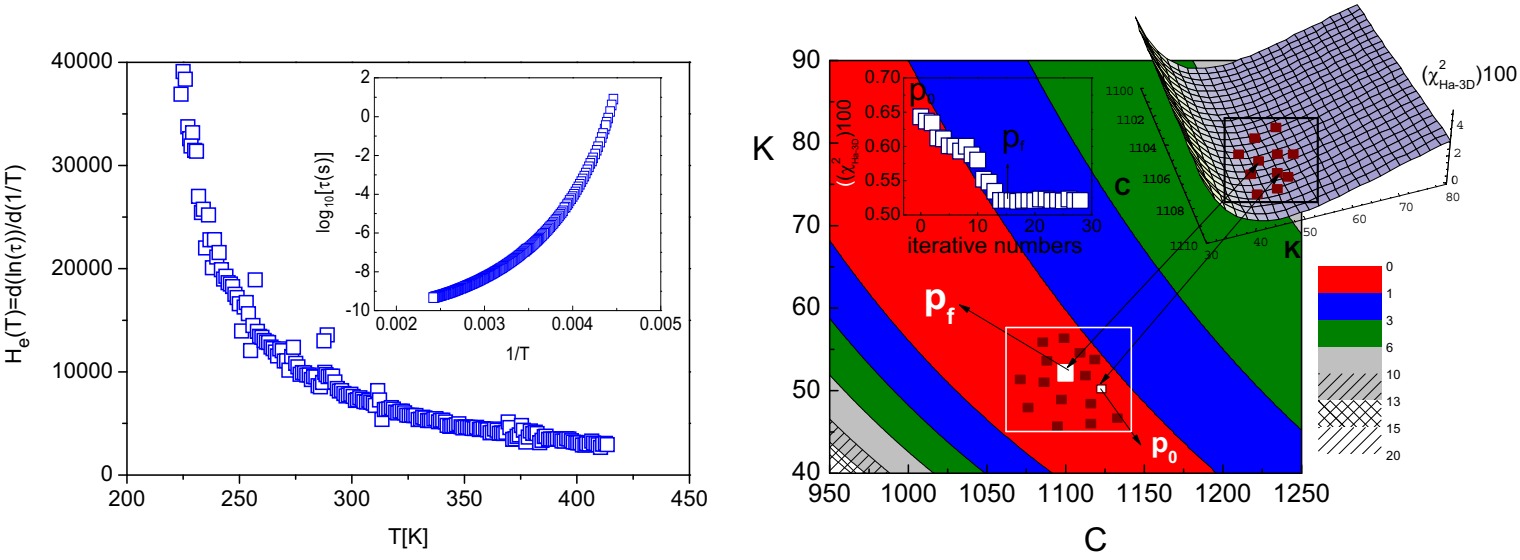

Figure 4.8: *The experimental enthalpy values H_e obtained through the derivative procedure for the case of 8*OCB is shown on the left graph. The right figure shows the projection of the hypersurface $\chi^2_{Ha3D}(C,K)$ as a function of K and C parameters of the Mauro equation for 8*OCB. The values of the minimum found from 3D−enthalpy space minimization procedure, fall in to the smooth and soft valley of the minimal region of χ^2. The red denotes the minimum values of χ^2_{Ha3D}. On the right and left upper corners, the corresponding 3D-space (C,K,χ^2) and the convergence iterations graph are shown, respectively.*

almost the whole temperature domain (small deviations are observed at low temperature), which reinforces the validity of the Mauro equation in this case.

Unlike the previous models, the parameters (K,C) are not correlated with the slope and the intercept of a linear function, thus both variables being necessarily and simultaneously involved in the data analysis. It is clear that minimization procedure within the enthalpy $3D$-space is required for the Mauro equation.

4.1.4.2 Error comparison

The above figures of merit χ^2 were defined by the numerical experimental enthalpy H_e and the enthalpy model function H_m [21]. Both kinds of enthalpy will have an intrinsic absolute error contribution which will appear from the experiment ΔH_e and for the model ΔH_m, giving rise to an absolute error contribution to the figure of merit χ^2. These contributions can be estimated by the calculus of their differential function

$$\Delta\chi^2_{3D}(p) \backsimeq d\chi^2_{3D}(T,p) = \frac{\partial\chi^2_{3D}(T,p)}{\partial H_e(T)}\triangle H_e(T) + \frac{\partial\chi^2_{3D}(T,p)}{\partial H_m(T,p)}\triangle H_m(T,p) \tag{4.36}$$

The error source which corresponds to the enthalpy model H_m can be estimated by the same way, and thus it can be written as:

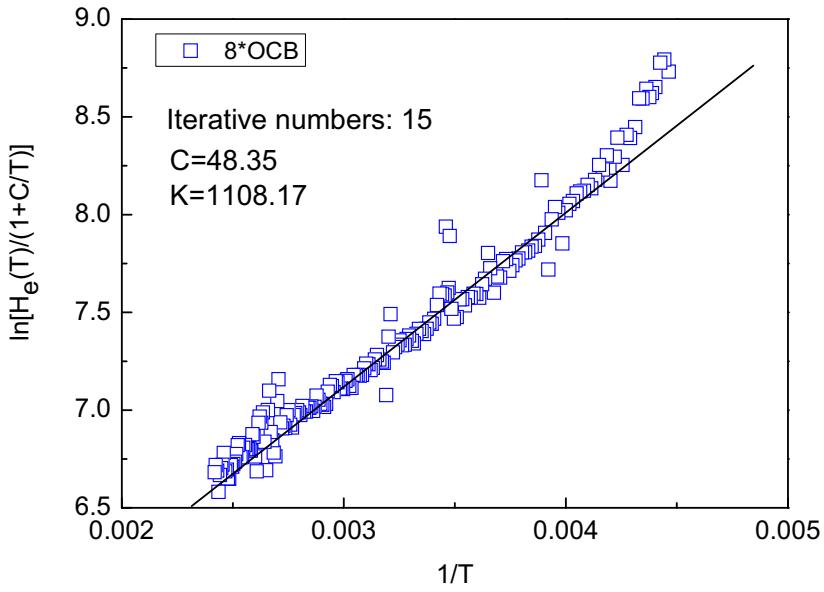

Figure 4.9: *Mauro et al. equation focused linearized distortion-sensitive analysis in the activation enthalpy space based on equation. (4.36) (continuous line). The domain of its validity should follow a linear dependence.*

$$dH_m(T,C,K) = \left\{\left(1+\frac{C}{T}\right)\exp\left(\frac{C}{T}\right)\right\}\triangle K + \left\{\frac{K}{T}\left(2+\frac{C}{T}\right)\exp\left(\frac{C}{T}\right)\right\}\triangle C \tag{4.37}$$

where T is the temperature and $\triangle C$ and $\triangle K$ are the absolute errors of the determined Mauro constants.

On the other hand, the relaxation time τ, obtained by the dielectric experiment, has an error contribution $\triangle\tau(s)$, which through the derivative procedure, will provide us the experimental enthalpy error source $\triangle H_e$. Taking into accout the equation (4.36) the absolute error can be estimated by:

$$dH_e(T) = \frac{\partial H_e(T)}{\partial T}\Delta T = \frac{\partial\left(d\ln(\tau(s))/d\left(\frac{1}{T}\right)\right)}{\partial T}\Delta T \backsimeq 2\frac{T}{\tau(s)}\triangle\tau(s) \tag{4.38}$$

The above equations give us a way to calculate the contributions of experimental error and those that will appear as a result of numerical derivative. Both sources of errors will have an important role in the absolute error of the function of merit which is used to solve this problem.

To what extent will be affected a standard χ^2_{3D} (defining the standard function as the sum-of-squares of the vertical distances between the experimental enthalpy data and the enthalpy curve model) and a relative weighted function of merit χ^2_{3DW} (defined as the equation (4.18)) for such error contributions? Will the consideration of introducing a relative weighted function minimize the error problem?

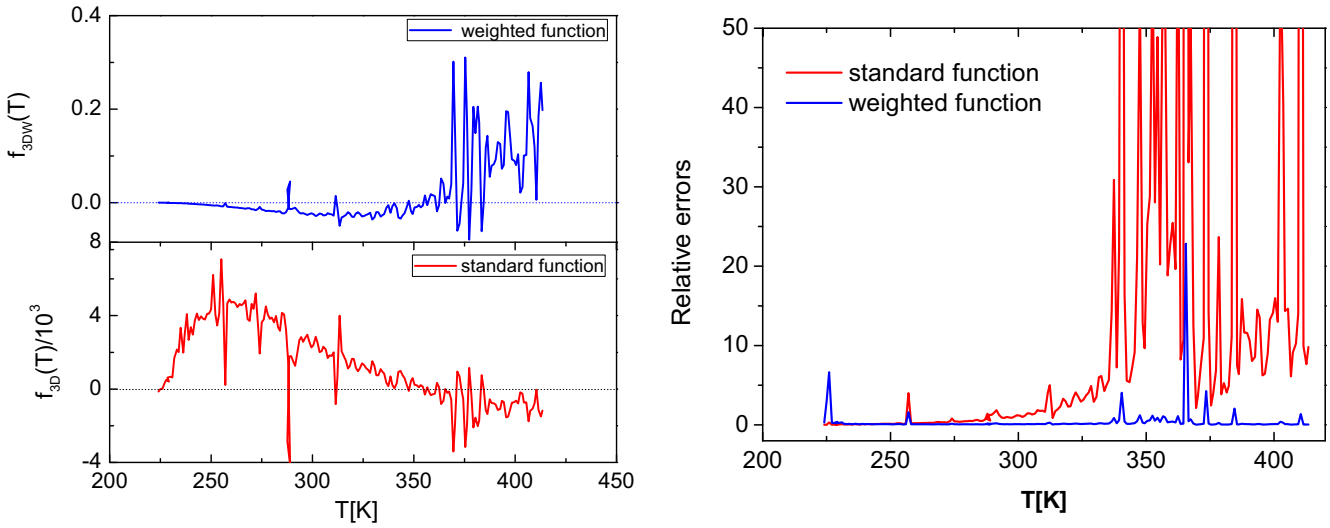

Figure 4.10: *Temperature dependencies of the absolute and local relative errors functions for the case of 8*OCB. The blue and red colours denote the cases of the standard χ^2_{3D} and the case of a weighted χ^2_{3DW} function of merit.*

The substitution of the equations (4.38) and (4.37) in (4.36) allows a way for estimating the absolute error of both figures of merit, which will be defined by the following equations:

- For a weighted function

$$d\chi^2_{3DW}(p) = \frac{2}{m-2}\sum_{i=1}^{m} f_{3DW}(T_i, p) \tag{4.39}$$

$$f_{3DW}(T,p) = \left\{\frac{H_e(T)}{H_m(T,p)} - 1\right\}\left\{\frac{\triangle H_e(T)H_m(T,p) - \triangle H_m(T,p)H_e(T)}{H_m(T,p)^2}\right\} \tag{4.40}$$

- For a standard function

$$d\chi^2_{3D}(p) = \frac{2}{m-2}\sum_{i=1}^{m} f_{3D}(T_i, p) \tag{4.41}$$

$$f_{3D}(T,p) = \{H_e(T,p) - H_m(T)\}\{\triangle H_e(T,p) - \triangle H_m(T)\} \tag{4.42}$$

where the functions $f_{3D}(T)$ and $f_{3DW}(T)$ may be defined as local functions of temperature, and its average value will give us the absolute errors of the function of merit.
Large or small values of these functions do not provide a complete answer for testing which of both would be less affected by the error sources instead, we need to know how big or small the absolute errors compared to both function of merit are. The comparison of their relative errors will allow us to select the most optimal function for the minimization process. Taking into account the above equations we can define their local relative errors as:

- For a weighted function

$$e^{(i)}_{3DW}(T,p) = \frac{f_{3DW}(T,p)}{\left(\frac{H_e(T)}{H_m(T,p)} - 1\right)^2} = \frac{\triangle H_m(T,p)\,H_e(T) - \triangle H_e(T)\,H_m(T,p)}{H_m(T,p)\,H_e(T) - H_m(T,p)^2} \tag{4.43}$$

- For a standard function

$$e^{(i)}_{3D}(T,p) = \frac{f_{3D}(T,p)}{(H_e(T) - H_m(T,p))^2} = \frac{\triangle H_e(T) - \triangle H_m(T,p)}{H_e(T) - H_m(T,p)} \tag{4.44}$$

The above absolute and relative error equations depend on the evolution of the relaxation time with temperature, which is obtained from the experiment for each material. In order to implement a quantitative comparison, the calculation of the above equations have been performed for the case of 8*OCB. Figure (4.10) shows the results of the comparison which optimize both functions of merit. The graphs show the temperature dependences of the local functions which define the absolute and relative errors respectively.

By using the experimental data of the 8*OCB material, we can conclude that, for the case of the use of a standard function of merit, the absolute and the relative errors will take values much higher than for the case of a weighted function. This procedure has been also tested for all materials dealt with in this work. This results in the conclusion that the use of a relative weighted function of merit minimizes the sources of errors and that the use of a relative weihgted function will be more advantageous to implement minimization processes.

Bibliography

[1] F. Kremer, A. Schoenhals, (eds.). *Broadband Dielectric Spectroscopy*, (Springer Verlag, Berlin, 2003).

[2] J. C. Martinez-Garcia et al, J. Phys. Chem. B **114**, 6099, (2010).

[3] http://www.novocontrol.de.

[4] S. Arrhenius, Z. Phys. Chem **4**, 226, (1889).

[5] T. Hecksher, A. I. Nielsen, N. B. Olsen, J. C. Dyre, Nature Physics **4**, 737, (2008).

[6] E. Donth, The Glass Transition. *Relaxation Dynamics in Liquids and Disordered Material*, Springer Series in Material Sci. II, Vol. 48 (Springer Verlag, Berlin, 1998).

[7] P. G. Debenedetti, F. H. Stillinger, Nature **410**, 259, (2001).

[8] S. A. Kivelson, G. Tarjus, Nature Materials **7**, 831, (2008).

[9] G. B. McKenna, Nature Physics **4**, 672, (2008).

[10] J. Mattsson, H. M. Wyss, A. Fernandez-Nieves, K. Miyazaki, Z. Hu, D. R. Reichman, D. A. Weitz, Nature **462**, 83, (2009).

[11] L. O. Hedges, R. L. Jack, J. P. Garrahan, D. Chandler, Science **323**, 1309, (2009).

[12] H. Vogel, Phys. Z **22**, 645, (1921).

[13] G. S. Fulcher, J. Am. Ceram Soc **8,** 339, (1925).

[14] G. Tammann, W. Hesse, Z. Anorg. Allg. Chem **156**, 245, (1926).

[15] A. Drozd-Rzoska, S. J. Rzoska, Phys. Rev.E **73**, 041502, (2006).

[16] C. Hansen, F. Stickel, P. Berger, R. Richert, E. W. Fischer, J. Chem. Phys **107,** 1086, (1997).

[17] A. Drozd-Rzoska, S. J. Rzoska, C. M. Roland, J. Phys.: Condens. Matt **20**, 244103, (2008).

[18] W. Goetze, L. Sjoegren, Rep. Prog. Phys **55**, 241, (1992).

[19] Y. S. Elmatad, D. Chandler, J. P. Garrahan, J. Phys. Chem. B **113**, 5563, (2009).

[20] J. C. Mauro, Y. Yue, A. J. Ellison, P. K. Gupta, D. C. Allan, PNAS **106**, 19780, (2009).

[21] J. C. Martinez-Garcia, J. Ll. Tamarit, S. J. Rzoska. J. Phys. Chem **134**, 024512, (2011).

[22] R. Fletcher, *Practical methods of optimization* (2nd ed.).(New York: John Wiley & Sons. ISBN 978-0-471-91547-8 ,1987)

[23] I. S. Gradshteyn, I. M. Ryzhik, *Hessian Determinants*.(San Diego, CA: Academic Press, p. 1069, 2000).

[24] J. Nocedal, Wright. Stephen. *Numerical optimization*.(New York: Springer. ISBN 0387987932, 1999).

Chapter 5

Results and discussion

In this chapter we focus on the principal results obtained in this work. We present the results divided in two topics. In the first section we present the results concerning to the dynamic of the pure compounds and mixed crystals formed between cycloheptanol (C7-ol) and cyclooctanol (C8-ol) as well as the α-relaxation dynamics of cyanoadamtane (CNadm) and its mixtures with chloroadamantane (Cladm). In the second part the results are showed in two groups (linearized and non-linearized models). The application of the derivative based, distortion-sensitive analysis to LCs and ODICs materials are presented. The possible empirical correlations between the linearized model with the universal pattern for the high frequency wing of the loss curve for primary relaxation time for LCs and ODICs are also presented. In the last part we show the application of the minimization procedure previously discussed in Chapter 4 to 30 glass forming systems. The evidences of the existence of crossovers as well as a quantitative description are discussed. A new procedure for detecting the crossover in a very easy way is showed.

5.1 Dynamics in binary systems.

5.1.1 Binary system C8-ol-C7-ol

The dynamics of the pure compounds and mixed crystals formed between C7-ol and C8-ol have been studied by means of broadband dielectric spectroscopy at temperatures near and above the orientational glass transition temperature. Dielectric loss spectra in the orientationally disordered simple cubic phase are presented. We have performed a detailed analysis of the dielectric loss spectra showing clear evidence of the relaxation processes for the orientational glass-former pure compounds.

The results focus on the issue of the appearance of the secondary relaxations for the OD $(C7-ol)_{1-x}(C8-ol)_x$ mixed crystals and try to make clear if they are concomitant with those found for pure components or, on the contrary, a change of the effects of many-molecule dynamics and intermolecular coupling or a change in the hydrogen bonding scheme can induce their

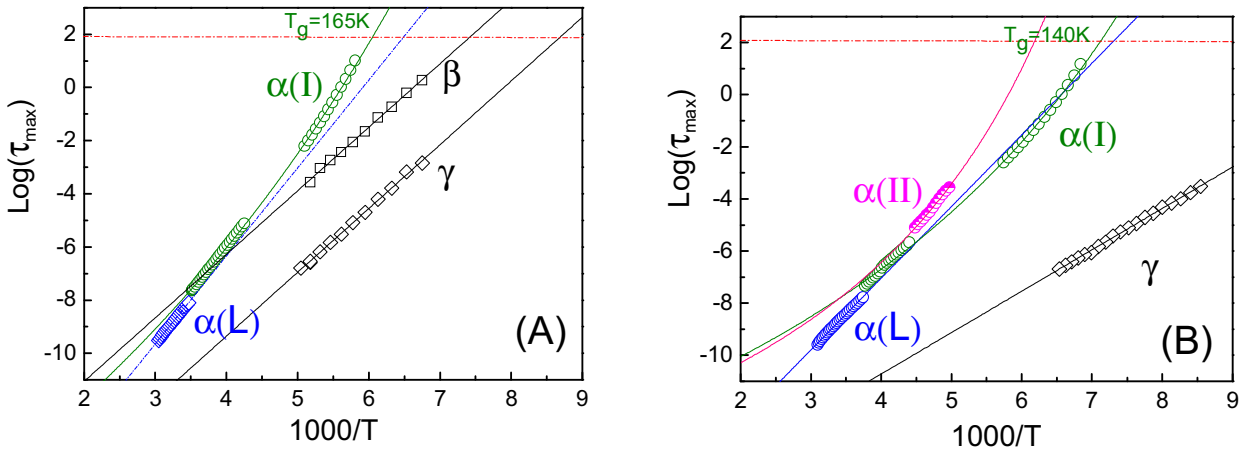

Figure 5.1: *Arrhenius plots of the dielectric relaxation times of pure components (C8-ol, (A); C7-ol, (B) for the α- (circles), β- (squares) and γ- (diamonds) relaxation processes. α-relaxation times for the different phases are denoted by colors: blue, liquid phase; green, phase I, and magenta for phase II of C7-ol.*

disappearance, as claimed for the β-relaxation in a preceding work [1].

5.1.1.1 Dynamics of OD phases of pure compounds

Figure (5.1) shows the relaxation times for the different processes vs. reciprocal of temperature (Arrhenius plot). As for the α-relaxation, and with the exception of the liquid phases, it clearly exhibits distinct non-Arrhenius behavior and thus the empirical Vogel-Fulcher-Tammann (VFT) function was used [2]. This function can be written as:

$$\tau = \tau_0 \exp\left[\frac{DT_0}{T - T_0}\right] \tag{5.1}$$

where τ_0 is a prefactor of the order of the molecular vibrations, T_0 is the temperature associated with the estimation of the ideal glass transition and D (strength parameter) is a measure of the fragility for the given temperature domain. Within the frame of the strong-fragile classification by Angell [3] the high values of D classify the OGs obtained from phases I of C8-ol and C7-ol as strong glasses (see Table 5.1). It should be noted the relaxation times for phases I are not available for the whole temperature range, due to the irreversible transition to phases II for both cases, as previously stated in previous works [4-7].

As far as the β-relaxation of C8-ol is concerned, it is worth noting that the characteristic time difference from the α process increases upon decreasing temperature, enabling the β-relaxation times to be unambiguously determined in the low temperature range. On the contrary, the γ-relaxation times for both C8-ol and C7-ol glass formers are quite enough far away from the preceding (α and β) processes. For all the secondary processes the relaxation times against temperature follow an Arrhenius law as evidenced in Figure (5.1). The fitted parameters are summarized in Table (5.2).

5.1.1.2 Dynamics of OD phase I of mixed crystals

It has been reported that C7-ol and C8-ol mixtures form continuous simple cubic (sc) OD mixed crystals $(C7-ol)_{1-x}(C8-ol)_x$ for the whole composition range [8]. The OD phase for such mixed crystals does not transform into a crystalline phase at low temperatures and thus OGs are easily obtained on cooling. Figure (5.2) displays the melting phase diagram together with the variation of the glass transition temperature as a function of the mole fraction [8]. Recently, the dynamics of the OD mixed crystals was analyzed for a set of concentrations, nicely reinforcing the isomorphic relationship between the OD phase I of pure components [1].

The number of dynamics studies on OD phases is relatively limited due to experimental problems in finding systems which give easily rise to glass formers (OGs) avoiding the irreversible transition to the low-temperature more ordered phase, as it has been shown for C8-ol and C7-ol OD phases I [9,10]. Fortunately, this inconvenience does not appear for the OD mixed crystals phase I sharing C8-ol and C7-ol for the whole composition range, owing to the isomorphism relationship between that phase of pure components and the appearance of the OG state. Thermodynamic and structural properties of the mixed crystals were previously studied with detail [8]

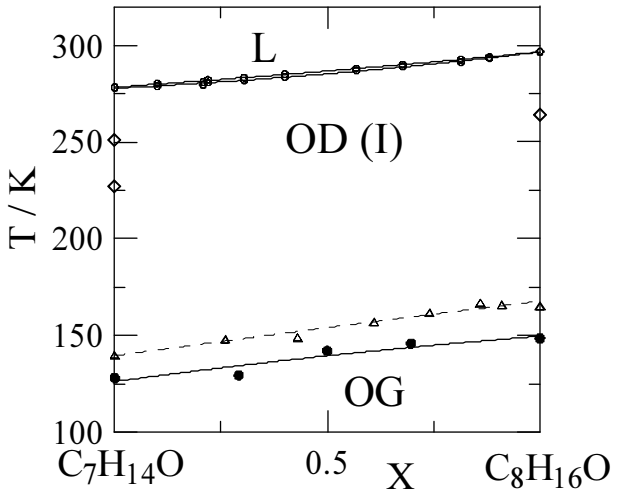

Figure 5.2: *Equilibrium melting phase diagram (L+OD(I)) (empty circles) and orientational glass transition temperatures obtained from X-ray diffraction [8](full circles) and from dielectric spectroscopy (empty triangles).*

Figure (5.3) depicts the α-relaxation times as a function of the reciprocal of temperature for the whole set of studied mixed crystals together with those of pure compounds for the sc OD phase I. It clearly evidences the continuous change of the relaxation time as a function of the mole fraction, supporting the conjecture that isomorphism between phases I of C7-ol and C8-ol involves also the dynamic behavior.
The relaxation times obtained for the different processes as a function of temperature and for the set of studied mixed crystals are plotted in figure (5.4). It should be noted that the non-Arrhenius behavior for the α-relaxation and the Arrhenius behavior for the β- and γ-relaxations exhibited by the pure compounds remain for the mixed crystals.

5.1.1.3 Disentangling the β-relaxation

The evidence of the secondary relaxations strongly depends on the mole fraction and on the temperature domain. As far as the γ-relaxation, it clearly appears for the whole temperature range

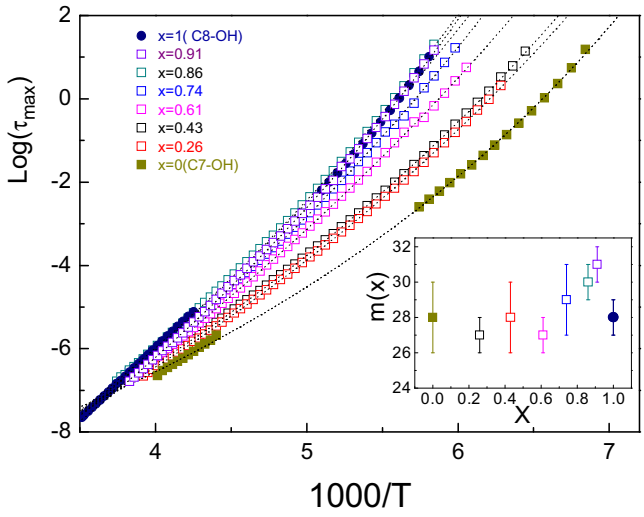

Figure 5.3: *α-relaxation time as a function of the reciprocal of temperature for the C7-ol and C8-ol pure compounds and mixed crystals. Dotted lines correspond to the VFT fits according to equation (5.1). Inset displays the fragility index as a function of the mole fraction.*

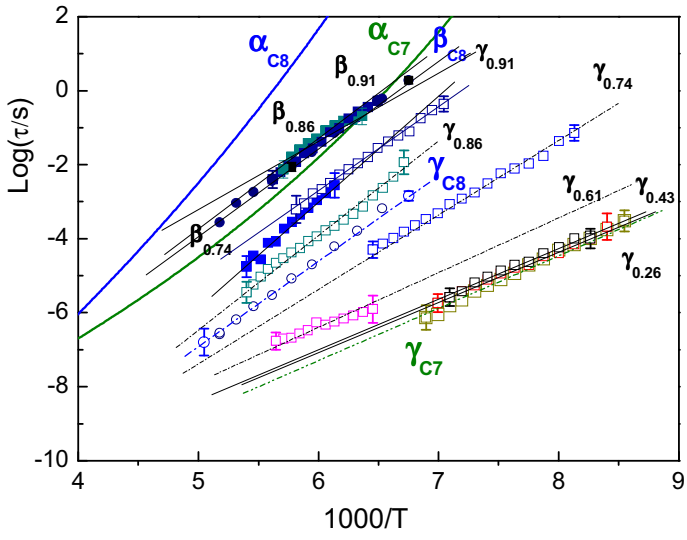

Figure 5.4: *Arrhenius plot of the β- (full symbols) and γ- (empty symbols) relaxation times as a function of the inverse of temperature for the set of analyzed mixed crystals (mole fraction is given as a subindex for each relaxation process and symbols are as in Figure (5.3)). The α-relaxation times are given only for pure components as a guide for the eyes C8-ol, blue continuous line, and C7-ol, green continuous line).*

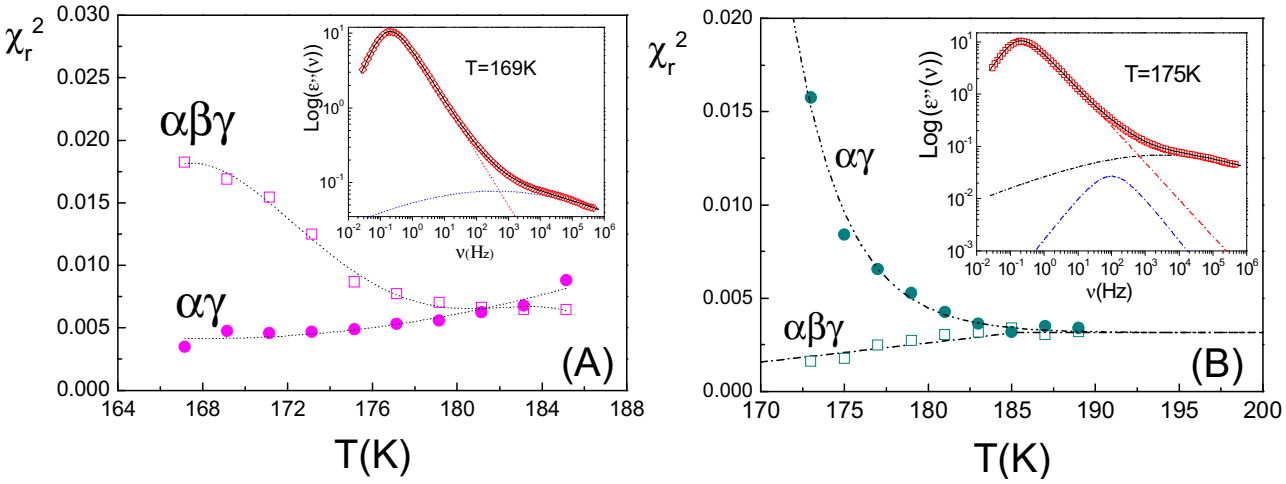

Figure 5.5: *Function of merit obtained from the fits of dielectric loss spectra for $x = 0.61$(A) and $x = 0.86$(B) by assuming the existence of one $(\alpha\gamma)$ or two $(\alpha\beta\gamma)$ secondary relaxations in addition to the primary α-relaxation. Insets display an example in the low-temperature domain for each composition.*

(within the ubiquitous limit of the available frequency domain). Nevertheless, β-relaxation could be disentangled only for mole fractions with $x \geq 0.74$, while for smaller mole fractions the applied fitting procedure gave better results for the whole temperature range when only two processes(α and γ) instead of three (α,β and γ) were hypothesized.

For $(C7-ol)_{1-x}(C8-ol)_x$OD mixed crystals the dielectric loss spectra were fitted by assuming the existence of the ubiquitous α-relaxation process (at $T > T_g$) and one or two secondary processes in order to disentangle their existence by means of the function of merit χ_r^2 defined as:

$$\chi_r^2 = \frac{1}{n-m}\sum_{i=1}^{n}\left(Y_i^{exp} - Y_i^{mod}\right)^2 \tag{5.2}$$

where n is the number of experimental points, Y_i^{exp} are the experimental values, Y_i^{mod} are the values obtained by the fitted model, m is the number of fitted parameters and thus, $n-m$ is the number of degrees of freedom.

Figure (5.5) displays the results for $x = 0.61$ (A) and $x = 0.86$ (B). For the low-temperature range of the mixed crystal with $x = 0.61$ the data analysis reveals that the introduction of an additional third relaxation process is completely fictitious and thus that only α- and γ-relaxation processes are present. On the contrary, for mixed crystals with $x \geq 0.74$ the presence of the three relaxation processes clearly improves the description of the experimental data.

5.1.1.4 Discussion

The results of Figure (5.3) would imply that the dynamics of the α-relaxation (meanly dominated by the hydrogen-bonded scheme) continuously changes from $x = 0$ (C7-ol) to $x = 1$ (C8-ol) without a noticeable change of the fragility (see inset in Figure (5.3)). As a consequence, the secondary

Table 5.1: *Characteristic parameters of the α-relaxation process according to the VFT fits.*

X	T_0 / K	D	$\log[\tau_o / s]$	m	T_g / K
0	68±2	36±1	-(12.49±0.76)	28±2	140±1
0.26	65±2	47±2	-(13.80±0.97)	27±1	148±2
0.43	66±1	44±2	-(13.32±0.87)	28±2	149±2
0.61	57±2	68±2	-(15.04±0.94)	27±1	157±2
0.74	70±2	51±1	-(14.64±0.73)	29±2	162±2
0.86	73±2	50±2	-(14.95±0.89)	30±1	167±1
0.91	72±1	51±2	-(15.67±0.82)	31±1	166±1
1	58±2	77±2	-(16.14±0.82)	28±1	165±2

relaxations coming from the change of the dipole orientation due to the set of active conformations in pure components should also appear in mixed crystals. Figure (5.4) displays the relaxation time for the β and γ secondary relaxations. As for the β-relaxation times as a function of the mole fraction (for the range they could be determined, $0.74 \leq x \leq 1$) it can be seen from the figure that whatever the mole fraction relaxation times for a given temperature are very close to that of pure C8-ol. It is worth noting that β-relaxation was attributed to the ring conformations of C8-ol and, according to the results here obtained it clearly appears that relaxation time is almost the same for the molecular mixed crystals (till $x \approx 0.74$). Such a result reinforces the intramolecular character of this relaxation process [4,7].

As far as the γ-relaxation is concerned, assigned to the –OH axial and equatorial conformations (thus intrinsically related to the hydrogen-bond scheme), clearly shifts to higher frequencies with decreasing mole fraction at a given temperature. This process shows up for all the mole fractions (see figure (5.5)) rather clearly shifting to higher frequencies with increasing temperature as a thermally activated process (figure (5.4)). Nevertheless, it should be notice that, although the α-relaxation for C7-ol is faster than for C8-ol (see figure (5.4)), for high mole fractions of C8-ol ($X = 0.91$, 0.86) the dynamics of the γ process is slightly slower than for pure compound C8-ol, while for mole fractions lower than $x = 0.86$ γ-relaxation times fall into those corresponding to the pure components at a given temperature. We have not, at present, a clear explanation for such a detail, but it is obvious that such an effect should come from a special molecular short-range order in the hydrogen-bond map for this composition range and not from a possible confusion with the β-relaxation process, which for such a composition domain is clearly seen as an intermediate dynamical process between the mean α-relaxation and the fastest γ-relaxation. Table (5.2) gathers the experimental parameters of the thermally activated secondaries processes.

Table 5.2: *Experimental parameters of the thermally activated ($\tau = \tau_0 \exp[E_a/RT]$) β- and γ-relaxation processes.* [a] *Values from [7].*

	β-relaxation		γ-relaxation	
X	$E_a^{\exp}/eV$	$\log[\tau_o/s]$	$E_a^{\exp}/eV$	$\log(\tau_\infty)$
0			0.32±0.06	-(17.07±0.24)
0.26			0.28±0.05	-(15.72±0.17)
0.43			0.26±0.09	-(14.96±0.21)
0.61			0.36±0.07	-(17.24±0.34)
0.74	0.55±0.08	-(19.74±0.73)	0.37±0.08	-(16.26±0.39)
0.86	0.50±0.07	-(16.49±0.69)	0.45±0.04	-(15.54±0.33)
0.91	0.48±0.08	-(16.09±0.48)	0.46±0.05	-(16.79±0.26)
1	0.47±0.07	-(15.84±0.22)	0.47±0.02	-(18.09±0.616)
	(0.51)[a]	(-16.74)[a]	(0.47)[a]	(-18.5)[a]

Results confirm those reported in earlier reports for the primary α- and intramolecular in nature secondary β- and γ- relaxations for C8-ol and α- and γ- relaxations for C7-ol [1,7,11-13]. Thus, for mixed crystals, in addition to the inherent primary α-relaxation due to the freezing in the orientational disorder, it has been possible to disentangle the secondary relaxations.

5.1.2 Binary system CNadm-Cladm

The α-relaxation dynamics of cyanoadamantane (CNadm) and its mixtures with chloroadamantane (Cladm) has been studied by means of broadband dielectric spectroscopy. The existence of orientationally disordered (OD) face centered cubic mixed crystals $(Cladm)_{1-x}(CNadm)_x$ for $0.5 \leq x \leq 1$ has been put in evidence by thermodynamics and structural analyses.

5.1.2.1 Dynamic of OD phases of Pure compounds

Figure (5.6) shows the dielectric loss spectra of CNadm for various selected temperatures on cooling from room temperature obtained in this work. For all the studied temperatures, a single peak is observed, although the half-width clearly exceeds the monodispersive Debye relaxation process. Since the loss peaks of the α-relaxation of the dielectric permittivity also exhibits an asymmetric broadening they were fitted according to the empirical Havriliak-Negami equation. For temperatures lower that $235K$, the dielectric strength diminishes due to the onset of an antiferroelectric arrangement of molecular dipoles as we will see through the analysis of the Kirkwood factor. As for the latter, it has been recently argued that the glass transition for CNadm is strongly related with the freezing of fluctuations of an antiferroelectric local ordering which gives rise to a diminution of the permittivity strength at temperatures on approaching the glass transition, an effect that was already postulated in the pioneering work of Amoreux et. al. [16].

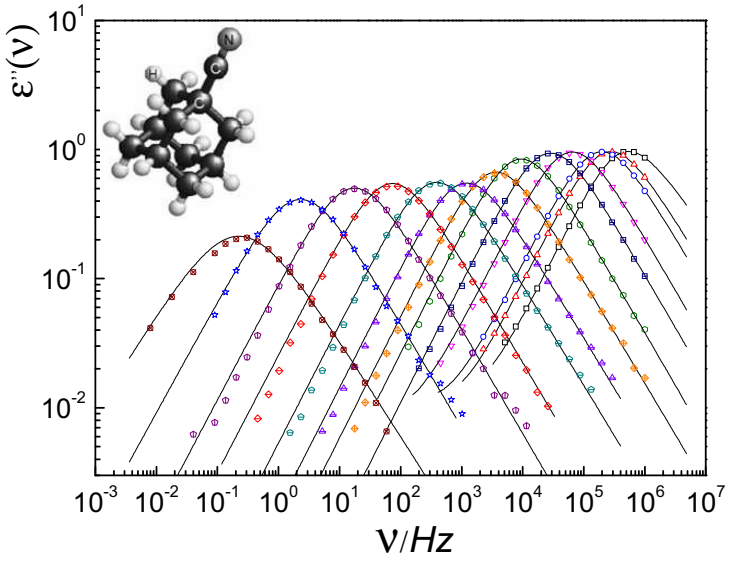

Figure 5.6: *Double logarithmic representation of selected dielectric loss spectra of CNadm from* 293*K to* 173*K (measurements were performed every* 5*K, but we show only one over two for clarity). The lines show the fits using the HN function for the* α*-relaxation processes. Inset shows the molecular structure on CNadm.*

5.1.2.2 Dynamics of mixed crystals

In order to analyze the influence on the dynamics of the molecular substitution in the CNadm OD lattice of similar dipolar molecules Cladm, OD mixed crystals between both compounds have been studied.

The formation of OD mixed crystals (solid solutions of substitutional type) was studied in the concentration range $0.5 \leq x \leq 1$ and controlled by means differential thermal analysis and high-resolution X-ray powder diffraction. As for the former, for compositions with mole fraction higher than 0.5, only one melting peak was found, which means that the OD phase of the mixed crystals does not transform to a more ordered structure.

OD mixed crystals were also characterised by means of dielectric spectroscopy. Selected dielectric loss spectra corresponding to the $(Cladm)_{0.38}\,(CNadm)_{0.62}$ mixed crystal are presented in figure (5.7), showing the α-relaxation process. Neither the pure CNadm compound nor the mixtures present an excess wing or a secondary peak in the frequency and temperature range of interest for this work.

Due to the cooperative character of the α-relaxation process, there is no doubt that molecules of both types participate together into the same α-relaxation process. Thus, an unique Havriliak-Negami equation was used to account for the dielectric losses. From that, the relaxation time of the maximum of the loss peak for each composition as a function of temperature was obtained: they are plotted in the Arrhenius diagram of Figure (5.8). A first and overall inspection of Figure

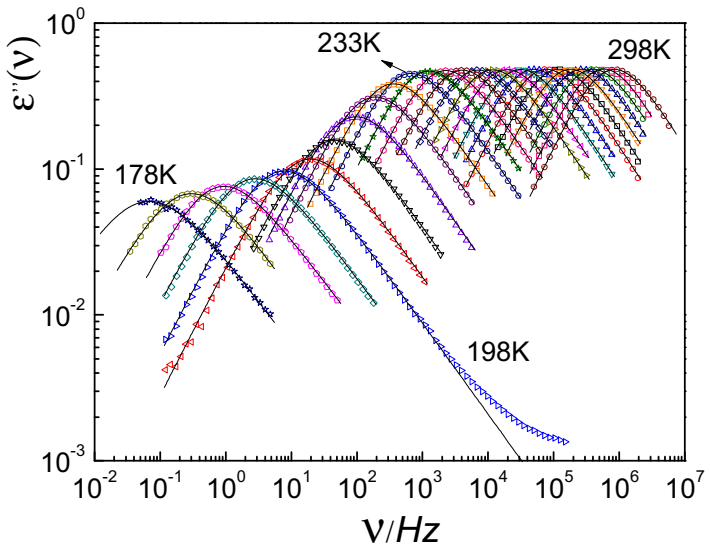

Figure 5.7: *Double logarithmic representation of selected dielectric loss spectra of* $(Cladm)_{0.38}(CNadm)_{0.62}$ *mixed crystal in the OD fcc phase at various temperatures. Solid curves are the HN fitting function. The dielectric loss at* $T = 198K$ *is shown for the whole frequency range to highlight the existence of an excess wing.*

(5.8) seems to indicate that for mole fractions higher than 0.5, at a given temperature, the dynamics is slowed down when molecules of CNadm are substituted by those of Cladm, i.e. with decreasing the mole fraction x of CNadm. This is, at least, a very surprising phenomenon when dynamics of pure compounds is recalled, because for the OD phase of Cladm dynamics concerning the overall molecular tumbling is several orders of magnitude faster than that of the CNadm at the same temperature [17].

5.1.2.3 Shape paramters

The Havriliak-Negami shape parameters α_{HN} and β_{HN} of the α-relaxation have been determined from the fit of HN function. As far as β_{HN} parameter is concerned, it is almost temperature independent but strongly dependent on composition of the mixed crystal. Such a behavior can be directly seen of figure (5.9), in which the values of the product $(\alpha_{HN}\beta_{HN})$ are represented in the abscise axis. Approaching the glass transition temperature, the common feature of many glass-forming materials, i.e. a decrease of the shape parameters with temperature, is found, indicating the strong deviation from the Debye behavior commonly attributed to the increase of temporal and spatial heterogeneities.

Experimental dielectric spectra, obtained in the frequency domain, were transformed to the time domain by means of the use of the connection between dielectric permittivity and relaxation function via the Laplace transformation and β_{KWW} stretched parameter was directly fitted for each temperature and mole fraction. Figure (5.9) shows the relationship between such a fit parameter

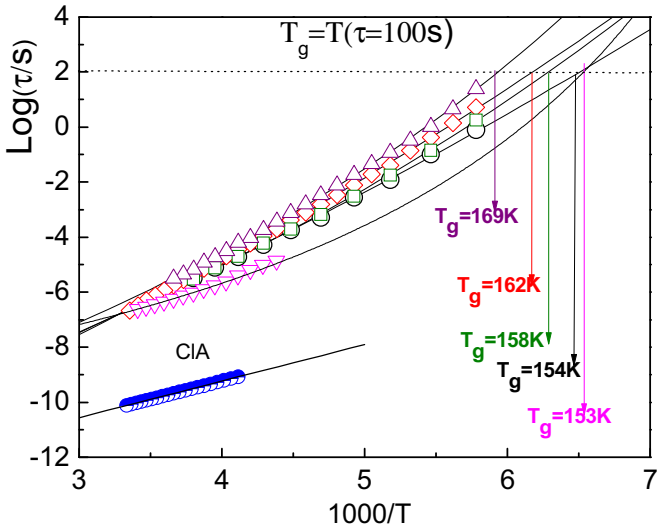

Figure 5.8: *Arrhenius plot of the -relaxation time versus inverse temperature for the pure compound CNA (black circles) and various* $(Cladm)_{1-x}(CNadm)_x$ *mixed crystals, X=0.80 (red diamonds), X=0.69 (green squares), X=0.62 (violet triangles) and X=0.5 (pink inverted triangles). Values for Cladm (blue circles) were calculated according to the data provided by Amoureux et. al. [17].*

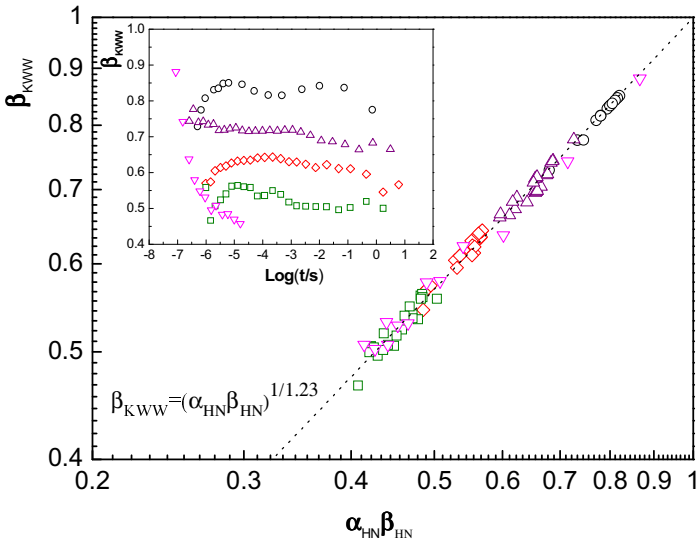

Figure 5.9: *Double logarithmic scale for the* β_{KWW} *stretched exponent of the Kohlrausch-Williams-Watts (KWW) relaxation function as a function of the shape parameters for the mixed crystals* $(Cladm)_{1-x}(CNadm)_x$*. Dashed line corresponds to the relationship between*β_{KWW} *and* α_{HN} *and* β_{HN} *shape parameters provided by Alegria et al. [15]. Simbols are the same as in Figure (5.8) .*

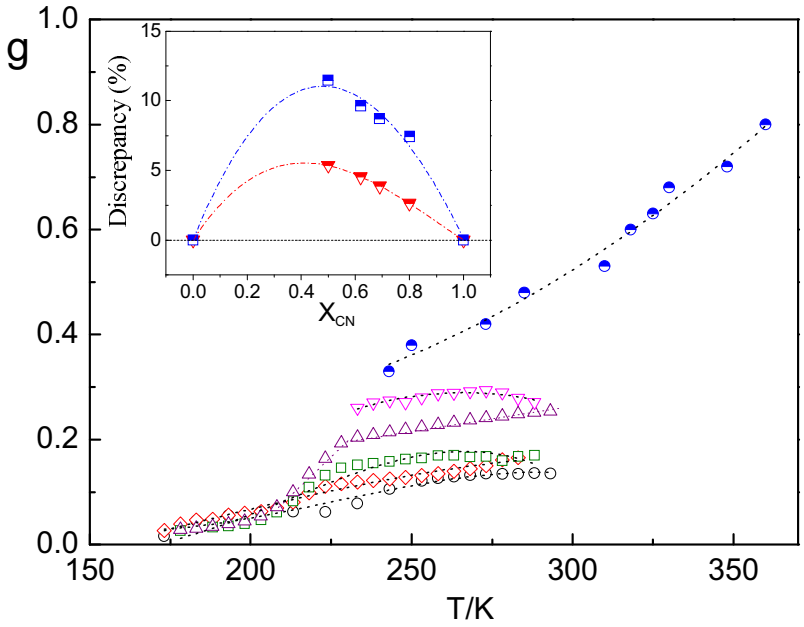

Figure 5.10: *Kirkwood factor as a function of temperature for several mole fractions (symbols as in Figure 5.8). Values for Cladm (blue circles) were obtained from Amoureux et al.[17]. The inset shows the relative deviation from the calculation of g used in the main plot from the values obtained according two other procedures described in references [26] and [27](Color online).*

and those obtained from the fits of the HN equation. It is evidenced that the proposed relation for structural glasses from Alegria et al. [15] (dashed line in Figure (5.9)) perfectly works for the whole temperature and composition studied range.

5.1.2.4 Kirkwood factor

The existence of miscibility in the OD fcc phase evidenced by thermal and X-ray powder diffraction measurements, has enabled us to determine the volume of the cubic unit-cell and thus, the density as a function of the temperature and of the mole fraction.

Figure (5.10) shows the variation of the Kirkwood g factor as a function of temperature for pure compounds and several mixed crystals in the OD fcc phase. As far as the effective dipole moment of the molecular entity, it has been calculated for the mixtures following the procedure of the molecular volume for the packing coefficient, i.e., as a linear combination of the square dipole moment for the pure compounds with the mole fraction [23]. It is noteworthy to point out that if calculation of effective μ^2 is performed according to the other methods, like for instance weighting the square dipoles by volume fractions or by mass fractions [24,25] the trends are exactly the same and only an small shift, with a discrepancy less than 10%, on the Kirkwood factor is observed [26,27].

It should be noticed that g values for CNadm are slightly different from those previously published [28] probably because those authors kept the density constant ($1.13 gcm^{-3}$) for the whole temperature domain in their calculations.

For the analyzed pure compounds and mixed crystals, three straightforward results from the g factor are evidenced: (i) it is always smaller than unit; (ii) it decreases with increasing the mole fraction of CNadm and (iii) it increases with temperature. As for the first experimental finding, it means that short-range correlations orient dipole entities in a strong antiferroelectric order. As for the second, the results coherently support the fact that the packing coefficient (see figure (5.11)) increases with the mole fraction of CNadm giving then rise to an increase of the steric hindrance of the molecular reorientation.

And, as for the last, it simply makes evident the increase of thermal expansion with temperature yielding to a softening of the thermal vibrations going along with a small increase of the ε_s. Nevertheless, it should be mentioned that the stair-like behavior of g for some mixtures is a direct consequence of the changes of the permittivity strength as a function of temperature (see figure (5.7)). This effect points out a rapid development on cooling of a local arrangement of molecular dipoles that should be attributed to a strong increase of the antiferroelectric order at temperatures higher than the corresponding glass transition temperature, in good agreement with what recently found in pure CNadm [29].

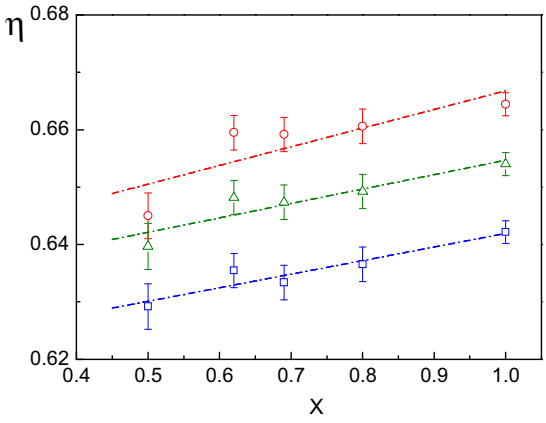

Figure 5.11: *Packing coefficient of the OD fcc* $(Cladm)_{1-x}(CNadm)_x$ *mixed crystals as a function of the mole fraction at several temperatures:* $178K$ *(circles),* $233K$ *(triangles) and* $288K$ *(squares). Lines are guides for the eyes.*

5.1.2.5 Discussion

The dynamics of the relaxation process corresponding to the molecular tumbling of molecules in the fcc lattice of the pure compound CNadm and the OD mixed crystals $(Cladm)_{1-x}(CNadm)_x$ for $0.5 \leq x \leq 1$ has been studied through dielectric spectroscopy.

The non-exponential character evidenced by the broadening of the α-relaxation peak and characterized by the β_{KWW} stretched parameter with the diminution of the mole fraction is caused by the heterogeneities produced by the concentration fluctuations which are the consequence of a statistic (chemical) disorder and not induced by dynamic correlations. This result shows that local hetero-geneities generated by the compositional disorder controls the broadening of the structural relaxation process, a result which is similar to that previously found for structural glasses [21]."

To enhance such a conclusion, Fig. 5.12 shows the overlap of several spectra under different condi-

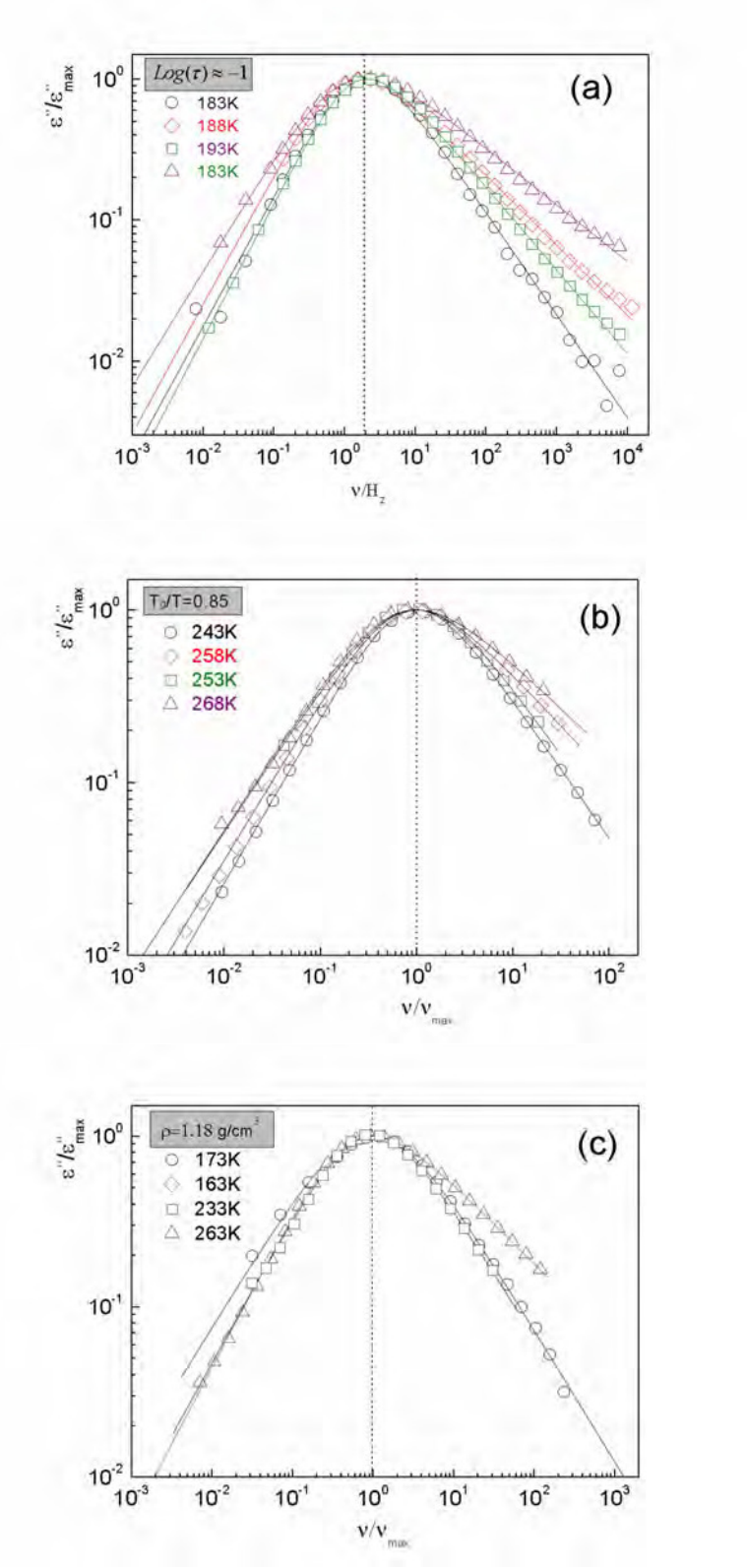

Figure 5.12: *Normalized dielectric spectra for some selected common values of relaxation time* $\log_{10}\tau = -1$*(a), reduced temperature* T_g/T*=0.85 (b), and density of* $1.18 gcm^{-3}$ *(c) for the mixed crystals* $(Cladm)_{1-x}(CNadm)_x$.

tions, equal relaxation time, equal distance to the glass transition temperature and equal density, in such a way the conclusion about the broadening is reinforced because there is not other reason that the composition disorder to account for the broadening (see Fig. 5.9 for the stretched exponent) of the relaxation peak.

This result shows that local heterogeneities generated by the compositional disorder control the relaxation process, a result which is similar to that previously found for structural glasses [21]. Local concentration fluctuations can broaden the loss peaks well above than what expected for a variation of intermolecular interactions.

For the mixed crystal $(Cladm)_{0.38}(CNadm)_{0.62}$ the distribution of the relaxation times appears to be sharper when compared to the observed general behavior of mixed crystals. Although it is difficult to establish a physical reason for such a result, it is clear that some kind of special short-range order appears for this composition making the dynamic behavior closer to that of CNadm pure compound as far as the distribution of the relaxation times is concerned

Finally, the results concerning the variation of the Kirkwood factor evidence a strong antiferroelectric order of molecular entities, which increases with the mole fraction of CNadm and with the decreasing of temperature. In addition, for all the compositions higher than 0.5 and even for CNadm pure compound, a stair-like diminution is observed between $220-240K$ as a consequence of the reinforcement of an antiferroelectric ordering. Such a change comes from an abrupt diminution of the dielectric strength together with a continuous variation of density as a function of temperature.

5.2 Derivative analysis

The application of the derivative procedure to the glass formig systems allows us the introduction of an enthalpy function $H_a(u_1,u_2)$ that for the case of VFT $(u_1 = D_T, u_2 = T_0)$, Avramov $(u_1 = C, u_2 = D)$, Elmatad $(u_1 = J_T, u_2 = T_0)$ and DSM $(u_1 = T_c, u_2 = \phi)$ equations, containts constants paramters related to the slope and intercept of a linear function. For such a reason, we call those models describing the relaxation time as linearized models. As previously discussed, the Mauro equation allows us the introduction of an enthalpy function. The parameters of the Mauro equation $(u_1 = K, u_2 = C)$ are not directly linked to those of a linear function, and therefore it is not possible to find, by means a derivative procedure, the associated linear function.

We present the results divided in two groups (linearized and non-linearized models). The first section focus on the linearized models, where the application of the derivative based, distortion-sensitive analysis to LCs and ODICs, materials are presented. In this section we also discussed the results concerning to the cases of the olygomeric liquid epoxy resin (EPON828), neopentylalcohol (NPA) and neopentylglycol (NPG) mixture$(NPA_{0.7}NPG_{0.3})$, isooctylcyanobiphenyl (8*OCB) and Propylene Carbonate (PC). In the second part we show the possibel empirical correlations between one the lienarized model with the universal pattern for the high frequency wing of the loss curve

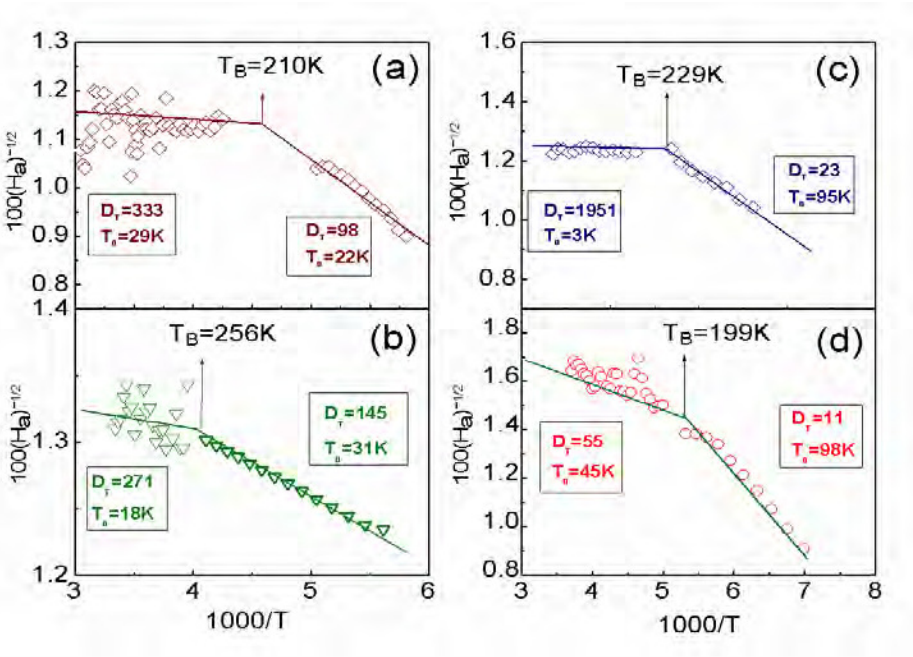

Figure 5.13: *Derivative-based analysis of the temperature variation of the dielectric relaxation according to equation (5.3), displaying the crossover between two distinct ranges of validity of the VFT model for cyclooctanol (a), cyanoadamantane (b), $(Cladm)_{0.38}(CNadm)_{0.62}$mixed crystal (c) and cyanocyclohexane (d).*

for primary relaxation time for LCs and ODICs. In the last part we show the application of the minimization procedure (see chapter 4) to 30 glass forming systems. The evidences of the existence of crossovers as well as a quantitative description are discussed. Whe show also a new procedure for detecting the crossover in a very easy way. A new kind of crossovers which seems to be impossible to be detected by the Stickel transformation are showed.

5.2.1 Linearized models

5.2.1.1 VFT description

The derivative based analysis of the VFT equation yields:

$$(H_a)^{\frac{1}{2}} = \left[\frac{d\ln\tau}{d\left(1/T\right)}\right]^{-1/2} = \left[\left(D_T T_0\right)^{-1/2}\right] - \frac{\left[T_0\left(D_T T_0\right)^{-1/2}\right]}{T} = A - \frac{B}{T} \tag{5.3}$$

where a linear regression analysis gives $T_0 = {}^{B}/_{A}$ and $D_T = {}^{1}/_{AB}$.
Following equation (5.3), a clear linear dependence of $(H_a)^{-1/2}$ and $1/T$ emerges, indicating then the domain of validity of the VFT equation. Then the linear regression yields optimal value of T_0 and coefficients D_T. Consequently, they can be substituted into the VFT equation, reducing the final fit solely to prefactor [31].
Figure (5.13) shows the linearized distortion-sensitive analysis applied to several Plastic Crystals.

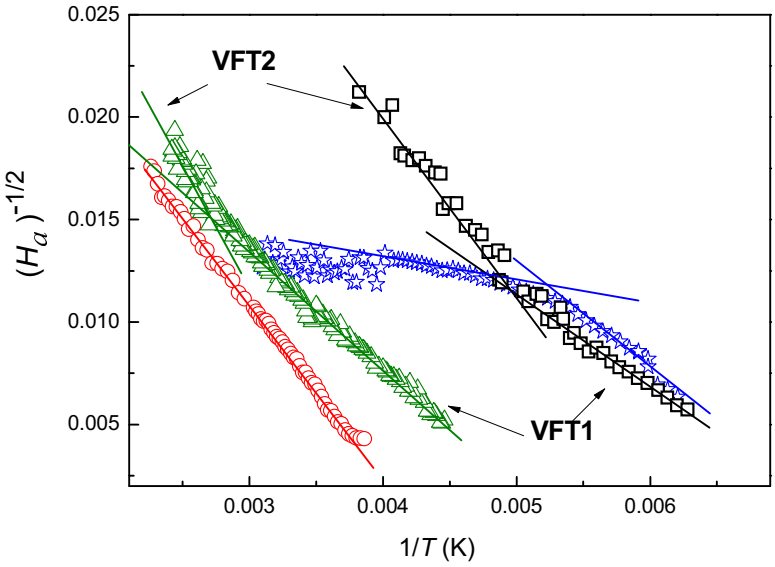

Figure 5.14: *VFT focused linearized distortion-sensitive analysis in the apparent activation enthalpy plane. VFT1 and VFT2 fits (continuous lines) are for subsequent dynamical domains. Stars are for NPANPG, triangles for 8*OCB, circles for EPON 828 and squares for PC .*

Table 5.3: *VFT description parameters obtained from the analysis in Fig (5.13) via eq. (5.3). Values of the prefactor are from the VFT fit with mentioned parameters.*

Materials	T_0 **(K) VFT1/VFT2**	D_T **VFT1/VFT2**	$\log_{10}[\tau_0$ **(s)] VFT1/VFT2**
NPANPG	134.0/70	5.0/41	-9.70/-14.12
8*OCB	188.2/239.9	5.6/2.4	-11.42/-11.04
EPON 828	-/232.7	-/3.3	-/-12.04
Prop. Carbonate	132.2/134.5	6.9/5.9	-13.73/-13.21

Two temperature dynamical domains are identified, which evidences the existence of two VFT regimes separated by a dynamical crossover temperature T_B.

The slope of the $[H_a]^{-1/2}$ decreases on decreasing temperature when crossing T_B, in addition with an increase of the Vogel temperature T_0 (except for cyclooctanol). According to equation (5.3) it means that the fragility strength parameter decreases for the following dynamical domain when approaching the glass transition temperature T_g. The latter feature is opposite to the one usually observed in supercooled liquids as it was already stated in previous studies of OD phases [32,33]. It is noteworthy that this is the first time that the previous findings obtained for an OD phase of a mixed crystal [32] are generalized for a variety of OD phases displayed by pure compounds or mixed crystals and regardless of the existence of hydrogen bonds.

Figure (5.14) shows results of the linearized analysis focused on the validity of the VFT equation.

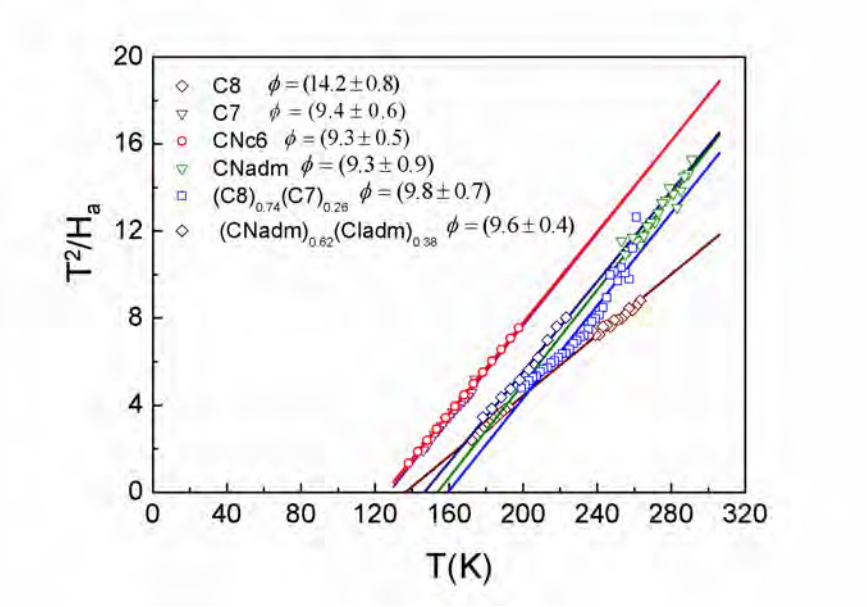

Figure 5.15: *Derivative-based analysis of the temperature variation of the dielectric relaxation according to the equation (5.4). The analysis have been performed for various OD phases of pure compounds and mixed crystals.*

There are two dynamical domains associated with different values of T_0 and D_T. All parameters are collected in Table (5.3). For molecular liquids the values of the subsequent dynamical domains decrease on shifting from the high-temperature to the low-temperature. For the case of the plastic mixed crystal(NPANPG) the opposite behavior occurs. It resembles the one observed for the isotropic phase of liquid crystals, where it was linked to the presence of prenematic fluctuations in the fluidlike surrounding. Prefactors ranges from $\sim 10^{-10}$ to $10^{-14}s$.

5.2.1.2 DSM and MCT description

Similar reasoning previously described can be used for the critical like DSM or MCT equations giving [34]:

$$\frac{T^2}{\frac{d\ln\tau}{d(1/T)}} = \frac{T_c}{\phi} - \frac{T}{\phi} = A - BT \tag{5.4}$$

Experimental data presented in the plot $T^2/H_a(T)$ vs T , should exhibit a linear behaviour in the domain of validity of the critical like equation [35]. The subsequent linear regression yields the optimal values of parameters $T_c = A/B$ and $\phi = 1/B$. The final fitting is reduced solely to prefactor τ_0. The analysis via equation (5.4) indicates also the domain of validity of the mode-coupling theory (MCT) behaviour in the high temperature domain [36-38].

As far as the validity of the single critical-like equation, the unequivocal validity of the dynamical scaling model is demonstrated by means of the linearized derivative analysis. The results lighted up by equation (5.4) are shown in figure (5.14) which displays $T^2/H_a(T)$ as a function of temperature

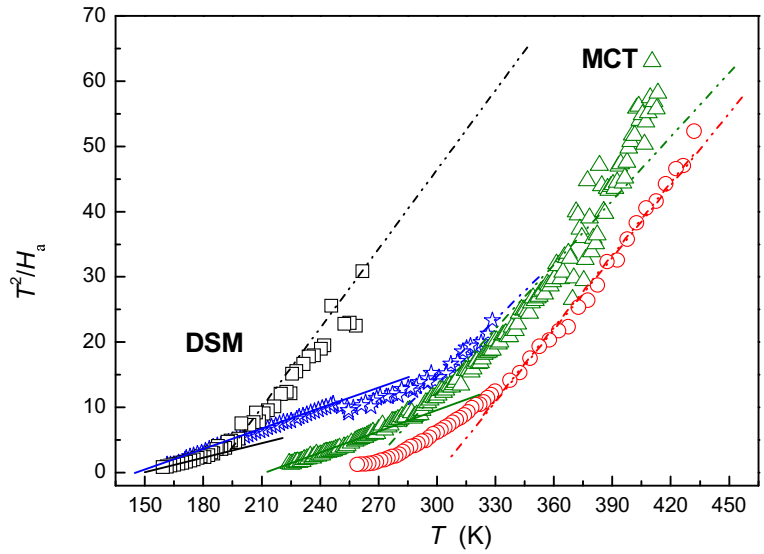

Figure 5.16: *The linearized distortions-sensitive analysis focused on the validity of "DSM" (low-temperature domain) and "MCT" (high-temperature domain) critical like descriptions. Compounds and symbols are as in Figure (5.14)*

Table 5.4: *"Critical-like" equation related parameters obtained from the analysis in Fig. (5.16) via eq. (5.4). Values of the prefactor are from the DSM and MCT fit with mentioned parameters.*

Material	**T_C (K) DSM/MCT**	**Power exponent DSM/MCT**	**$\log_{10}[\tau_0$ (s)] DSM/MCT**
NPANPG	150.0/248	9.2/3.72	-8.91/-11.23
8*OCB	212/258	8.9/3.65	-10.92/-10.31
EPON 828	-/290	-/2.96	- /-11.23
Prop. Carbonate	151/178	11.8 / 3.31	-13.44 /-11.15

for the set of pure compounds and mixed crystals studied. It is worth noticed that the critical-like behavior of the DSM model proposed by Colby is described with an exponent very close to the universal value ($\phi = 9$), except for cyclooctanol ($\phi \approx 14$) regardless the molecular composition and the presence of an hydrogen bonded scenario. These results for OD phases giving rise to orientational glasses indicate the possible significance of the existence of a translational order for the emergence of dynamical scaling model predictions. In addition, the results evidence the validity of the DSM for OD phases regardless of the possible existence of heterogeneities due to concentration fluctuations for mixed crystals.

The possibility of using critical-like parameterizations for another kind of materials is shown in figure (5.16). Also in this case the linear regression analysis can yield values of relevant parameters, collected in Table (5.4). Noteworthy is the superiority of the DSM–type behavior for ODIC and LC compound. For propylene carbonate (PC) such behavior can be noted only approximately,

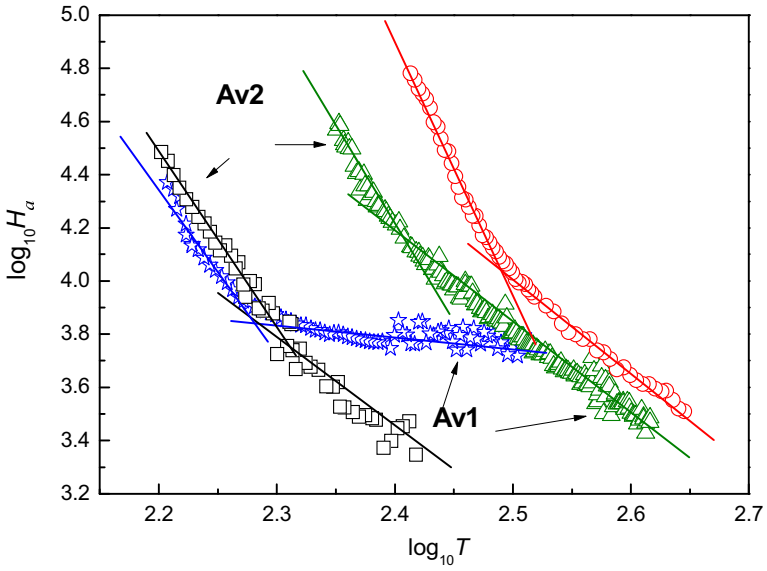

Figure 5.17: *"Avramov" equation focused linearized distortion-sensitive analysis in the apparent activation enthalpy plane. Av1 and Av2 domains are for subsequent dynamical domains. Compounds and symbols are as in Figure (5.14).*

Table 5.5: *"Avramov" equation related parameters obtained from the analysis in Figure (5.17) via equation (5.5). Values of the prefactor are from the Avramov fit with mentioned parameters.*

Material	***D*** **Av1/Av2**	***C*** **Av1/Av2**	$\log_{10}[\tau_0\,(s)]$ **Av1/Av2**
NPANPG	1.02/9.7	$7445/4.7\cdot10^{22}$	-18.51/-7.33
8*OCB	4.2/7.05	$1.35\cdot10^{11}/8.25\cdot10^{17}$	-9.97/-8.81
EPON 828	4.5/10.7	$1.60\cdot10^{12}/1.22\cdot10^{27}$	-11.15/-9.20
Prop. Carbonate	5.3/7.7	$1.10\cdot10^{13}/1.82\cdot10^{18}$	-10.55/-9.95

close to T_g. In each case a clear manifestation of the MCT related critical-like behavior in the high temperature domain appears.

5.2.1.3 Avramov description

For the "Avramov" equation, a similar linearized, derivative based analysis leads to :

$$\log\left[\frac{d\ln\tau}{d\left(1/T\right)}\right]=\log\left[H_a\right]=\log\left(CD\right)+\left(1-D\right)\log T=A+B\log T \tag{5.5}$$

On the plot $\log H_a$ vs $\log T$, the linear domain indicates the range of validity of the Avramov equation. Then the linear regression yields optimal values of coefficients: $D=1-B$ and $C={}^{10^A}/_{(1-B)}$.

The possibility of using "Avramov" equation for portraying $\tau(T)$ behavior is shown via linear

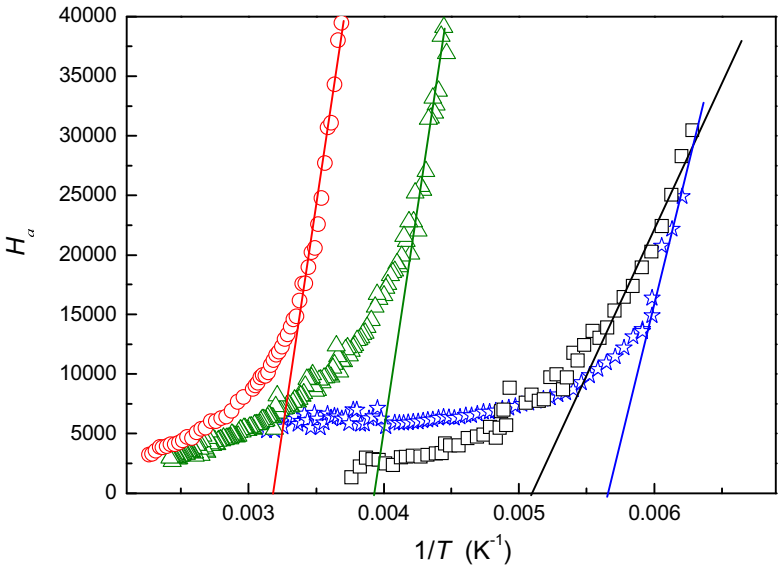

Figure 5.18: *Elmatad et al. [39] equation focused linearized distortions-sensitive analysis in the apparent activation enthalpy space. The domain of its validity should follow a linear dependence.Compounds and symbols are as in Figure (5.14).*

Table 5.6: *Elmatad et al. [39] equation related parameters obtained from the analysis in Fig.(5.18) via eq. (5.6). Values of the prefactor are from the Elmatad fit with mentioned parameters.*

Material	$J/T_0^{'}$	T_0 **(K)**	$\log_{10}[\tau_0$ **(s)]**
NPANPG	16.1	180.0	-1.74
8*OCB	15.3	256	-4.16
EPON 828	13.9	309	-7.26
Prop. Carbonate	10.27	202	-7.22

domains in Figure (5.17). Noteworthy is the clear manifestation of two dynamical domains do not reported for such parameterization so far. For NPANPG plastic crystal two linear domains are indicated although this assumption is valid only within the limit of the experimental error. Values of parameters, obtained via linear regression of equation (5.5) are given in Table (5.5). Noteworthy is the fact that prefactors are significantly smaller than for the VFT equation.

5.2.1.4 Elmatad description

Similar reasoning as above can be used for Elmatad et al. equation [39], leads to the dependence:

$$H_a = \frac{d\ln\tau}{d\left(1/T\right)} = \frac{2J^{'}T_0^{'2}}{T} - 2J^{'}T_0^{'} = \frac{B}{T} - A \tag{5.6}$$

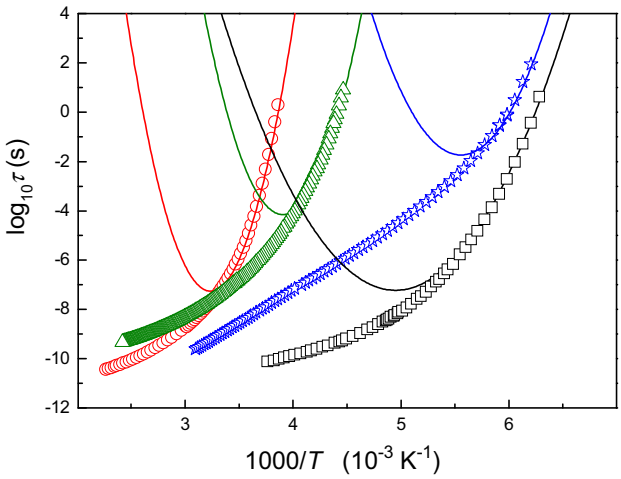

Figure 5.19: *Results of fitting experimental data via Elmatad et. al.[39] equation with sets of parameters from Table (5.6).Compounds and symbols are as in Figure (5.14).*

At the plot $H_a(T)$vs $1/T$, the domain of validity of Elmatad equation is indicated by a linear dependence. Following the linear regression yields the $J^{'}$ and $T_0^{'}$ parameters.
The distortions-sensitive linearized analysis for the equation (5.6) is presented in figure (5.18). Parameters obtained from the linear regression analysis are given in Table (5.6). Figure (5.18) reveals a limited validity of such description, hardly visible in the direct plot $\tau(T)$ shown in Figure (5.19).

5.2.1.5 Discussion

To resolve the puzzling situation for portraying the upsurge of dynamic properties on approaching the glass temperature the analysis of leading equations was presented. It has been carried out by the use of the derivate analysis of the the apparent enthalpy $H_a = d\ln\tau(T)/d(1/T)$ which reduces the number of fitted parameters and to reveal subtle distortions from the given equation. This way of analysis also yields optimal values of leading parameters, reducing the final fitting of $\tau(T)$ data solely to prefactors τ_0. The analysis showed that for two VFT equations are needed to describe $\tau(T)$ in the broader range of temperatures. In agreement with earlier reports we found a superior validity of the critical-like description in the ultraviscous/ultraslowing domain for the liquid crystalline glass formers and the orientationally disordered crystals. In particular, as clearly indicated in Figs. 5.15 and 5.16, the Dynamical Scaling Model [35] perfectly describes the low-temperature domain, while the Mode Coupling Theory [38] is able to account for the high-temperature domain. Then, both critical-like models seem to account for the dynamics of glass formers. The linearized analysis revealed a limited validity of the equation recently proposed by Elmatad et al [39], hardly visible at the $\tau(T)$ plot. Nevertheless, we would like to stress that at present one model describing all the features of glass forming systems does not exist.

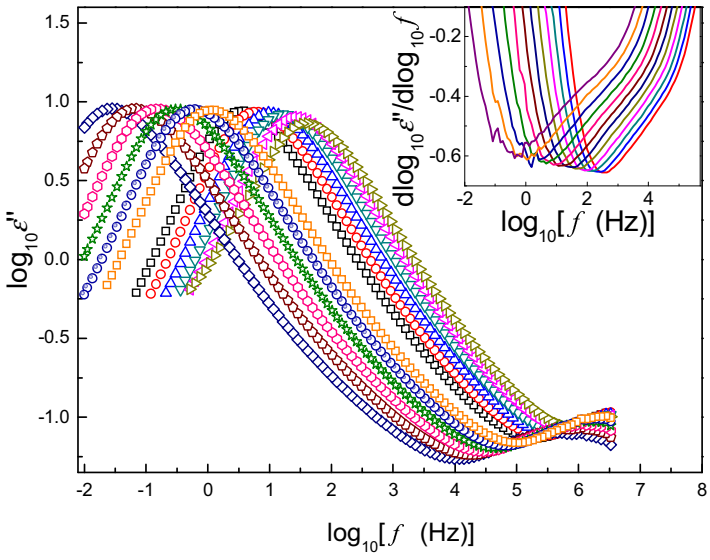

Figure 5.20: *Double logarithmic representations of dielectric loss spectra* $\log_{10}\varepsilon''$ *as function of frequency of cycloheptanol (C7-ol) ODIC phase from 146 to 168 K each 2 K. Inset shows the derivative of the loss spectra as a function of frequency for the same temperatures [43].*

5.2.2 Universal pattern

Recently Nielsen et al [40] demonstrated an experimental evidence for the prevalence of universal $\sqrt{t}$ time decay, or equivalently $f^{-1/2}$ in frequency relaxation, of the distribution of relaxation times in glass forming liquids on approaching the glass temperature T_g. In fact this issue was first pointed out a decade ago for the high frequency wing of dielectric loss curves $\varepsilon''(f)$ that obeys the time-temperature superposition (TTS) [41]. However, it was shown by means of the analysis of 53 low molecular liquids that the correlation with TTS is not obligatory [40].

These results mean that a clear quantitative universal pattern for the distribution of relaxation times was identified in the immediate vicinity of the glass transition point in supercooled liquids

Neither LC nor ODIC glass formers were considered in [40-42] for searching the possible universal pattern of the distribution of relaxation times, namely:

$$\varepsilon''(f)_{T\to T_g} \propto f^{-n\to -1/2} \tag{5.7}$$

where $f > f^{\alpha}_{peak}$, $\varepsilon''(f)$ is for dielectric loss curve and $\tau = 1/2\pi f_{peak}$.

We will show here that a similar universality occurs for glass forming liquid crystals and orientationally disordered crystals (ODIC), although some differences concerning the universal values appear. Empirical correlations of the found behaviour are also briefly discussed.

Figure (5.20) shows the example of the plot $\log_{10}\varepsilon''$ vs $\log_{10} f$, for dielectric loss curves in cycloheptanol ODIC phase. The inset presents results of the derivative based analysis of the distribution of relaxation times $d\log_{10}\varepsilon''/d\log_{10} f$ vs $\log_{10} f$. The minimal values on the plots in the inset show the slope at the point of bending for $\log_{10}\varepsilon''$ vs $\log_{10} f$ curve. In this way all slopes related

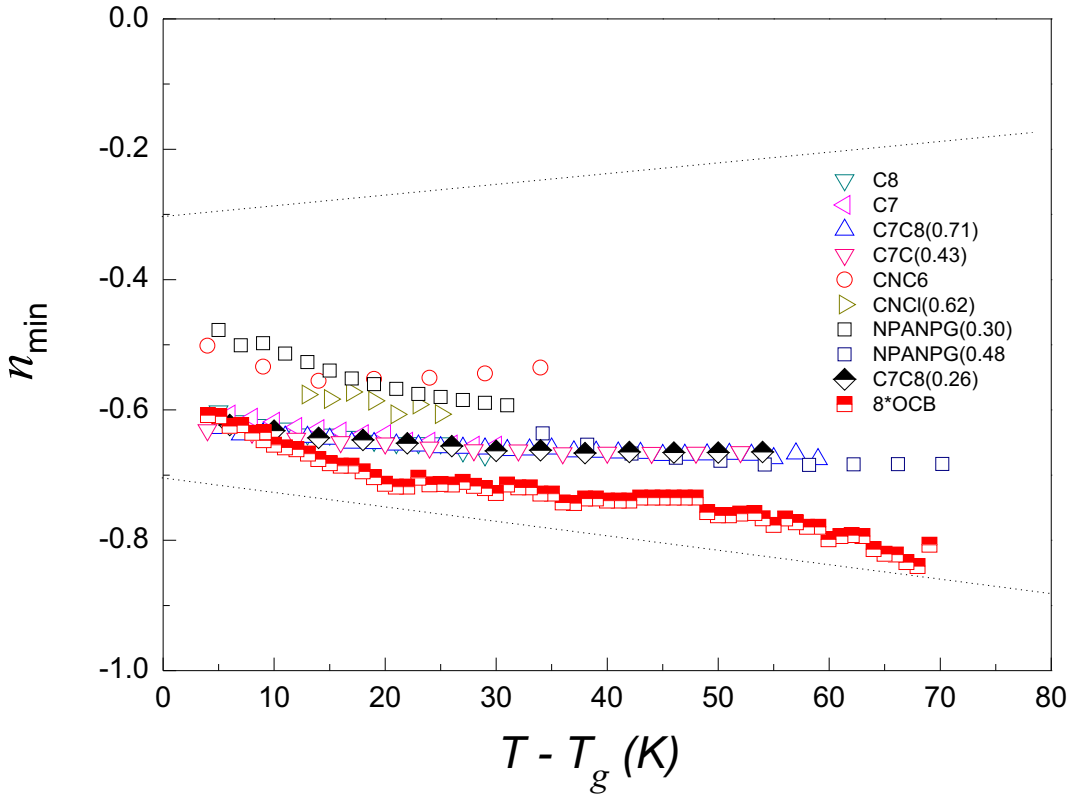

Figure 5.21: *The minimal values obtained from the derivative at the point of bending for* $\log_{10}\varepsilon''$ vs $\log_{10} f$ *vs. curve for several ODICs and 8*OCB LC. The compounds presented in the figure are: C8: C8-ol Cyclooctanol; C7: C7-ol Cycloheptanol, and their mixed ODIC crystals C7C8(0.71):* $(C7-ol)_{0.29}(C8-ol)_{0.71}$*; C7C8(0.43):* $(C7-ol)_{0.57}(C8-ol)_{0.43}$*; C7C8(0.26):* $(C7-ol)_{0.74}(C8-ol)_{0.26}$ *[43]; CNC6: Cyanocyclohexane [44]; ; Neopentylalcohol and Neopentylglycol mixed crystals, NPANPG(0.30):* $(NPA)_{0.70}(NPG)_{0.30}$ *and NPANPG(0.48):* $(NPA)_{0.52}(NPG)_{0.48}$ *[45].*

to equation (5.7) were determined. Following this way of analysis, results recalling equation (5.7) are shown in figure (5.21) for ODIC and for an LC. To get the minimal slope at the glass transition temperature T_g, the values of n as a function of temperature were linearly extrapolated at T_g temperature.

5.2.2.1 Empirical correlations

Figure (5.22) shows that small deviation from the above pattern occurring for ODICs can be correlated with the discrepancy from the liniearized equation DSM with exponent $\phi \approx 9$. The values were taken from previous analyses under the DSM framework. One may speculate that this behaviour may be associated with the fact that vitrification occurs slightly different for orientationally disordered phases, due to steric hindrances or intermolecular interactions.

The observed behaviour can also be linked with the fragility changes. First, Alvarez et al. [46]

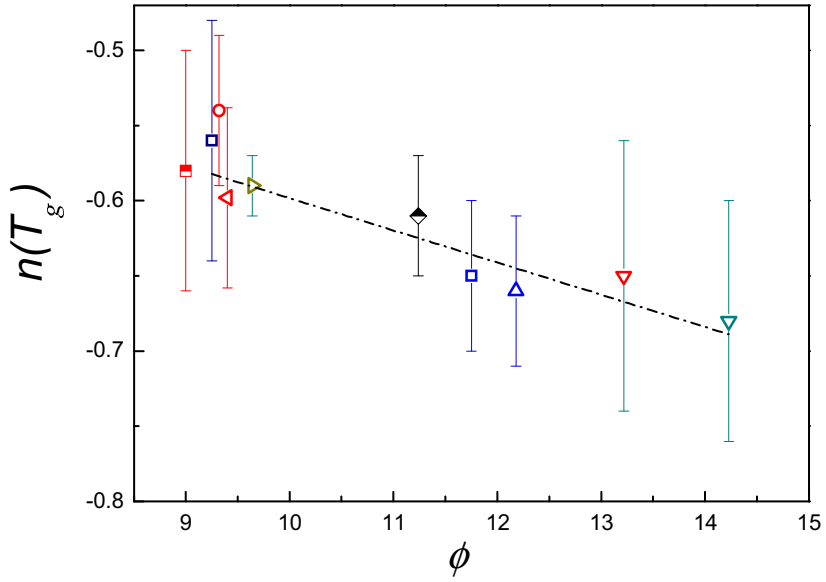

Figure 5.22: *Minimal slope (n = nmin) at the glass transition temperature as a function of the critical exponent for the dynamical scaling model. Symbols are as in Figure (5.21).*

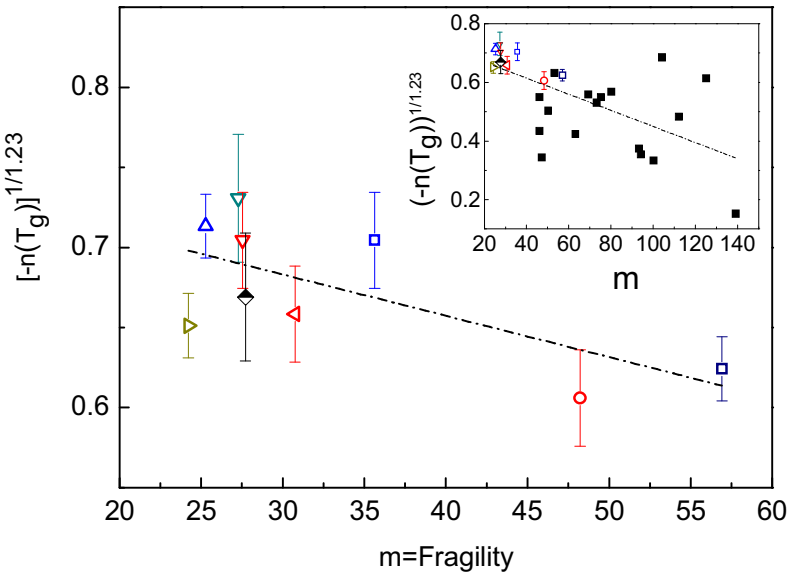

Figure 5.23: *Correlation between the minimal slope n at the glass transition temperature and fragility for ODIC systems. Symbols as in Figure (5.21). The inset displays the same correlation extended for some canonical glass formers (black squares). The data were obtained by combining the values obtained from references [30], [49], [51], [52] and [53].*

proposed a link between the Havriliak-Negami [47, 48] distribution power exponents $(\alpha_{HN,}\beta_{HN})$ and the KWW stretched exponent β_{KWW}, namely: $\beta_{KWW} = (\alpha_{HN,}\beta_{HN})^{1/1.23}$. Recalling the well known fact that $\alpha_{HN,}\beta_{HN} = -n$ then $\beta_{KWW} = (-n)^{1/1.23}$. Böhmer et al. [49] found an empirical relation linking β_{KWW} and fragility coefficient m=$d\log_{10}\tau/d\log_{10}(T_g/T)$, namely: $m = m_0 - s\beta_{KWW}$, where $m_0 = 250$ and $s = 320$. This relation and the linearity emerging from Figure (5.22), yield:

$$m = m_0 - s\beta_{KWW} = m_0 - s(-n)^{1/1.23} \approx m_0 - s'(\phi)^{1/1.23} \tag{5.8}$$

It would then mean that fragility and the slope of the dielectric loss spectra of the α-relaxation at $f > f^{\alpha}_{peak}$ should be correlated $m_0 - s(-n)^{1/1.23}$. Figure (5.22) shows up the correlation $m = 295 - 387(-n)^{1/1.23}$ for ODIC. The correlation can be extended for other glass formers (see inset in figure (5.23)), the reciprocal of the obtained experimental slope is (ca. 365) very close to the value proposed by Böhmer et al.[49].

Concluding, the clear quantitative universality for the distribution of relaxation times is present not only for organic vitrifying liquids but also for glass forming experimental model systems, namely rod like liquid crystalline glass formers and for orientationally disordered crystals. In addition, it seems that this universality is linked to that proposed from the dynamical scaling model and, subsequently, this fact reinforces the Böhmer correlation between fragility and the β_{KWW} exponent.

5.2.3 Non-Linearized models

5.2.3.1 Mininimization procedure of the Mauro equation

The form of the equation introduced by Mauro et al. [54] does not allow a similar straightforward linearization procedure. In fact, the application of the derivative procedure to the Mauro et al. equation gives rise to the enthalpy function in the form:

$$H_a(T) = \frac{d\ln\tau}{d(1/T)} = K\left(1 + \frac{C}{T}\right)\exp\frac{C}{T} \tag{5.9}$$

Unlike the previous models, the parameters (K, C) are not correlated with the slope and the intercept of a linear function, thus both variables being necessarily and simultaneously involved in the data analysis.

The estimates of the model parameters are chosen to minimize a function of merit given by the sum of weighted squared residuals [55], which, for the Mauro equation it can be written as:

$$\chi^2_{Ha3D}(C, K) = \frac{1}{N-2}\sum_{i=1}^{N}\left(1 - \frac{\frac{d\ln\tau_i}{d(1/T_i)}}{K\left(1 + \frac{C}{T_i}\right)\exp\left(\frac{C}{T_i}\right)}\right)^2 \tag{5.10}$$

The optimization method that has been used in this work is iterative, so starting values are required for the parameter search. As we have discussed in the Chapter 4, careful choice of starting values

is necessary as the parameter estimates may represent a local minimum in the function of merit. To make the linearization process of the equation (5.9) similar to the previous equations, the plot of $\ln\left[H_a/\left(1+\frac{C}{T}\right)\right]$ vs $1/T$ should appear as a linear curve for the domain of validity of the Mauro equation, as it clearly follows rewritting equation (5.9) as:

$$\ln\left[\frac{H_a}{1+\frac{C}{T}}\right] = \ln K + \frac{C}{T} \tag{5.11}$$

The above equation involves in their left side not only the enthalpy values derived from the experimental data, it also involves the parameter C which is obtained from the minimization process. Table (5.7) list the values of the minimization results for the 30 liquids studied, where the relaxation time data $\tau(T)$ were taken from [56-77]. For all liquids reported in Table (5.7), the Mauro constant C and K represent a local minimum in the function of merit $\chi^2_{Ha3D} = f(C,K)$ associated to the $3D$-enthalpy space, which are obtained by the procedure dicussed in the Chapter 4. For the $3D$-enthalpy space, the final fit of $\tau(T)$ requires a final assesment of the τ_0 prefactor, which are also reported in Table (5.7).

5.2.3.2 Complementary dielectric datas

The following experimental dielectric relaxation time datas $\tau(T)$ have been used in this work for testing the minimization procedure of the Mauro equation. The systems are presented following the same order showed in the tables added at the end of the chapter. The short-name of the systems used in this work follows the international scientific common nomenclature:
bisphenol **(EPON828)** [56], epoxy resins, poly[(phenyl glycidyl ether)-co-formaldehyde] **(PPGE)** [56], o-terphenyl **(OTP)** [57], Kresolphtalein-di-methylether **(KDE)** [58], Propylene carbonate **(PC)** [59], phenylsalicylate (**salol**) [60], Diethylphthalate(**DEP**) [61], 2-methyltetrahydrofuran (**MTHF**) [62], different mixtures (42,54 and 62%) of polychlorinatedbiphenyl (**PCB42**, **PCB54**, **PCB62**) [63], polystyrene with molecular weight 540k (**PS540k**) [64], **Glycerol** [65], propyleneglycol (**PG**) [65], dipropyleneglycol (**2PG**) [65], Dibutylphthalate (**DBP**) [66], two different datas of tripropyleneglycol (3PG) which are tripropylene glycol **(3PG)a** [67], and **(3PG)b** [68], **Ethanol** [69], **Xylitol** [70], Diclorodiflurometano(**freon12**) [71], four different datas of polyvinylacetate (PVac) obtained from different authors **(PVac)a** [72], **(PVac)b** [73], **(PVac)d** [74], **(PVac)f** [75], isooctylcyanobiphenyl **(8*OCB)** [76], phenylbenzene **(E7)** [34], cycloheptanol(C7-ol) and cyclooctanol (C8-ol) mixture $(C8-ol)_{0.74}(c7-ol)_{0.26}$ [43], Neopentylalcohol (NPA) and Neopentylglycol (NPG) mixed crystals: $(NPA)_{0.70}(NPG)_{0.30}$ [32], isopentylcyanobiphenyl **(5*CB)** [77]. The datas were taken from earlier authors' studies.

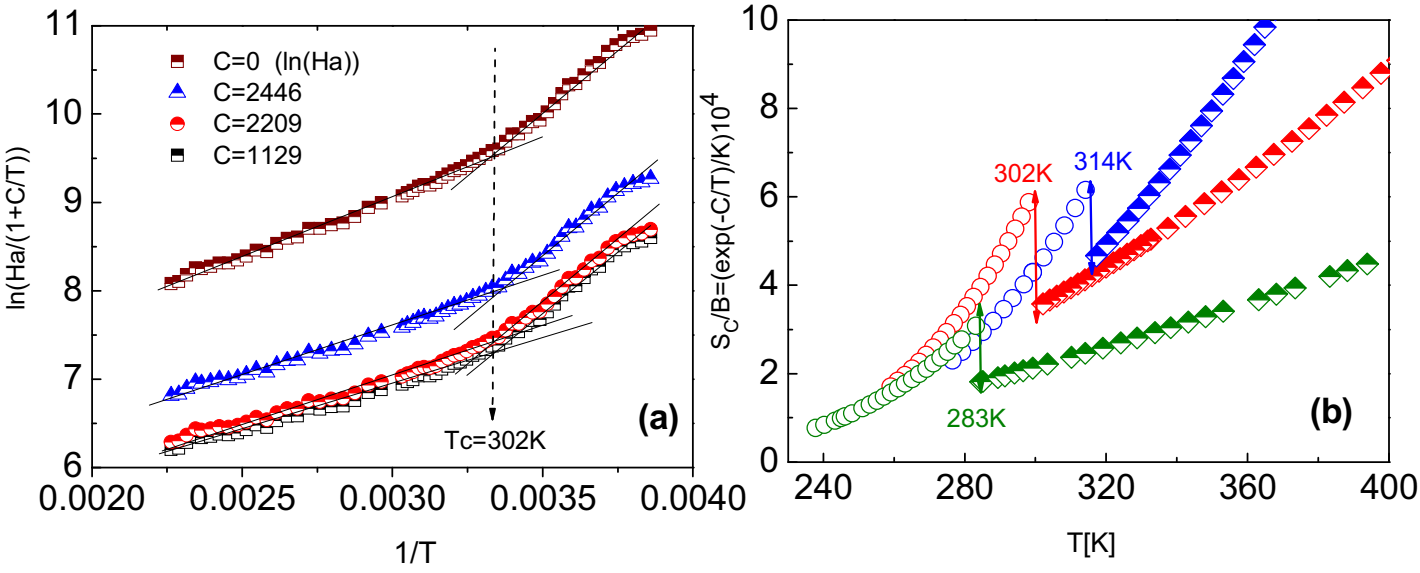

Figure 5.24: *Both figure show quantitative examples of the evidence of dynamical crossovers in the Mauro equation. Figure (a) shows the plot* $\ln\left[H_a/\left(1+\frac{C}{T}\right)\right]$ *vs* $1/T$ *for the case of EPON828 for different values of C parameter. Two temperature domains can be detected by a slope change at the crossover temperature* (T_c) *which does not depends of the C constant values. Figure (b) shows the plot of the configurational entropy rescaled by B as a function of the temperature for the cases EPON828(red), OTP(green) and PPGE(blue). A configurational entropy jump appear at the crossover temperature* (T_c).

5.2.3.3 Evidence of the existence of crossover in the Mauro equation

Figure (5.24a) shows the plot $\ln\left[H_a/\left(1+\frac{C}{T}\right)\right]$ vs $1/T$ for the case of EPON828. As it is showed, two temperature domains can be detected by a slope change at temperature (T_c) which signs a dynamic change. It gives an evidence of the existence of a possible dynamic crossover in the Mauro equation. The graph also gives us another surprisingly conclusion. From the graph (5.24a) we can conclude that the crossover temperatue (T_c) does not depend of the C constant values. It means that independently of any selected minimization procedure the possible dynamic crossover can be detected by a slope change in one simple plot of $\ln[H_a]$vs $1/T$.

On the other hand, following the energy landscape analysis of Naumis [78] and the temperature-dependent constraint model of Gupta et al. [79], as weell as the assumption of a simple two-state system in which the network constraints are either intact or broken, Mauro et. al. [54] gives an equation for calculating the configurational entropy S_c of the system, which is written as:

$$S_c(T) = \frac{B}{K}\exp\left(-\frac{C}{T}\right) \tag{5.12}$$

where K and C are the Mauro constants and B is an effective activation barrier, which is typically left as a fitting parameter.

Figure (5.24b) shows the plot of the configurational entropy rescaled by B as a function of the

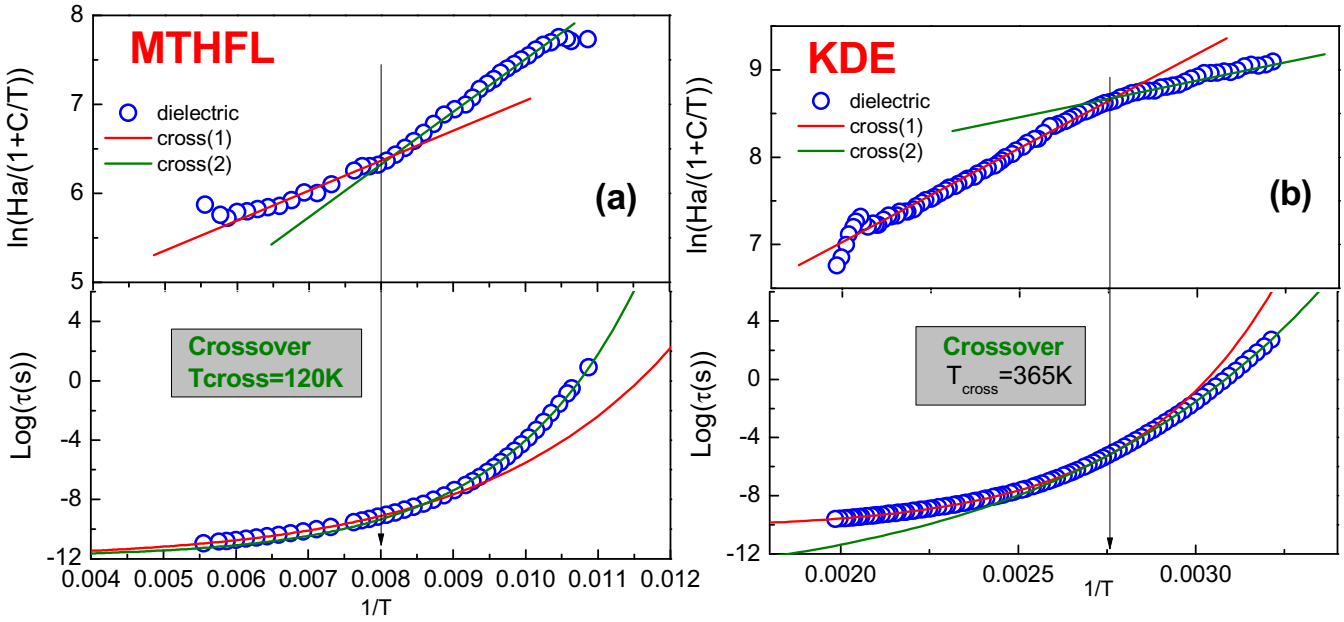

Figure 5.25: *Figure (a) and (b) show representative examples of the crossovers (up and down). It has been plotted for the cases of MTHFL and KDE respectivetly.*

temperature for the cases EPON, PPG and OTP. The different set of crossovers constant values C and K were taken from Table (5.8) and were calculated by the previously discussed minimization procedure. A configurational normalized entropy jump appear at the crossover temperature (T_c), which gives us another way to represent the evidence of the existence of dynamical crossover in the Mauro equation.

The possible dynamic crossovers in all liquids under study were tested. We found two different kinds of crossovers. One group of liquids where the slope in the graph $\ln\left[H_a/\left(1+\frac{C}{T}\right)\right]$ vs $1/T$ increases on cooling toward T_c (crossover up) as well as another group of liquids where the slope of the graph decreases (crossover down). Figure (5.24a) and (5.24b) show representative examples of this crossover which has been plotted for the cases of MTHFL and KDE respectivetly. How different are these crossovers as compared with the crossovers detected by the Stickel procedure [30]? Can these crossovers be correlate with some dynamic relevance magnitude?

5.2.3.4 Dynamic correlations

For most glass-forming liquids, a single fragility parameter at T_g is sufficient to describe equilibrium dynamics across the full range of temperatures. However, certain glass formers [80] require two different fragility parameters to reflect the changing fragility of those liquids in different temperature regimes. On cooling toward T_g, the temperature dependence of the α-relaxation time will change from Arrhenius high temperature to a pronounced non-Arrhenius behaviour at lower temperature, yielding the so called fragile-to strong $(F-S)$ liquid transition, which was first discovered in water by Ito et al.[81].

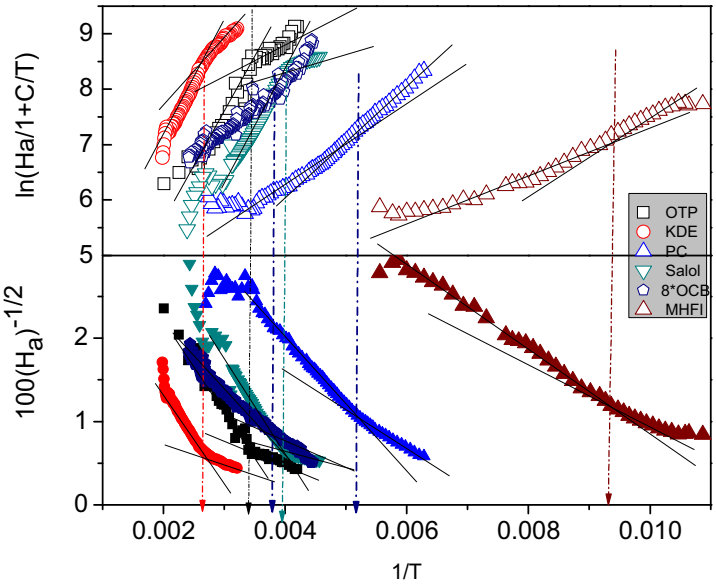

Figure 5.26: *The figure yields examples for 6 liquids under study. It shows the dynamical crossovers estimated by the Mauro (upper panel) and the VFT equation(botton panel). The temperature crossover values are aproximately the same. The change of the slope in (upper panel) is not always unique like the VFT representation. For the cases of PC and MTHFL we found a new slope changes which is impossibel to detect by the Stickel transformation. It would be related with the characteristic of the liquid transition.*

This transition can be quantified by the change of the fragility parameter m. Taking in to account the definition of the fragility [82-85] as well as the relaxation time temperature dependece $\tau(T)$ of the Mauro model, the index fragility m for this case will be written as the following equation[1]:

$$m = \frac{K}{\ln(10)\,T_g}\left(1+\frac{C}{T_g}\right)\exp\left(\frac{C}{T_g}\right) \tag{5.13}$$

where K and C are the Mauro constants and T_g is the standard glass transition temperature.
In this work, for the Mauro equation, we quantified the extent of the $(S-F)$ transition performing two steps of data analysis around the temperature crossovers T_c. In the first step, the parameters K_1 and C_1 are obtained by the enthalpy space analysis procedure in the high temperature domain $(T > T_c)$ from which the fragility parameter m_1 is calculated using equation (5.13). The parameter m_1 quantifies the fragility of the supercooled liquids far from T_g. In the second step, for the low-temperature domain $(T_g < T < T_c)$, the parameters K_2 and C_2 are obtained by the same procedure allowings us another set of parameters, from which the fragility parameter m_2 is also obtained by equation (5.13). The parameter m_2 quantifies the fragility of the liquids near to T_g.
For a liquid without $(S-F)$ or $(F-S)$ transitions, m_1 and m_2 have the same value. However, for a liquid with a $(S-F)$ transition $m_1 < m_2$ and for the case of $(F-S)$ transition, $m_1 > m_2$. We quantified the difference in fragility around the crossover temperature T_c by the ratio m_1/m_2 which

[1]The fragility equation published by Zhang et al.[80] was resported in a wrong way without the term $\ln(10)$

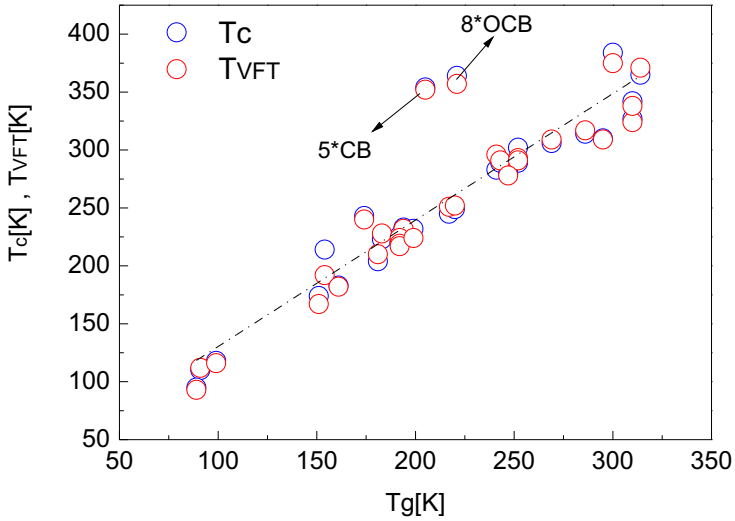

Figure 5.27: *Plots of $T_{VFT}\,(T_g)$ and $T_c\,(T_g)$. Except the cases of the 5*CB and 8*OCB, we can conclude that all liquids under study surprisingly follow a good linear correlation.*

we define as the fragility transition factor f as :

$$f = \frac{m_1}{m_2} = \begin{cases} 0 < f < 1 & (S-F) \\ f > 1 & (F-S) \end{cases} \tag{5.14}$$

We propose this factor as a quantitative measure for characterizing the glass behaviour around the crossovers. The larger the factor f, the larger is the extent of the$(F-S)$ transition during heating the liquid from T_g. A ratio of fragility was previously introduced by Chang et al.[87] by the fragility parameter defined around the equilibrium temperature T_{liq} on cooling metallic glass-forming liquids. They did not report any crossover in their equation, so their fragility transition factor takes values always larger than the unity and thus reporting only materials with $(F-S)$ transitions. Our way for detecting the dynamical crossover gives rise to distinguish liquids with both transitions $(F-S)$ and $(S-F)$ which are impossible to detect by Stikel analysis [30].

Table (5.8) lists the constant values $\log_{10}\tau_0$, K, C ,T_g and m, of the liquids under study. These parameters were calculated for both temperature domains above and below T_c. The T_g values were obtained by the numerical solution of Mauro equation at $100s$. Table (5.9) list the values of the crossover temperature T_c, the experimental glass transition temperature T_g, the ratio T_c/T_g, the relative difference of T_c with respect to T_{VFT} as well as the transition factor f for all of the liquids under study. The crossover temperature T_{VFT} is calculated by the liniarized derivative analysis of the VFT equation.

For all liquids under studied the results reported in Table (5.9) show that there is not big difference between the crossover temperature values of the VFT and the Mauro equation, but this relative difference can be positive o negative. The Figure (5.26) shows results for six liquids. It shows

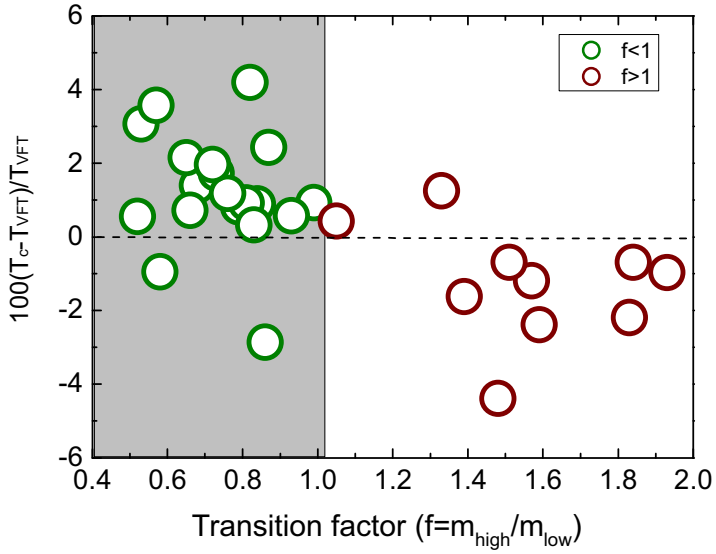

Figure 5.28: *Plot of the relative temperature crossover difference vs the fragilty transition factor. Values of f smaller or larger than $f = 1$ will define two system domains. For the cases of PPGE, MTHFL, DBP, the fragility transition factor $f < 1$ and their relative temperature crossover difference take negative values. For PG the fragility transition factor gets values $f > 1$ and its relative temperature crossover difference is positive.*

the dynamical crossovers calculated by the Mauro and the VFT equation. The crossovers are very close, but the change of the slope in our crossover representation is not always unique like the VFT representation. For the cases of PC and MTHFL we obtain a different slope changes that it would be related with the characteristic liquid transitions. Both temperature crossovers can be correlated with the experimental glass transition temperature.

Figure (5.27) shows the plots of $T_{VFT}\,(T_g)$ and $T_c\,(T_g)$. Except the cases of the 5*CB and 8*OCB, we can conclude that all liquids under study surprisingly follows a good linear correlation. It can give us a practice and easy way for estimating the crossovers when the experimental glass transition temperature of the liquid under study is previously known.

Figure (5.28) gives us another surprisingly correlation. Although, for all liquids under study the relative temperature crossover difference is very small, it will be correlate with the fragility transition factor f as it is showed. Liquids with fragility transition factors $f < 1$ $(S-F)$ will have a temperature crossover T_c farther to T_g that in the case of VFT crossover temperature. Liquids with fragility transition factors $f > 1 (F-S)$ have a crossover T_{VFT} farther to T_g that in the case of the Mauro crossover. We found four execptions, for the cases of PPGE, MTHFL, DBP, the fragility transition factor $f < 1$ and for PG it gets values $f > 1$.

Table 5.7: *Values of the minimization results for the liquids under study. The Mauro constants C and K represent a local minimum of the function of merit $\chi^2_{Ha3D} = f(C,K)$ associated to the 3D-enthalpy space, which are obtained by the procedure dicussed in the Chapter 4. For the 3D-enthalpy space, the final fit of $\tau(T)$ requires a final assesment of the τ_0 prefactor, which are also reported in the table.*

Materials	$\log_{10}\tau_0$	**K[1/K]**	**C[1/K]**
EPON[56]	-12.39	856.6	229
PPGE[56]	-2.01	7.13	1809.5
OTP[57]	-13.07	70.49	1160.59
KDE[58]	-11.13	83.34	1489.49
PC[59]	-10.72	9.90	960.94
Salol[60]	-11.23	23.38	1230.42
DEP[61]	-11.99	132.93	679.93
MTH[62	-11.53	15.09	475.04
PCB42[63]	-12.35	150.09	855.94
PCB54[63]	-11.74	116.14	1040
PCB62[63]	-14.06	498.59	797.81
PS540k[64]	-11.83	17.36	1526.2
Glycerol[65]	-12.15	934.87	371.49
PG[65]	-11.32	632.85	374.53
2PG[65]	-9.82	155.17	684.92
DBP[66]	-8.86	42.31	848.32
3PGa[67]	-10.79	63.54	862.76
3PGb[68]	-9.93	27.81	1009.37
Ethanol[69]	-9.62	116.89	310.87
Xylitol[70]	-10.81	16.08	1510.09
Freon12[71]	-8.55	0.71	716.11
PVaca[72]	-8.64	6.07	2209.6
PVacb[73]	-7.91	2.66	2374.3
Pvacc[74]	-10.03	11.26	2066.45
Pvacd[75]	-10.04	35.98	1632.06
8*OCB[76]	-9.74	48.35	1108.17
E7[34]	-8.42	19.49	1154.87
***C8c7*[43]**	-11.74	1488.59	175.46
***NPGNPA*[32]**	-10.82	304.06	793.95
5*CB[77]	-9.55	40.43	1051.58

Table 5.8: *Values of* $\log_{10}\tau_0$, *K, C , and* T_g *and fragility parameter m, for the liquids under study. These parameters were calculated for both temperature domains above and below* T_c. *The* T_g *values were obtained by the numerical solution of Mauro equation at* 100*s*. *The liquids with a fragille-strong* $(F-S)$ *transition are in bold.*

Materials	$\log_{10}\tau_0 1$	**K1 [1/K]**	**C1 [1/K]**	**Tg1 [K]**	**m 1**	$\log_{10}\tau_0 2$	**K2 [1/K]**	**C2 [1/K]**	**Tg2 [K]**	**m2**
EPON[56]	-11.29	66.55	1129	240	76	-9.54	0.46	2446.5	252	142
PPGE[56]	-3.03	59.5	1203.1	297	26	-1.50	1.18	2270.9	286	45
OTP[57]	-11.69	2.2	2062.7	252	123	-15.25	210.8	929.3	243	83
KDE[58]	-10.24	9.53	2211	322	97	-14.52	487.2	1005.9	314	70
PC[59]	-11.03	43.2	686.3	148	73	-10.55	8.03	991.98	157	90
Salol[60]	-10.43	1.40	1886.8	224	116	-22.09	1611.5	439.02	218	73
DEP[61]	-10.49	5.62	1300.9	189	99	-20.73	2399.8	243.9	179	54
MTH[62	-11.87	68.4	306.4	84	65	-11.83	17.99	460.5	91	82
PCB42[63]	-10.22	5.41	1602.8	227	99	-26.06	4182.1	271.15	221	63
PCB54[63]	-9.87	1.57	2169.2	258	112	-23.10	3467.1	350.37	247	61
PCB62[63]	-9.95	2.04	2295.2	279	110	-37.39	15570	119.39	268	57
PS540k[64]	-9.72	2.23	2069.3	255	116	-11.19	60.60	1237.2	255	77
Glycerol[65]	-11.72	759.6	408.9	195	43	-12.99	1183.9	336.69	194	41
PG[65]	-10.12	183.32	620.27	186	53	-12.34	935.46	317.35	175	40
2PG[65]	-10.31	292.15	557.74	191	48	-8.64	61.47	843.04	194	57
DBP[66]	- 9.50	121.05	655.25	179	54	-8.73	36.32	872.90	181	63
3PGa[67]	-11.52	177.31	660.95	189	61	-9.33	18.27	1078.3	192	75
3PGb[68]	-13.21	538.70	463.33	186	53	-8.76	9.08	1204.6	192	78
Ethanol[69]	-9.73	283.85	204.47	94	37	-7.89	31.53	420.84	99	51
Xylitol[70]	-12.70	278.52	802.46	238	64	-8.59	1.78	2002.9	247	97
Freon12[71]	-11.93	165.78	245.23	87	53	-4.64	1.4E-4	1438	91	82
PVaca[72]	-8.75	7.78	2132.8	309	84	-9.73	15.94	1941.3	310	85
PVacb[73]	-10.03	78.81	1408.5	302	68	-3.88	0.01	3806.2	295	82
Pvacc[74]	-11.07	90.59	1412.6	306	74	-7.92	0.97	2761	310	98
Pvacd[75]	-10.58	95.85	1329.1	296	69	-9.71	26.26	1718.1	300	79
8*OCB[76]	-10.34	120.19	852.43	217	61	-7.52	1.80	1747	221	85
E7[34]	-10.38	345.54	560.94	200	47	-5.45	0.15	2001	199	82
***C8c7*[43]**	-11.99	1791.9	146.18	149	28	-7.51	249.22	390.76	151	34
***NPGNPA*[32]**	-12.48	1363.8	200.75	152	34	-4.98	0.64	1335.9	161	65
5*CB[77]	-9.65	29.74	120.22	35	52	-10.15	162.09	733.04	205	56

Table 5.9: *Values of the crossover temperature from Mauro equation T_c and from VFT analysis T_{VFT}, the experimental glass transition temperature T_g, the ratio T_c/T_g and the transition factor f for the liquids under study. The liquids with a fragille-strong $(F-S)$ transition is bold.*

Materials	Tc [K]	Tg [K]	Tc/Tg	TVFT [K]	100*(Tc-TVFT)/TVFT	m1	m2	f =m1/m2
EPON[56]	302	252	1.198	293	3.07	76	142	**0.53**
PPGE[56]	268	259	1.035	277	-0.03	26	45	**0.58**
OTP[57]	283	241	1.174	296	-4.39	123	83	1.48
KDE[58]	365	314	1.162	371	-1.62	97	70	1.39
PC[59]	187	154	1.214	192	11.46	73	90	**0.81**
Salol[60]	245	217	1.129	251	-2.60	116	73	1.59
DEP[61]	223	183	1.219	228	-2.19	99	54	1.83
MTH[62	110	91	1.201	112	-1.78	65	82	**0.79**
PCB42[63]	249	220	1.132	252	-1.19	99	63	1.57
PCB54[63]	289	243	1.189	291	-0.69	112	61	1.84
PCB62[63]	306	269	1.138	309	-0.97	110	57	1.93
PS540k[64]	289	252	1.147	291	-0.69	116	77	1.51
Glycerol[65]	233	194	1.201	232	0.43	43	41	1.05
PG[65]	243	174	1.397	240	1.25	53	40	1.33
2PG[65]	226	192	1.177	224	0.89	48	57	**0.84**
DBP[66]	204	181	1.128	210	-2.86	54	63	**0.86**
3PGa[67]	221	192	1.151	219	0.92	61	75	**0.81**
3PGb[68]	220	192	1.146	217	1.39	53	78	**0.68**
Ethanol[69]	118	99	1.192	116	1.73	37	51	**0.73**
Xylitol[70]	280	247	1.134	278	0.72	64	97	**0.66**
Freon12[71]	95	89	1.067	93	2.15	53	82	**0.65**
PVaca[72]	327	310	1.055	324	0.93	84	85	**0.99**
PVacb[73]	310	295	1.051	309	0.32	68	82	**0.83**
Pvacc[74]	342	310	1.103	338	1.18	74	98	**0.76**
Pvacd[75]	384	300	1.280	375	2.43	69	79	**0.87**
8*OCB[76]	252	221	1.140	357	1.96	61	85	**0.72**
E7[34]	232	199	1.166	224	3.57	47	82	**0.57**
***C8c7*[43]**	174	151	1.152	167	4.19	28	34	**0.82**
***NPGNPA*[32]**	183	161	1.137	182	0.55	34	65	**0.52**
5*CB[77]	250	205	1.219	352	0.57	52	56	**0.93**

Bibliography

[1] L. P. Singh, S. S.N. Murthy, J. Phys. Chem. B **112**, 2606, (2008).

[2] F. Kremer, A. Schoenhals, *Broad Band Dielectric Spectroscopy*, Springer, Berlin, (2003).

[3] C. A. Angell, *Relaxations in Complex Systems*, edited by K.L. Ngai and G. B. Wright, NRL, Washington DC, (1985).

[4] R. Puertas, M. A. Rute, J. Salud, D. O. López, S. Diez, J.C. van Miltenburg, L.C. Pardo, J.Ll. Tamarit, M.Barrio, M.A. Pérez-Jubindo, M.R de la Fuente, Phys. Rev. B **69**, 224202, (2004).

[5] D. L. Leslie-Pelecky, N. O. Birge, Phys. Rev. Lett **72**, 1232, (1994).

[6] M. Shablakh, L. A. Dissado, R. M. Hill, J. Chem. Soc., Faraday Trans **79**, 383, (1983).

[7] R. Brand, P. Lunkeheimer, A. Loidl, Phys. Rev. B **56**, R5713, (1997).

[8] M. A. Rute; J. Salud; P. Negrier, D. O. López, J.Ll. Tamarit, R. Puertas, M. Barrio, D. Mondieig, J. Phys. Chem. B **107**, 5914, (2003).

[9] J. Salud, D. O. López, M. Barrio, J. Ll. Tamarit, J. Mater. Chem **9**, 909, (1999).

[10] J. Ll.Tamarit, M. A. Pérez-Jubindo, M. R. de la Fuente, J.Phys.: Condens. Matter **9**, 5469, (1997).

[11] P. Lunkenheimer, R. Brand, U. Schneider, A. Loidl, Philos. Mag. B **79**, 1945, (1999).

[12] R. Puertas, J. Salud, D.O. López, M. A. Rute, S. Diez, J. Ll. Tamarit, M. Barrio, M. A. Pérez-Jubindo, M. R. de la Fuente, L.C. Pardo, Chem. Phys. Lett **401**, 368, (2005).

[13] M. Tyagi, S. S. N. Murthy, J. Chem. Phys **114**, 3640, (2001).

[14] K. L. Ngai, S. Capaccioli, Phys. Rev. E **69**, 031501, (2004).

[15] F. Alvarez, A. Alegria, J. Colmenero, Phys. Rev. B **44**, 7306, (1991); Phys. Rev. B **47**, 125, (1993).

[16] J. P. Amoureux, M. Castelain, M. D. Benadda, M. Bee, J.L. Sauvajol, J. Phys. (Paris) **44**, 513 (1983).

[17] J. P. Amoureux, M. Sahour, C. Fernandez, P. Bodart, Phys, Stat. Sol **143**, 441 (1994).

[18] A. Alegría, E. Guerrica-Echevarría, L. Goitiandía, L. Lellería, J. Colmenero, Macromolecules **28**, 1516 (1995).

[19] R. Kohlrausch, Prog. Ann. Phys **91**, 179 (1854).

[20] G. Williams, D. C. Watts, Trans. Faraday Soc. **66**, 80 (1970).

[21] S. Capaccioli, K. L. Ngai, J. Phys. Chem. B **109**, 9727 (2005).

[22] J. Kirkwood, J. Chem. Phys **7**, 911, (1969); H. Frölich, H. Frohilich, *Theory of Dielectrics*, Oxford University Press, London, (1949).

[23] S. J. Suresh, V. M. Naik, J. Chem. Phys **116**, 4212 (2002).

[24] V. P. Pawar, S. C. Mehrotra, J. Mol. Liq **95**, 63, (2002).

[25] V. P. Pawar, A. R. Patilb, S. C. Mehrotra, J. Mol. Liq **121**, 88, (2005).

[26] R. J. Sengwa, S. Sankhla, J. Mol. Liq **130**, 119, (2007).

[27] G. Parthipan, T. Thenappan, J. Sol. Chem. **36**, 1231, (2007).

[28] L. C. Pardo, M. Barrio, J. Ll. Tamarit, D.O.López, J. Salud, P. Negrier, D. Mondieig. Phys.Chem.Chem.Phys **3**, 2644, (2001).

[29] L. Carpentier, R. Decressain, M. Descamps, J. Chem. Phys. **128**, 024702, (2008).

[30] F. Stickel, E. W. Fischer, R. Richert, J. Chem. Phys. **104,** 2043, (1996).

[31] A. Drozd-Rzoska and S. J. Rzoska, Phys. Rev. E. **73**, 041502, (2006).

[32] A. Drozd-Rzoska, S. J. Rzoska, S. Pawlus, J. Ll. Tamarit, Phys. Rev. B **73,** 224205,(2006).

[33] A. Drozd-Rzoska, S. J. Rzoska, S. Pawlus, J. Ll. Tamarit, Phys. Rev. B **74** , 064201, (2006).

[34] A. Drozd-Rzoska, S. J. Rzoska and C. M. Roland, J. Phys.: Condens. Matt **20**, 244103, (2008).

[35] R. H. Colby, Phys. Rev. E **61**, 1783, (2000).

[36] E. Leutheuser, Phys. Rev. A **29**, 2765, (1984).

[37] S. A. Kivelson, G. Tarjus, Nature Materials **7**, 831 (2008).

[38] W. Goetze, L. Sjoegren, Rep. Prog. Phys **55**, 241 (1992).

[39] Y. S. Elmatad, D. Chandler, J. P. Garrahan, J. Phys. Chem. B **113**, 5563 (2009).

[40] A. I. Nielsen, T. Christensen, B. Jakobsen, K. Niss, N. B. Olsen, R. Richert, J. C. Dyre, J. Chem. Phys **130**, 154508 (2009).

[41] N. B. Olsen, T. Christensen, J. C. Dyre, Phys. Rev. Lett **86**, 127, (2001).

[42] A. I. Nielsen, S. Pawlus, M. Paluch, J. C. Dyre, Phil. Mag **88**, 4101, (2008).

[43] J. C. Martinez-Garcia, J. Ll. Tamarit, L. C. Pardo, M. Barrio, S. J. Rzoska, and A. Drozd-Rzoska, J. Phys. Chem. B **14**, 6099, (2010).

[44] J. C. Martinez-Garcia, J. Ll. Tamarit, S. J. Rzoska, A. Drozd-Rzoska, L. C. Pardo, and M. Barrio, J. Non-Cryst. Solids **357**, 329, (2011).

[45] M. Romanini, J. C. Martinez-Garcia, J. Ll. Tamarit, S. J. Rzoska, M. Barrio, L. C. Pardo, and A. Drozd-Rzoska, J. Chem. Phys **131**, 184504 (2009).

[46] D. Gomez, A. Alegria, J. Non-Cryst. Solids **287**, 246, (2001).

[47] E. Donth, *The Glass Transition. Relaxation Dynamics in Liquids and Disordered Material*, Springer Series in Material Sci. II, Vol. 48 Springer Verlag, Berlin, (1998).

[48] C. F. J. Böttcher, O. C. Belle Van, P. Bordewijk, Rip, A.; *Theory of Electric Polarisation*; **Vol I (2nd edition)**, Elsevier: Amsterdam, (1973)

[49] R. Böhmer, K. L. Ngai, C. A. Angell, D. J. Plazek, J. Chem. Phys **99**, 4201 (1993).

[50] J. C. Martinez-Garcia, J. Ll. Tamarit, S. J. Rzoska, J. Chem. Phys **134**, 024512 (2011).

[51] P. Lunkenheimer, L. C. Pardo, M. Koehler, A. Loidl, Phys. Rev. E **77**, 031506, (2008).

[52] J. J. Moura Ramos, N. T. Correia, H. P. Diogo, C. Alvarez, T. A. Ezquerra, J. Non-Cryst. Solids **351**, 3600, (2005).

[53] A. Döß, M. Paluch, H. Sillescu, G. Hinze, Phys. Rev. Lett **88**, 095701, (2002).

[54] J. C. Mauro, Y. Yue, A. J. Ellison, P. K. Gupta, D. C. Allan, PNAS **106**, 19780, (2009).

[55] J. C. Martinez-Garcia, J. Ll. Tamarit, S. J. Rzoska. J. Phys. Chem **134**, 024512, (2011).

[56] S. Corezzi, M. Beiner,H. Huth, K. Schroter, S. Capaccioli, R. Casalini, D. Fioretto,E. Donth, J. Chem. Phys **117**, 2435 (2002).

[57] C. M. Roland, R .Casalini, J. Phys.: Condens. Matter **19**, 205118,(2007).

[58] F. Stickel, F. Kremer, E.W. Fischer, Physica A **201**, 318, (1993).

[59] F. Stickel, E. W. Fischer, R. Richert, J. Chem. Phys **104**, 5, (1996)

[60] F. Stickel, E. W. Fischer, R. Richert, J. Chem. Phys **102**, (15), (1995).

[61] M. Paluch, C. M. Roland, J. Non-Cryst. Solids **316**, 413, (2003).

[62] R. Richert, C. A. Angell, J. Chem. Phys **108**, 21 (1998).

[63] C. M .Roland, S. Hensel-Bielowka, M. Paluch, R Casalini, Rep. Prog. Phys **68**, 1405, (2005)

[64] S. Pawlus , K. Kunal, L. Hong, A.P. Sokolov, Polymer **4**, 2918, (2008).

[65] A. Schönhals, F. Kremer, J. Non-Cryst. Solids **172**, 336, (1994).

[66] A. Schönhals, Europhys. Lett **56,** 815, (2001).

[67] K. Grzybowska, A. Grzybowski, S. Pawlus, S. Hensel-Bielowka, M. Paluch, J. Chem. Phys **22**, 204506, (2005).

[68] K. Grzybowska, A. Grzybowski, J. Zioło, M. Paluch, S. Capaccioli, J.Chem.Phys **125**, 044904 (2006).

[69] R. Brand, P. Lunkenheimer, U. Schneider, A. Loidl, Phys. Rev. B **62**, 8878, (2000).

[70] P. Lunkenheimer, R. Wehn, U. Schneider, A. Loidl, Phys. Rev. Lett. **95**, 055702, (2005). R. Wehn, P. Lunkenheimer, A. Loidl, J. Non-Cryst. Solids **353**, 3862, (2007).

[71] L. C. Pardo, P. Lunkenheimer, A. Loidl, J. Chem. Phys. **124**, 124911, (2006).

[72] C. M. Roland, R. Casalini, Macromolecules **36**, 1361, (2003).

[73] R. Richert, Physica A **287**, 26, (2000).

[74] W. Heinrich, B. Stoll, Colloid Polym. Sci **263**, 873, (1985).

[75] F. Stickel, Doctoral Thesis, 1995, Johannes Gutenberg-Universtat Mainz, Germany (Shaker, Achen, 1995)

[76] A. Drozd-Rzoska, S. J. Rzoska, M. Paluch, J. Chem. Phys **129**, 184509, (2008).

[77] A. Drozd-Rzoska, J. Chem. Phys **130**, 234910, (2009).

[78] G. G. Naumis, J Non-Cryst Solids **352**, 4865, (2006).

[79] P. K. Gupta, J. C. Mauro, J .Chem. Phys. **130**, 094503, (2009).

[80] C. Zhang, L. Hu, Y. Yue, John. C. Mauro, J .Chem. Phys **133**, 014508, (2010).

[81] K. Ito, C. T. Moynihan, C. A. Angell, Nature (London) **398**, 492, (1999).

[82] C. A. Angell, Chem. Rev. (Washington, D.C.) **102**, 2627, (2002).

[83] L. M. Martinez, C. A. Angell, Nature (London) **410**, 663, (2001).

[84] C. A. Angell, Science **267**, 1924, (1995).

[85] C. A. Angell, J. Non-Cryst. Solids **354**, 4703, (2008).

Chapter 6

General Conclusions

The work presented in this thesis potentially extends the knowledge of dynamics of orientationally disordered phases and orientationally glasses, a research topic which has gained interest during the last decades. The aim of this work has been to account for the orientational dynamics of simple globular-shaped molecules with and without intramolecular degrees of freedom as well as to investigate the effect of intermolecular interactions on the dynamics by means of the study of several mixed crystals. Through this study, especial attention has been devoted to the phenomenological equations accounting to the temperature dependence of the mean relaxation time describing the orientational dynamics. Within this topic, a new approach based on the derivative sensitive analysis has been developed. The main conclusions are sketched in the following lines

Dynamics in binary systems

Binary system cyclooctanol (C8-ol) and cycloheptanol (C7-ol) The dynamics of the pure compounds and mixed crystals formed between C7-ol and C8-ol have been studied by means of broadband dielectric spectroscopy at temperatures near and above the orientational glass transition temperature. We have performed a detailed analysis of the dielectric loss spectra showing clear evidence of the relaxation processes for the orientational glass-former pure compounds. The results focus on the issue of the appearance of the secondary relaxations for the OD $(C7-ol)_{1-x}(C8-ol)_x$ mixed crystals and try to make clear if they are concomitant with those found for pure components or, on the contrary, a change of the effects of many-molecule dynamics and intermolecular coupling or a change in the hydrogen bonding scheme can induce their disappearance, as claimed for the β-relaxation in a preceding work [1].

- The α-relaxation times as a function of the reciprocal of temperature for the whole set of studied mixed crystals together with those of pure compounds for the simple cubic orientationally disordered (OD) phase I are obtained. They clearly evidence the continuous change of the relaxation time as a function of the mole fraction, supporting the conjecture that isomorphism between phases I of C7-ol and C8-ol involves also the dynamic behaviour.

- For $(C7-ol)_{1-x}(C8-ol)_x$OD mixed crystals the dielectric loss spectra were fitted by assuming the existence of the ubiquitous α-relaxation process (at $T > T_g$) and one or two secondary processes. It was concluded that the introduction of an additional third relaxation process is completely fictitious and thus that only α- and γ-relaxation processes are present for $x < 0.74$. On the contrary, for mixed crystals with $x \geq 0.74$ the presence of the three relaxation processes clearly improves the description of the experimental data [1].

- In spite of the evidences concerning the intramolecular character of the β and γ secondary relaxations for the pure components as well as for the mixed crystals we obtained thermally activated processes, which are described by a continuous change of the activation energy between the values of pure compounds for the γ relaxation and by almost constant activation energy for the β relaxation. This result confirms the intramolecular character of the β-relaxation associated to the transitions between the two possible conformations of the –OH side group of C8-ol and the continuous variation (relaxation time and activation energy) for the γ process evidences its intrinsic relation to the hydrogen-bond scheme.

- The relaxation times for β and γ processes were also determined without superimposing a phenomenological model by means of the application of a derivative process of the real part of the complex permittivity based on the Kramers-Kronig relations at temperatures lower that the glass transition temperature T_g. It was determined by the steps or inflection points in the real part of the dielectric permittivity $\varepsilon^{'}$ function, inherently associated with the peak of the imaginary dielectric permittivity $\varepsilon^{''}$, which translates to a maximum in the first derivative of $\varepsilon^{'}$with respect to the frequency. The results confirm, at $(T < T_g)$, the Arrhenius behaviour for β and γ relaxations. The activation energies obtained from the used methodology compare well with those obtained at $(T > T_g)$ from previous standard procedures. The procedure shows up a new method to make evident the existence of such secondary relaxations as well as to avoid phenomenological equations for determining the relaxation time and for testing possible secondary relaxation process in glass forming systems [2].

Binary system CN-adamantane (CNadm) and Chloro-adamantane (Cladm)

The α-relaxation dynamics of CNadm and its mixtures with Cladm have been studied by means of broadband dielectric spectroscopy. The existence of OD face centered cubic mixed crystals $(Cladm)_{1-x}(CNadm)_x$ for $0.5 \leq x \leq 1$ has been put in evidence by thermodynamics and structural analyses [3].

- It was shown that the non-exponential character evidenced by the broadening of the α-relaxation peak and characterized by the stretched parameter with the diminution of the mole fraction is caused by the heterogeneities produced by the concentration fluctuations which are the consequence of a statistic (chemical) disorder and not induced by dynamic correlations. This result shows that local heterogeneities generated by the compositional disorder

control the relaxation process, a result which is similar to that previously found for structural glasses [3,4].

- It was shown a new way for calculating the Kirkwood factor g for mixtures. The effective dipole moment of the molecular entity have been calculated following the procedure of the molecular volume as a linear combination of the dipole moment for the pure compounds with the mole fraction [4]. The results show small shift, with a discrepancy less than 10% in comparison with other methods which weight the square dipoles by volume fractions or by mass fractions.

- The variation of the Kirkwood factor evidences the existence of a strong antiferroelectric order of molecular entities, which increases with the mole fraction of CNadm and decreases with temperature. It was shown that in addition, for all the studied compositions higher than the equimolar mixture, also including CNadm pure compound, a stair-like diminution is observed, a consequence of the reinforcement of an antiferroelectric ordering. This change comes from an abrupt diminution of the dielectric strength together with a continuous variation of density as a function of temperature [4].

- It was used a new numerical procedure for transforming the experimental dielectric spectra, obtained in the frequency domain to the time domain by means of the use of the connection between dielectric permittivity and relaxation function via the Laplace-Fourier transformation. The procedure has been supported by means of the Mathemathic platform (Mathematic 8.0). The stretched parameter was directly fitted at each temperature and each mole fraction. The relationship between such a fit parameter and those obtained from the fits of the HN equation evidenced that the proposed relation for structural glasses from Alegria et. al perfectly works for the whole temperature and composition studied range [4].

Derivate analysis

Linearized models It was applied the derivative based, distortion-sensitive analysis to the relaxation times datas $\tau(T)$ for Liquid Crystals, isooctylcyanobiphenyl (8*OCB), pentylcyanobiphenyl (5OCB) and ODICs materials, a set of systems formed by pure compounds displaying a well-known hydrogen bonding scheme as cyclooctanol (C8-ol) and cycloheptanol (C7-ol), as well as systems lacking of this kind of particular intermolecular interactions, as cyanoadamantane (CNadam) and cyanocyclohexane (CNc6), several mixtures between C7-ol and C8-ol and between CNadam and Cladam, neopentylalcohol (NPA) and neopentylglycol (NPG) mixture$(NPA_{0.7}NPG_{0.3})$, one olygomeric liquid epoxy resin (EPON828), and Propylene Carbonate (PC).

- The application of the derivative analysis to C8-ol, C7-ol, CNadam, CNc6, several mixtures between C7-ol and C8-ol and between CNadam and ClAdam, $NPA_{0.7}NPG_{0.3}$, 8*OCB, and

5*CB has been performed for testing the validity of the dynamical scaling model (DSM). We have concluded that the DSM can perfectly account the scaling exponent of the relaxation time as a function of temperature for all the OD crystals studied by using the linearized derivative analysis. It was concluded that the exponent close to 9 seems to be a general property for phases with only one kind of disorder, translational for liquid crystals and orientational for OD phases, reinforcing the existence of a hidden phase transition at ($T_c < T_g$) and claiming the existence of a group of ultraslowing materials, fluid and solid, where a clear evidence for the dynamic divergence exists [5-7].

- It was found an empirical correlations between the critical exponent of the DSM model with the universal pattern for the high frequency wing $f > f^{\alpha}_{peak}$ of the loss curve for primary relaxation process for LCs and ODICs. It was concluded that the minimal slope at the glass transition temperature as a function of the critical exponent corresponding to the DSM as well as the fragility and the slope of the dielectric loss spectra of the α-relaxation at $f > f^{\alpha}_{peak}$ should be correlated [8].

- The linearized derivative analysis was also applied to EPON828 and Propylene Carbonate data. We concluded that two VFT equations are needed to describe $\tau(T)$ in the broader range of temperatures. The same was found for the "Avramov" equation i.e., the existence of a crossover, an artifact not reported so far. In agreement with earlier reports we have found a superior validity of the critical-like description in the ultraviscous/ultraslowing domain for the liquid crystalline and the orientationally disordered crystals glass formers. The linearized analysis have revealed a very limited validity of the equation recently proposed by Elmatad hardly visible at the $\tau(T)$ plot [9].

Non-Linearized models It was shown that the form of the equation introduced by Mauro et. al. does not allow a similar straightforward linearization procedure. Unlike the previous models, the involved parameters (K, C) are not correlated with the slope and the intercept of a linear function, thus both variables being necessarily and simultaneously involved in the data analysis. In order to resolve this problem, we have introduced the concept of the enthalpy space as the three-dimensional chi-square space, obtained after a derivative transformation of the relaxation time- temperature evolution, which is called $(H_a - 3D)$.

- For estimating the model parameters in the Mauro equation, it was introduced a function of merit given by the sum of weighted squared residuals [9].

- It was performed an iterative optimization method, which have been supported by means of the Mathemathic platform (Mathematic 8.0). For the case of models involving an exponential function we concluded that the use of the Newton method for minimizing glass forming model functions can be a realible alternative solution. It was also concluded that the use of a

relative weighted function of merit minimizes the sources of errors being more advantageous to implement minimization processes [10].

- For all liquids under study the plot $\ln\left[H_a/\left(1+\frac{C}{T}\right)\right]$ vs $1/T$ as well as the plot of the configurational entropy S_c rescaled by B reveal the evidence of the existence of dynamical crossover in the Mauro equation. It was shown that with this plot two temperature domains can be detected by a slope change at temperature T_c which signs a dynamic crossover. We have found one group of liquids where the slope of the above graph increases on cooling toward T_c as well as another group of liquids where the slope of the graph decreases. A new kind of crossover which seems to be impossible to be detected by the Stickel transformation is shown by a change of slope in one simple plot of $\ln[H_a]$ vs $1/T$ [11].

- For all the glass forming liquids under study the results have shown that there is not a big difference between the crossover temperature values obtained form the VFT and from the Mauro equations. We concluded that, excluding the cases of the 5*CB and 8*OCB, the plots of $T_{VFT}(T_g)$ and $T_c(T_g)$ surprisingly follows a good linear correlation. It can give us a practice and easy way for estimating the crossovers, when the experimental glass transition temperature of the liquid under study is previously known [11].

- For characterizing the glass behaviour around the crossovers temperature T_c, we have proposed a new fragility transition factor f. It was concluded that for all studied liquids the relative temperature crossover difference between VFT and Mauro equation is correlated with the fragility transition factor f . For the cases of PPGE, MTHFL, DBP, we found four excepctions [11]. Some glass forming systems (PPGE, MTHFL, DBP) seem to be apart from such a correlation and a more detailed analysis should be performed [11].

Corrective functions of coupling model (CM) equation It was introduced the corrective functions of the CM equation which have not been are reported so far. We have shown that the corrective CM equation can be written as the product of two terms, the original primitive relaxation time τ_0, introduced by Ngai, and a new term which is called as the corrective relaxation time function $C(n)$. It allows the introduction of the normalized corrective activation energy function $\Delta E(n)$.

- It was concluded that for all experimentally reported coupling domains $0 \leq n \leq 1$, independently of the chosen relaxation time from the experiment (τ_{HN},τ_{max} or τ_{KWW}), the corrective functions $C(n)$ and $\triangle E(n)$ will take values around the unity and zero respectively, and the CM equation will remain unchanged to testify the JG processes [12].

Bibliography

[1] J. C. Martinez-Garcia, J. Ll. Tamarit, L. C. Pardo, M. Barrio, S. J. Rzoska, A. Drozd-Rzoska, J. Phys. Chem. B **14**, 6099, (2010).

[2] J. C. Martínez-García, J.Ll. Tamarit, L. C. Pardo, M. Barrio, A. Drozd-Rzoska, S. J. Rzoska, Phys. Status Solid. A, in press (2011).

[3] J. C. Martinez-Garcia, S. Capaccioli, S. Diez, J. Ll. Tamarit, M. Barrio, N. Veglio, L. C. Pardo, J. Non-Cryst. Solids **356**, 621, (2010).

[4] J. C. Martinez-Garcia, J. Ll. Tamarit, S. Capaccioli, M. Barrio, N. Veglio, L. C. Pardo, J. Chem. Phys **132**, 164516, (2010).

[5] J. C. Martinez-Garcia, J. Ll. Tamarit, S. J. Rzoska, A. Drozd-Rzoska, L. C. Pardo, M. Barrio, J. Non-Cryst. Solids **357**, 329, (2011).

[6] M. Romanini, J. C. Martinez-Garcia, J. Ll. Tamarit, S. J. Rzoska, M. Barrio, L. C. Pardo, A. Drozd-Rzoska, J. Chem. Phys **131**, 184504, (2009).

[7] A. Drozd-Rzoska, S. J. Rzoska, S. Pawlus, J. C. Martínez-García, J.Ll. Tamarit, Phys. Rev. E **82**, 031501, (2010).

[8] J. C. Martinez Garcia, J. Ll. Tamarit, S. J. Rzoska, J. Chem.Phys **134**, 144505, (2011).

[9] J. C. Martinez-Garcia, J. Ll. Tamarit, S. J. Rzoska, J. Chem. Phys **134**, 024512, (2011).

[10] J. C. Martinez-Garcia. et. at, *(in preparation)*.

[11] J. C. Martinez-Garcia. et. al, *(in preparation)*.

[12] J. C. Martinez-Garcia. et. al, *(in preparation)*.